

Coherent Imaging of Cellular Dynamics

THÈSE N° 8202 (2017)

PRÉSENTÉE LE 15 DÉCEMBRE 2017
À LA FACULTÉ DES SCIENCES ET TECHNIQUES DE L'INGÉNIEUR
LABORATOIRE D'OPTIQUE BIOMÉDICALE
PROGRAMME DOCTORAL EN PHOTONIQUE

ÉCOLE POLYTECHNIQUE FÉDÉRALE DE LAUSANNE

POUR L'OBTENTION DU GRADE DE DOCTEUR ÈS SCIENCES

PAR

Miguel SISON

acceptée sur proposition du jury:

Prof. H. P. Herzig, président du jury
Prof. T. Lasser, directeur de thèse
Prof. T. Weil, rapporteuse
Dr M. Villiger, rapporteur
Prof. D. Van de Ville, rapporteur



ÉCOLE POLYTECHNIQUE
FÉDÉRALE DE LAUSANNE

Suisse
2017

Abstract

Mitochondrial dynamics refers to the processes of fusion, fission, and transport that aid mitochondria in accomplishing their many roles; including ATP production, oxygen sensing, and homeostasis. Due to their involvement in numerous essential cellular activities, dysfunctional mitochondria have been implicated in a wide range of human diseases.

Confocal microscopy using fluorophores for molecular specificity remains the gold standard of intracellular imaging. However, fluorescent labels can be toxic to the cell upon prolonged exposure and still suffer from photobleaching. This compromises the application of confocal fluorescence microscopy for true long lasting time-lapse imaging of living samples.

Optical coherence microscopy (OCM) exploits the intrinsic variation in the scattering properties of the sample to achieve fast, label-free, and highly sensitive three-dimensional imaging. Unfortunately, being label-free means OCM lacks specificity and coherence based imaging techniques have no counterpart to fluorescent markers. The invention of the photothermal optical lock-in OCM (poli-OCM) brought about the possibility of specific OCM imaging using gold nanoparticles (AuNP) as photothermal bio-markers. The use of AuNPs as specific contrast agents has substantial advantages stemming from their well-established biocompatibility and photostability.

Microscopic techniques that offer fast three-dimensional imaging over extended time durations may serve to reveal previously inaccessible knowledge on mitochondria. In this work we quantify mitochondrial dynamics based on specific poli-OCM and surface functionalization of AuNPs.

In realizing mitochondria specific poli-OCM imaging, it is necessary to functionalize AuNP with mitochondria targeting capabilities. We presented copolymer surface coatings that provide the AuNPs with improved stability, solubility, and cellular uptake on top of mitochondria labeling. We further optimized the utilization of these AuNP labels for poli-OCM imaging. We also demonstrated poli-OCM imaging with differently structured gold nanolabels, which could lead to the realization of multimodal imaging using a single bio-marker.

The two quantification techniques we developed are based on (1) temporal autocorrelation analysis combined with a classical diffusion model and (2) single particle tracking. Autocorrelation analysis is the foundation of fluorescence correlation spectroscopy (FCS); a technique extensively used for analyzing dynamic phenomena in chemistry and biophysics. We extended

this analysis to three-dimensional poli-OCM imaging allowing us to map quantified mitochondrial diffusion parameters in three dimensions within the cell. We also investigated how the size of the mitochondria with respect to the point spread function (PSF) of the poli-OCM impacts the result of our autocorrelation analysis. Single particle tracking complements our temporal autocorrelation analysis since recent advances in localization and tracking algorithms have demonstrated precision better than the size of the PSF.

Finally, we demonstrated the possibility of using mitochondria specific poli-OCM imaging with the quantification techniques we developed for studying the Cockayne syndrome (CS). CS is a very rare and fatal genetic disease that has been associated with mitochondrial dysfunction. To our knowledge, no study has been conducted focusing on quantifying the effect of CS on mitochondrial dynamics.

Key words: Optical coherence microscopy (OCM); photothermal optical lock-in OCM (poli-OCM); mitochondrial dynamics; gold nanoparticle functionalization

Résumé

La dynamique mitochondriale fait référence aux processus de fusion, de fission et de transport permettant aux mitochondries d'accomplir leurs différentes fonctions, notamment la production d'ATP, la détection d'oxygène, et l'homéostasie. Dû au rôle des mitochondries dans de nombreuses activités cellulaires essentielles, leur dysfonctionnement est impliqué dans une large variété de maladies humaines.

La microscopie confocale, qui apporte de la spécificité moléculaire grâce à l'utilisation de fluorophores, reste la méthode de référence pour l'imagerie intracellulaire. Cependant, les marqueurs fluorescents peuvent devenir toxiques pour la cellule lors d'une exposition prolongée et sont aussi sujets au photoblanchiment. Ces phénomènes compromettent l'utilisation de la microscopie de fluorescence pour imager des échantillons vivants sur de longues périodes.

La microscopie par cohérence optique (OCM) exploite les propriétés intrinsèques de l'échantillon en termes de diffusion de la lumière pour accomplir une imagerie tridimensionnelle rapide, sans marqueurs et avec une grande sensibilité. Cependant, la absence de marqueurs entraîne un manque de spécificité de l'OCM. Par ailleurs, les techniques basées sur la cohérence n'ont aucun équivalent aux marqueurs fluorescents. L'invention de l'OCM photothermique avec une détection synchrone optique (ou poli-OCM pour photothermal optical lock-in OCM) a rendu possible l'imagerie OCM spécifique en utilisant des nanoparticules d'or comme biomarqueurs photothermiques. L'usage de nanoparticules d'or en tant qu'agents de contraste spécifique présente des avantages considérables grâce à leur biocompatibilité et leur photostabilité bien établies.

Les techniques de microscopie permettant l'imagerie rapide tridimensionnelle sur des durées prolongées ont le potentiel de révéler des connaissances précédemment inaccessibles sur les mitochondries. Dans cette thèse, nous quantifions la dynamique mitochondriale en se basant sur l'imagerie spécifique en poli-OCM et la fonctionnalisation de surface des nanoparticules d'or.

Pour accomplir l'imagerie spécifique des mitochondries en poli-OCM, il est nécessaire de fonctionnaliser les nanoparticules d'or afin de cibler spécifiquement les mitochondries. Nous présentons des traitements de surface pour revêtir de copolymères les nanoparticules d'or, améliorant ainsi leur stabilité, leur solubilité et leur assimilation par les cellules en plus du marquage mitochondrial. De plus, nous optimisons l'utilisation de ces nanoparticules

d'or pour l'imagerie poli-OCM. Nous démontrons en outre l'imagerie en poli-OCM avec des nano-marqueurs d'or de structures différentes, permettant la réalisation d'une imagerie multimodale n'utilisant qu'un seul biomarqueur.

Les deux techniques de quantification que nous avons développées sont basées sur (1) l'analyse de l'autocorrélation temporelle combinée à un modèle de diffusion classique, et (2) le suivi de particules uniques (ou SPT pour single particle tracking). L'analyse de l'autocorrélation est à la base de la spectroscopie de corrélation de fluorescence (FCS), une technique largement utilisée pour l'analyse de phénomènes dynamiques en chimie et biophysique. Nous étendons cette analyse à l'imagerie tridimensionnelle en poli-OCM, nous permettant ainsi de caractériser de façon quantitative les paramètres de diffusion mitochondriale en trois dimensions à l'intérieur de la cellule. Nous investiguons aussi la manière dont la taille des mitochondries impacte le résultat de notre analyse d'autocorrélation par rapport à la fonction d'étalement du point (ou PSF pour point spread function). Le SPT complète notre analyse de l'autocorrélation temporelle, des avancées récentes sur les algorithmes de suivi et de localisation ayant démontré une précision meilleure que la taille de la PSF.

Finalement, nous démontrons la possibilité d'utiliser l'imagerie spécifique des mitochondries en poli-OCM avec les techniques de quantification développées pour l'étude du syndrome de Cockayne (SC). Le SC est une maladie héréditaire très rare et fatale qui a été associée à un dysfonctionnement mitochondrial. A notre connaissance, aucune étude se focalisant sur la quantification de l'effet du SC sur la dynamique mitochondriale n'avait été conduite auparavant.

Mots clefs : microscopie par cohérence optique (OCM); OCM photothermique avec une détection synchrone optique (poli-OCM); dynamique mitochondriale; fonctionnalisation des nanoparticules d'or

Contents

Abstract (English/Français)	i
Introduction	1
1 Mitochondrial dynamics	5
1.1 Mitochondrial dysfunction and diseases	6
1.2 Remarks	9
2 Coherence and photothermal optical coherence microscopy	11
2.1 Interference	11
2.2 Frequency domain optical coherence tomography (FDOCT)	12
2.3 Optical coherence microscopy (OCM)	14
2.4 Photothermal optical lock-in OCM	14
3 Gold nanoparticle functionalization and mitochondria imaging	17
3.1 Multifunctional copolymer coated AuNPs for poli-OCM imaging	18
3.2 Mitochondria imaging with various Au-nanostructures	23
3.3 Summary	24
4 Quantification of mitochondrial dynamics	27
4.1 3D time-lapse imaging and quantification of mitochondrial dynamics	28
4.1.1 Introduction	29
4.1.2 Results and Discussion	30
4.1.3 Conclusion	36
4.1.4 Methods	36
4.1.5 Supporting Information	40
4.2 poli-OCM autocorrelation analysis for finite sized particles	48
4.3 Quantifying mitochondrial dynamics via 3D single particle tracking	54
4.3.1 Introduction	55
4.3.2 Methodology	55
4.3.3 Results and Discussion	58
4.3.4 Conclusion	60

Contents

4.4 Summary	62
5 Outlook: Mitochondrial dynamics in the Cockayne Syndrome	63
5.1 CS cell viability with AuNP-mitochondria labeling	64
5.2 Quantifying CS mitochondrial dynamics	64
5.3 Summary	69
6 Conclusion	71
Acknowledgements	75
Bibliography	79
Curriculum Vitae	99

Introduction

Mitochondria are dynamic organelles found in most eukaryotic cells existing in a highly interconnected network [1]. Their primary function is to provide the cell with ATP via oxidative phosphorylation [2] but they have been known to factor in other cellular activities. These include oxygen sensing [3, 4], regulation of intracellular Ca^{2+} [5–7], and apoptosis [8–10] among others. In accomplishing these tasks, the mitochondrial network undergoes continuous reorganization via the processes of fusion, fission, and transport; collectively referred to as mitochondrial dynamics [11, 12]. Considering mitochondrial involvement in a number of mechanisms ensuring the health and survival of the cell, it is not surprising that mitochondrial dysfunction has been implicated with numerous human diseases [1, 13, 14]. While multiple studies have linked mitochondrial dynamics to the pathogenesis of different diseases, most have focused on genetic and biochemical aspects [15–17]. Very few, if any, have approached this phenomena via imaging and quantification of mitochondrial motion from a physics and kinetics perspective. This is despite the recent advances in microscopy [18, 19], from which our understanding of intracellular structure and mitochondrial morphology has benefited [20–24].

Confocal fluorescence microscopy is still the most widely used imaging technique in cell biology, providing three-dimensional structural information with a diffraction limited resolution. Furthermore, it achieves molecular specificity with the use of fluorescent bio-markers. The availability of a broad range of fluorophores, designed for various intracellular structures, proteins, and organelles contributes to the versatility of confocal microscopy. Unfortunately, most fluorescent labels are either susceptible to photobleaching or inherently toxic [25, 26]. These limitations hinder the use of confocal fluorescence microscopy in applications requiring long term imaging of living samples.

Optical coherence microscopy (OCM) is a three-dimensional imaging technique that uses a broadband light source with a short coherence length to achieve depth-sectioning [27]. It is fast, highly sensitive, and label-free; obtaining its contrast from the intrinsic variation of the sample's scattering properties. OCM has demonstrated its value in biomedical research through its application in studies focusing on the progression of diabetes [28–32] and Alzheimer's disease [33]. Similarly, cellular imaging with the OCM has already been achieved [34, 35]

Contents

but the lack of specificity limits its further involvement in intracellular imaging. Unfortunately, coherence based techniques do not have a counterpart to the fluorescent biomarkers used in confocal microscopy. It was the invention of the photothermal optical lock-in OCM (poli-OCM), which realized the possibility of specific OCM imaging using gold nanoparticles (AuNPs) as photothermal contrast agents.

In this thesis we develop techniques for quantifying mitochondrial dynamics by exploiting the speed and specificity of three-dimensional poli-OCM imaging and using functionalized AuNPs as mitochondria specific labels.

An important component of our approach is the surface functionalization of AuNPs. We present copolymer coatings based on human and bovine serum albumin that impart mitochondria targeting and improve the solubility, biocompatibility, and cellular uptake of the AuNPs. Photothermal imaging using AuNP bio-markers offers substantial advantages due to the well-established biocompatibility and photostability of gold. We optimize the utilization of these AuNP labels for poli-OCM imaging by adjusting the labeling concentration and characterizing the poli-OCM signal. Furthermore, we demonstrate mitochondria specific poli-OCM imaging using differently structured nanoparticle labels.

We develop two techniques for quantifying mitochondrial dynamics. The first one is based on temporal autocorrelation analysis merged with a classical diffusion model. This technique extends the analytical foundation of fluorescence correlation spectroscopy (FCS) [36] to three-dimensional poli-OCM imaging. We demonstrate the ability of our technique to extract spatially resolved mitochondrial diffusion parameters. We also investigate the accuracy of our measurements through numerical simulations. Specifically, we determine the impact of maintaining the assumption of point-like diffusers despite the non-negligible size of the mitochondria compared to the focal volume of the poli-OCM. We consider the effect of mitochondrial size as a modification to the molecular detection function (MDF) of the poli-OCM. Furthermore, the Bessel-like illumination beam of the poli-OCM augments the extracted diffusion parameters and needs to be incorporated in the modified MDF. The second technique we develop is based on single particle tracking (SPT). We elaborate on how the higher localization precision of SPT results in a more accurate measurement of mitochondrial diffusion constant. Moreover, we demonstrate the possibility of using SPT to identify and quantitatively differentiate the transition between diffusive and directional mitochondria motion.

Finally, we apply the techniques we developed to study the Cockayne syndrome (CS); a very rare and fatal genetic disease that cause neurdegeneration and developmental deficiency [37]. CS shares a lot of its symptoms with neurodegenerative diseases and mitochondrial dysfunction has been strongly implicated with its pathogenesis [37–39]. To our knowledge, no study has attempted to quantify the effects of CS on mitochondrial dynamics.

The rest of this thesis is organized as follows:

- **Chapter 1** focuses on mitochondrial dynamics and how it is associated with human diseases. Here we give a brief overview of the characteristics and functions of mitochondria that contribute to the overall health and survival of a cell. We cite some mitochondrial related diseases and discuss how abnormal mitochondrial dynamics link to their pathogenesis.
- **Chapter 2** reviews the theoretical concepts that are most relevant for poli-OCM imaging.
- **Chapter 3** discusses the use of AuNPs as bio-markers for poli-OCM imaging. In this chapter we elaborate on the physical properties of AuNPs that make them ideal labels for long term live cell imaging applications. We also present a method for surface functionalization of AuNPs that imparts mitochondria targeting. We also explain the procedure and analysis in optimizing AuNP labeling for poli-OCM imaging.
- **Chapter 4** We present the techniques we developed to quantify mitochondrial dynamics via three-dimensional time-lapse imaging with poli-OCM. We include our publication and a submitted manuscript detailing these techniques, which are based on temporal autocorrelation analysis with a classical diffusion model and single particle tracking. In this chapter we also investigate the accuracy of our autocorrelation analysis using numerical simulations.
- In the last chapter, **Chapter 5**, we present the results of our pilot study aimed at demonstrating the possibility of using the techniques we developed for imaging and quantifying mitochondrial dynamics to study the Cockayne syndrome.

1 Mitochondrial dynamics

Mitochondria are organelles commonly found in eukaryotic cells. They are famously known as the “powerhouse of the cell” providing energy by producing cellular ATP. In order to sustain the cell’s energy needs, mitochondria exist in a highly interconnected network. This mitochondrial network undergoes continuous transformation through the process of fusion and fission depending on current cell activity. Fission allows mitochondria to divide and increase their number. These individual ball-shaped mitochondria are more mobile and are capable of migrating across different locations in the cell. The redistribution and transport of mitochondria is necessary to provide for the regions of the cell with the most energy demand. An example of this mitochondrial migration is seen in neurons where mitochondria from the soma are transported along the extent of the axon in support of neurite growth [40]. On the other hand, fusion enables mitochondria to form longer strands and/or attach to the mitochondrial network. ATP production through oxidative phosphorylation (OXPHOS) has been shown to promote mitochondria fusion [41]. In fact, according to Youle et al. fusion helps in maximizing OXPHOS by improving complementation among damaged mitochondria [42]. In this thesis we will refer to mitochondria fusion, fission, and migration with the general term mitochondrial dynamics.

On top of ATP production, mitochondria are also involved in a number of regulatory cell functions. Mitochondria control intracellular Ca^{2+} , which is crucial for homeostasis [6]. Intracellular Ca^{2+} is used for signaling [43] where Ca^{2+} may trigger various functions including cell apoptosis [44], differentiation [45, 46], and enhanced oxidative metabolism [47]. This regulation of Ca^{2+} by the mitochondria is linked to the fusion mediator mitofusin-2 (Mfn2) [6].

Mitochondria also function as cellular oxygen sensors. Oxygen is a necessary component of ATP production via OXPHOS. In oxygen limited environments, eukaryotic cells need to activate an adaptive response to ensure survivability [48]. As a reaction to hypoxia, mitochondria release reactive oxygen species (ROS) via the electron transport chain [49, 50]. The increased

Chapter 1. Mitochondrial dynamics

level of ROS, in turn, activates the hypoxia-inducible factors (HIFs) [49]. Mitochondria fission is an important upstream facilitator of this adaptive response mechanism and it has even been shown that inhibited fission prevents hypoxia-induced metabolic shift, which include preferring glycolysis over OXPHOS [51].

Ensuring mitochondrial integrity is another cell function that is associated with mitochondrial dynamics. Mitophagy is a “quality control” mechanism pertaining to the degradation of compromised or dysfunctional mitochondria. Damaged mitochondria is first isolated via fission before being disposed of by lysosomes [52]. In contrast, mitochondrial biogenesis is mediated by peroxisome proliferator-activated receptor- γ coactivator-1 α (PGC-1 α), which also regulates the expression of the fusion mediator Mfn2 [53, 54].

It is evident that mitochondrial dynamics are essential for mitochondria to accomplish their various duties. It comes with little surprise that dysfunctional mitochondrial dynamics have been implicated with aging and several diseases [13, 17].

1.1 Mitochondrial dysfunction and diseases

In addition to producing ATP, mitochondria play multiple roles in maintaining normal cellular function. Because of these roles, a number of human conditions have been associated with abnormal mitochondrial behaviour and dynamics. These conditions include but are not limited to normal aging, metabolic disease, cancer, and neurodegenerative diseases [13]. In this section we give examples of a few diseases and how mitochondrial dynamics impact their pathogenesis.

Cancer According to Hanahan and Weinberg the hallmarks of cancer are (1) sustained cell proliferation and (2) robustness against growth suppressor, (3) resistance to programmed cell death or apoptosis, (4) high invasiveness potential, (5) promotion of angiogenesis, and (6) enabling replicative immortality [55]. Among these qualities, resistance to apoptosis is the one most closely related to mitochondrial dynamics. Inhibiting the mitochondrial apoptotic pathway is the most common form of cell death deregulation shared by a variety of cancer phenotypes [56]. A known fission mediator, Dynamin-related protein 1 (Drp1), induced fission occurs early during apoptosis and right before the release of *cytochrome c* [8]. Despite regulating apoptosis by inducing mitochondrial fragmentation, Drp1 knockdown has reduced proliferation and increased spontaneous apoptosis for non-small-cell lung carcinoma [57]. Similarly, overexpression of Drp1 was associated with malignant oncocytic thyroid tumors [58].

The aggressive proliferation of cancer cells needs to be accompanied by a rapid and sufficient increase in ATP production. One prevailing mechanisms addressing this enhanced energy de-

1.1. Mitochondrial dysfunction and diseases

mand was first proposed by Otto Warburg [59]. The Warburg effect, as it is called, describes the preference of cancer cells to glycolysis over OXPHOS for ATP production [59, 60]. Despite being less efficient, glycolysis generates ATP at a faster rate compared to OXPHOS [61, 62]. Moreover, glycolysis allows cancer cells to sustain ATP production even in low oxygen level conditions. Since mitochondrial morphology is tightly linked to energy metabolism, this reprogramming of the metabolic mechanism is reflected in mitochondrial dynamics [63]. Interconnected mitochondrial networks favors respiration and OXPHOS whereas high fragmentation correlates with glycolytic metabolism [64]. Abnormalities that promote mitochondrial fission have been repeatedly observed in samples from cancer patients [63]. Increased levels of Drp1 were found with mutations associated with melanoma, thyroid, and breast cancer just to name a few [65–67]. Similarly, down-regulation of Mfn2 and optic atrophy 1 (OPA1), both of which are fusion regulating, were observed in human gastric tumors and hepatocellular carcinoma samples, respectively [68, 69].

It is evident that the resistance to apoptosis and shifting to glycolysis of cancer cells involve mitochondrial dynamics and morphology. In particular, abnormal mitochondrial fission and fragmentation seem to be common qualities of malignant tumor development. It is also true that mitochondrial dysfunction is observed in many cancer phenotypes, which may explain the preference for ATP. However, mounting evidence has shown that cancer cells have a tendency to promote glycolysis despite normal mitochondrial function while still producing significant amounts of ATP via OXPHOS [70].

Neuropathy Mitochondrial dynamics play a crucial role in the execution of energy demanding neuronal activity including synapse and neurite growth. Consequently abnormalities in various mediators of mitochondrial dynamics are correlated to a number of neurological disorders. For example, the most common cause of Charcot-Marie-Tooth (CMT) disease, which is a group of disorders causing peripheral neuropathy, is a mutation with Mfn2 [71]. Similarly, OPA1 mutation has been found in a majority of cases of dominant optical atrophy DOA [72]. The nerve damage caused by these diseases typically results in impaired movement and vision but in some cases could also lead to complete loss of function.

Huntington's Disease Disturbed mitochondrial dynamics have also been implicated in a number of neurodegenerative diseases. The Mayo Clinic defines Huntington's disease (HD) as a dominantly inherited neurodegenerative disease causing progressive breakdown of neurons in the brain. It is fatal and patients afflicted with this disease suffer through personality change, impaired and involuntary movement, dementia, and intellectual decline [73]. HD results from the repeat expansion of CAG trinucleotide in the huntingtin gene [13]. Mounting evidence has shown that reduction in number and size of mitochondria, mitochondrial ATP

Chapter 1. Mitochondrial dynamics

production, and PGC-1 α expression comes with increasing HD severity [74, 75]. HD is also accompanied by significant increase in Drp1 and decrease in Mfn2 [76]. Furthermore, mutant huntingtin gene have been known to regulate mitochondrial traffic and bind to Drp1, inducing fragmentation [16, 77].

Alzheimer's Disease Alzheimer's disease (AD), similar to HD, is also a neurodegenerative disease that causes memory loss and the overall deterioration of the patients mental faculties. It is characterized by the extracellular formation of amyloid- β plaques and intracellular neurofibrillary tangles [13]. Although not common in all cases, mutations of the amyloid- β protein precursor (APP), presenilin 1 (-PS1), or presenilin 2 (-PS2) genes involved with amyloid- β peptide production were found in AD neurons [17]. Metabolic impairment and ROS induced damage are known abnormalities that have been strongly implicated with the pathogenesis of AD [78]. Since mitochondria are the primary source of both ATP and ROS in cells, there has been a build up of evidences that alludes to the involvement of dysfunctional mitochondria and mitochondrial dynamics in the progression of AD.

Overexpression of the fission mediator Drp1 was found in both APP mutant cell lines and the postmortem brains of AD patients and AD mouse models. Moreover, this abnormal expression extends to nearly all mitochondrial fusion and fission mediating proteins including OPA1 and Mfn1/2 among others, often leading to mitochondrial fragmentation. Due to this excessive fission, mitochondria from AD brain biopsies or mouse models are often more fragmented, enlarged or swollen, and in some instances formed "beads-on-a-string" like structure [79]. This fragmented mitochondrial network found in AD models has also been attributed to oxidative stress and ROS over production [78].

ROS are a natural byproduct of ATP production by the mitochondria, which are in fact used as signaling molecules for homeostasis. However, ROS are also capable of inducing damage by oxidizing lipids and major biomolecules such as DNA and RNA [80, 81]. The intracellular ROS concentration is typically balanced between the production by mitochondria and clearance by antioxidants, but damaged or dysfunctional mitochondria are known to be less efficient in ATP generation while at the same time producing more ROS. Unfortunately, increased levels of ROS also induce mitochondrial fragmentation. This mutually promoting interaction between mitochondrial fragmentation and ROS overproduction amplifies the impact of oxidative imbalance and dysfunctional mitochondrial dynamics in AD [78].

Parkinson's Disease Genes regulating mitochondrial dynamics have been implicated in the development of Parkinson's disease (PD); these include α -synuclein, Parkin, and phosphatase and tensin homolog induced putative kinase 1 (PINK1) [42, 82]. PD is arguably one of the most common neurodegenerative disease and causes bradykinesia, rigidity, and resting

tremors caused by the loss of pigmented dopaminergic neurons [13, 73]. It is accompanied by the presence of Lewy bodies, which are abnormal aggregates predominantly composed of α -synuclein. Overexpression of the protein α -synuclein has been observed to hamper microtubule-dependent trafficking and consequently mitochondrial transport.

The rare and early onset familial PD is believed to be caused by PINK1 and Parkin mutations [83, 84]. PINK1 and Parkin act together and play an important role in mitochondrial “quality control” by regulating Miro, a component of the mitochondrial motor complex [15]. Prior to mitophagy, a damaged mitochondrion is held in position by first detaching it from its microtubule motor. This is accomplished by the PINK1-mediated Parkin phosphorylation of Miro [15]; a process that has been observed to protect dopaminergic neurons in *Drosophila* [85, 86]. Mutations in PINK1 and Parkin lead to the accumulation of damaged mitochondria and implicate the failure of mitophagy in PD development [87]. For example, PINK1 and Parkin have been observed to target Mfn2, discouraging fusion and resulting to mitochondrial fragmentation. In studies with *Drosophila*, overexpression of PINK1 significantly inhibited mitochondrial transport [15, 84]. Because neurons have highly polarized structures and rely on axonal transport to execute its functions, PINK1 and Parkin regulation of mitochondria motility may give an explanation for the peripheral neuropathy reported in some PD patients. However, despite extensive studies, a clear interpretation of the function of PINK1 and Parkin in PD remains elusive. Studies with mammalian cells have been less symptomatic and, in some instances, have provided conflicting results. Mitochondria from PINK1 or Parkin knockout human neurons have demonstrated mitochondrial fragmentation [88, 89], which could be reversed by Parkin overexpression [90] or by augmentation with Mfn2 or OPA1 [88]. Conversely, PINK1 knockout in COS-7 cells promoted mitochondrial tubulation [14, 91]. Evidently, explaining the abnormalities in mitochondrial morphology and dynamics is crucial in unveiling the mechanisms behind PD. Unfortunately, the role that PINK1 and Parkin mutations play on this is not well understood and needs to be investigated further.

1.2 Remarks

This chapter gave a brief overview of mitochondrial dysfunction and how it impacts the development of various diseases. Without a doubt, disturbed mitochondrial dynamics are detrimental to health and could explain the mechanism behind the pathogenesis of these diseases. While these studies have extensively investigated gene mutations and how they relate to abnormal mitochondrial function as well as disease symptoms, the approaches have been mostly biochemical. In recent years, the advances in super-resolution optical microscopy have given scientists a means to visualize the mitochondrial structure [20–24]. Unfortunately, it is difficult to achieve true long duration time-lapse imaging because most of this techniques are limited by photobleaching. Arguably, this limitation is the primary reason why studies

Chapter 1. Mitochondrial dynamics

approaching mitochondrial dynamics from the physics point of view where the kinetics of the mitochondria are investigated and quantified are very rare and scarce.

2 Coherence and photothermal optical coherence microscopy

The Oxford Dictionary in English defines coherence as “*the quality of being logical and consistent*”. We consider ideas and policy to be coherent if they display consistency with respect to themselves or others. Similarly, a person is deemed coherent if he or she is understandable to other people. This requires the individuals conversing to at least share the same language or background information. In other words, coherence is a measure of similarity between two entities.

Mathematically, coherence can be characterized by the normalized dimensionless cross-correlation function (CCF)

$$\gamma_{ij}(\tau) = \frac{\langle U_i^*(t) U_j(t+\tau) \rangle}{\sqrt{\langle |U_i(t)|^2 \rangle \langle |U_j(t)|^2 \rangle}} \quad (2.1)$$

where $\langle \rangle$ denotes temporal averaging, both $U_i(t)$ and $U_j(t)$ are complex functions of time varying signals, and $*$ is to indicate the complex conjugate. This correlation function quantifies the similarity between a pair of signals as a function of the time delay τ .

2.1 Interference

In physics and optics, coherence is among the fundamental properties of waves and is often described as their ability to interfere. If for example, two waves are too “dissimilar” they lose this interference property and are therefore labeled as incoherent. Light, being a wave phenomenon, is also characterized by its coherence.

Consider two stationary light fields $U_1(\mathbf{r}, t)$ and $U_2(\mathbf{r}, t)$ with constant average intensities $I_1(\mathbf{r}) = \langle |U_1(\mathbf{r}, t)|^2 \rangle$ and $I_2(\mathbf{r}) = \langle |U_2(\mathbf{r}, t)|^2 \rangle$ [92]. The superposition of these two fields at an

observation location \mathbf{r}_P results in

$$U_T(\mathbf{r}_P, t) = U_1(\mathbf{r}_P, t - t_1) + U_2(\mathbf{r}_P, t - t_2) \quad (2.2)$$

where $t_1 = \frac{r_P - r_1}{c}$ and $t_2 = \frac{r_P - r_2}{c}$ are defined as the durations needed for the fields traveling at the speed of light c to propagate from their sources at \mathbf{r}_1 and \mathbf{r}_2 respectively. The observed interference is given by the time averaged total intensity

$$\begin{aligned} I_T(\mathbf{r}_P) &= \langle |U_T(\mathbf{r}_P, t)|^2 \rangle \\ &= I_1(\mathbf{r}_P) + I_2(\mathbf{r}_P) + \langle U_1^*(\mathbf{r}_P, t') U_2(\mathbf{r}_P, t' + \tau) \rangle + \langle U_1(\mathbf{r}_P, t') U_2^*(\mathbf{r}_P, t' + \tau) \rangle \end{aligned} \quad (2.3)$$

with the variable substitutions $t' = t - t_1$ and $\tau = t_1 - t_2$. It is obvious from Eq. 2.3 that the interference terms share the same form as the cross-correlation function (Eq. 2.1). This illustrates how interference is the phenomenon of correlating waves and coherence is a measure of how well these fields interfere. In fact, $\langle U_1^*(\mathbf{r}_P, t') U_2(\mathbf{r}_P, t' + \tau) \rangle$ is referred to as the mutual coherence function and Eq. 2.3 can be rewritten as

$$I_T(\mathbf{r}_P) = I_1(\mathbf{r}_P) + I_2(\mathbf{r}_P) + 2\sqrt{I_1(\mathbf{r}_P)I_2(\mathbf{r}_P)}\text{Re}\{\gamma_{12}(\tau)\}, \quad (2.4)$$

using the real part of the normalized mutual coherence function, also known as the complex degree of coherence $\gamma_{12}(\tau)$, to represent the interference term [92]. For the case of interfering fields from the same source separated by a time delay τ , $\gamma_{12}(\tau)$ transforms into the normalized autocorrelation function $\gamma(\tau) = \frac{\langle U^*(t)U(t+\tau) \rangle}{\sqrt{\langle |U(t)|^2 \rangle}}$, which characterizes the temporal coherence of the source [92]. $|\gamma(\tau)|$ takes on values from 0 to 1 describing the boundary conditions of perfect incoherence and coherence respectively. In reality, all light sources display a certain degree of partial coherence and $|\gamma(\tau)|$ generally decays with increasing τ . To quantify the temporal coherence of a light source, we define the coherence time τ_c [92] as

$$\tau_c = \int_{-\infty}^{\infty} |\gamma(\tau)|^2 d\tau. \quad (2.5)$$

Consequently, the coherence length l_c is defined as the distance light travels for a duration equivalent to τ_c or simply $l_c = c\tau_c$. Through the years, interferometric imaging techniques have capitalized on the coherent nature of light to improve resolution, sensitivity, as well as to develop novel contrast mechanisms.

2.2 Frequency domain optical coherence tomography (FDOCT)

Optical coherence tomography (OCT) is a three-dimensional imaging method based on low-coherence interferometry. The broadband light sources used in low-coherence interferometry have finite coherence lengths allowing them to perform depth sectioning. OCT systems are

2.2. Frequency domain optical coherence tomography (FDOCT)

able to resolve individual scatterers in depth as long as they are separated by more than the coherence length l_c ; this ability is called coherence gating. For a broadband light source with a Gaussian spectral profile centered at λ_0 and bandwidth $\Delta\lambda$, the depth resolution δz is given by

$$\delta z = \frac{l_c}{2n} = \frac{2\ln 2}{n\pi} \frac{\lambda_0^2}{\Delta\lambda}. \quad (2.6)$$

where n is the index of refraction of the sample [93]. Similar to other interferometric techniques, OCT splits the light into the reference beam and the illumination or sample beam. OCT collects the backscattered light from the sample and superimposes it with the reference beam. One advantage of this interferometric detection scheme is the ability to adjust the reference beam power to boost the collected signal independent of the illumination. By taking advantage of this coherent amplification, OCT has consistently demonstrated its effectiveness for imaging weakly scattering biological samples. Furthermore, the contrast of OCT stems from the intrinsic scattering properties of the sample. These qualities, high sensitivity, three-dimensional imaging capability, and label-free nature, of OCT have helped it establish a niche in the field of biomedical imaging.

Initially, however, OCT systems were slow and required three-dimensional scanning to acquire full volumetric images. In 1995, Fercher et al. proposed using a spectrometer to record the interferogram spectrum which resulted in the invention of frequency domain OCT (FDOCT) [94]. The acquired interference spectrum $I_{spec}(k)$ would be the coherent sum of all backscattered fields $E_s(k, t) = E_0(k) \sum_{i=1}^N \alpha_i e^{i(kz_i - \omega t)}$ and the reference field $E_r(k, t) = E_0(k) e^{i(kz_r - \omega t)}$

$$\begin{aligned} I_{spec}(k) &= \left\langle \left| E_0(k) \alpha_r e^{i(kz_r - \omega t)} + E_0(k) \sum_{i=1}^N \alpha_i e^{i(2kz_i - \omega t)} + c.c. \right|^2 \right\rangle \\ &= |E_0(k)|^2 \left[\alpha_r^2 + \sum_{i=1}^N \alpha_i^2 + \sum_{i \neq j=1}^N \alpha_i \alpha_j \cos(2k(z_j - z_i)) + \sum_{i=1}^N \alpha_i \alpha_r \cos(k(z_r - 2z_i)) \right] \end{aligned} \quad (2.7)$$

where α_r and α_i are the effective reflectivities of the reference arm with length z_r and each scatter in the sample located at z_i along the axial direction. The first two terms are the DC components while the third term represents the interference between the different scatterers; typically, $\alpha_i \ll \alpha_r$ meaning the third term can be neglected. The final term stands for the cross-correlation between the sample and reference fields and allows us to determine the position z_i of the different scatters within the depth of field (DOF). This significantly decreases the acquisition time of OCT because the full depth information is already encoded in this spectrum. It would only require an inverse Fourier transform to retrieve the depth profile and therefore, FDOCT systems only need 2D raster scanning to acquire full 3D tomograms.

2.3 Optical coherence microscopy (OCM)

Optical coherence microscopy (OCM) is the high resolution implementation of OCT. It makes use of high numerical aperture (NA) optics to achieve submicron resolution $\delta r \propto \frac{\lambda_0}{NA}$ ideal for imaging samples at the cellular level. However, improving spatial resolution by focusing Gaussian beams comes with a corresponding decrease in DOF $\propto \frac{\lambda_0}{NA^2}$. As a consequence, z -scanning would again be necessary to achieve full 3D imaging. This presents OCM with a fundamental trade-off between speed and high resolution imaging. A number of OCT/OCM instruments have tried to address this limitation. One instrument that is of particular interest for this thesis is the extended-focus OCM (xfOCM) [27].

xfOCM circumvents the reduced DOF of focused Gaussian beams by exchanging it with a Bessel-like illumination beam [27]. The Bessel-beam is a solutions to the Helmholtz equation, which predicts a beam that maintains its lateral profile over a large propagation distance. In practice, the xfOCM uses a Bessel-like beam to illuminate the sample with a light needle that preserves its beam width over an extended depth despite focusing with a high NA objective. The xfOCM has been used in longitudinal *in vivo* imaging studies which revealed the progression of diabetes [28–32] and Alzheimer’s disease [33] in their respective mouse models. Quantitative blood flow imaging with the xfOCM has also been done [95, 96] and was applied to statistical parametric mapping of mouse cortex blood flow response to stimuli [97]. Dark-field OCM (dfOCM) is a variant of the xfOCM featuring enhanced contrast for imaging weakly scattering samples such as cells [34]. The separate illumination (Bessel-beam) and detection (Gaussian beam) modes of the xfOCM makes dark-field imaging readily accessible by adding a circular mask to discard specular reflection.

2.4 Photothermal optical lock-in OCM

As previously mentioned, the contrast of OCM imaging is obtained from the variations of the refractive index within a sample. Because it is based on elastic scattering and coherent detection, OCM cannot take advantage of the fluorescent labels extensively used by other microscopy techniques (confocal, super-resolution, etc.). Despite consistently displaying high sensitivity and speed, this lack of specificity hinders OCM’s further involvement in biological studies at the cellular level. Instead of fluorescence, photothermal contrast is an appealing alternative for specific OCM imaging since it utilizes local perturbation of the sample’s refractive index.

Photothermal contrast is based on the conversion of light energy into heat. Most photothermal microscopes use labels that absorb energy from a heating beam and dissipate heat into their immediate vicinity [98]. This interaction causes an increase in temperature of the surrounding medium, which consequently alters the local index of refraction and expansion [98, 99].

2.4. Photothermal optical lock-in OCM

Photothermal contrast is achieved by using a separate probe beam to detect this change in scattering properties. One way of implementing photothermal imaging is by using an intensity modulated heating beam at a defined frequency Ω . This modulated heating generates synchronously modulated backscattered fields which can then be selectively filtered via lock-in detection.

According to Gaiduk et al. [99], the change in temperature $\Delta T(r, t)$ caused by the photothermal effect with a sinusoidally modulated heating beam is described by

$$\Delta T(r, t) = P_{diss} \frac{1}{4\pi\kappa r} \left(1 + \exp\left(-\frac{r}{r_{th}}\right) \cos\left(\Omega t - \frac{r}{r_{th}}\right) \right) \quad (2.8)$$

where κ is the medium's thermal conductivity and the dissipated power $P_{diss} = P_{heat} \frac{\sigma_{abs}}{A}$ is defined by the power of the heating beam P_{heat} and the ratio of its diffraction limited spot size A with the absorption cross section σ_{abs} of the photothermal label. Finally, the extent of heat diffusion is characterized by the thermal radius r_{th}

$$r_{th} = \sqrt{\frac{2\kappa}{\Omega C_p}} \quad (2.9)$$

using the heat capacity per unit volume C_p of the medium. Assuming the refractive index change with respect to temperature as $\frac{\partial n}{\partial T}$, the effective photothermal scattering signal is given by

$$S \approx \frac{1}{\pi\omega_0 C_p \lambda^2 \Omega} n \frac{\partial n}{\partial T} \frac{\sigma_{abs}}{A} P_{heat} P_{probe} \Delta t \quad (2.10)$$

where Δt is the detector integration time and ω_0 , λ , and P_{probe} are the waist, wavelength, and power of the probe beam respectively. In general, P_{heat} , P_{probe} , and Δt are accessible system parameters that can be adjusted to improve imaging performance.

In 2012, Pache et al. demonstrated fast three-dimensional imaging of gold nanoparticles (AuNP) in highly scattering media and living cells with the invention of photothermal optical lock-in OCM (poli-OCM) [100]. In addition to the intensity modulated photothermal heating beam, poli-OCM uses a pair of acusto-optic modulators (AOM) to add linear phase modulation to the reference beam, enabling optical lock-in detection [100]. Pache et al. approximated the field backscattered by the volume surrounding the AuNP as

$$E_{AuNP}(k, t) = \alpha_{AuNP} E_0(k) e^{ik(2z_{AuNP} + \epsilon \cos(\Omega t)) - i\omega t} \quad (2.11)$$

and the reference beam by

$$E_r(k, t) = \alpha_r E_0(k) e^{i(kz_r - (\omega + \Omega)t - \phi)} \quad (2.12)$$

Chapter 2. Coherence and photothermal optical coherence microscopy

where the α 's are the effective reflectivities, E_0 is the amplitude of the input beam, Ω is again the modulation frequency, and ε is a parameter for the thermally induced path length modulation. The effective photothermal signal comes from the interference of these two fields integrated over an integer multiple of integration time $T = m\Delta t$ of the spectrometer

$$\begin{aligned}
 I_{poli}(k) &= |E_0(k)|^2 \alpha_r \alpha_{AuNP} e^{ik(z_{AuNP} - z_r) - i\varphi} \int_0^T e^{-i(\varepsilon \cos(\Omega t) - \Omega t)} dt + c.c. \\
 &\approx |E_0(k)|^2 \alpha_r \alpha_{AuNP} \varepsilon k T \sin(2k(z_{AuNP} - z_r) - \phi), \quad \text{for } \varepsilon k \ll 1.
 \end{aligned} \tag{2.13}$$

As stated in [100] and similar to Eq. 2.10, the photothermal signal is proportional to the scattering by an effective volume defined by the integral of the modulated refractive index variation around the AuNP. In Eq. 2.13 this photothermal interaction is represented by ε such that $\varepsilon \propto P_{heat} \frac{\sigma_{abs}}{A}$. This pioneering work demonstrated the possibility of highly sensitive and specific poli-OCM imaging in living without cells sacrificing speed [100]. Furthermore, one particular advantage of photothermal imaging, as opposed to fluorescence, is the photostability of its markers. AuNPs, like most photothermal labels, are not susceptible to photobleaching making them ideal for long term time-lapse imaging of living cells.

3 Gold nanoparticle functionalization and mitochondria imaging

Specific imaging for biological samples is most often achieved by attaching a fluorophore to the structure or molecule of interest. The spectral separation between the excitation and emission of these fluorophores enables selective filtering of the desired signal. To this date, confocal fluorescence microscopy is arguably the most widely used intracellular imaging technique and numerous organic dyes, fluorescent proteins, and quantum dots have been developed to further its use. Unfortunately, no counterpart is available for coherent imaging techniques based on elastic scattering like OCM. As previously elaborated, photothermal imaging using AuNPs as contrast agents offers a promising alternative; particularly because of the unique combination of properties AuNPs possess.

The high stability and low toxicity of AuNPs are among their qualities important for biological application. The high oxidation potential of gold makes it more stable compared to other metals even in an aqueous environment [101]. Furthermore, cells and other biological samples have consistently demonstrated high tolerance and survivability despite prolonged exposure to AuNPs alluding to the biocompatibility of colloidal AuNPs [102, 103].

Moreover, AuNPs are “very small” by definition. They typically have dimensions that are in the same order of magnitude or smaller compared to organelles and other intracellular structures. This is of particular significance since, labels should be small enough not to mechanically perturb the activity of the molecule it attaches to. In addition, larger particles ($> 10^2$ nm) are known to have difficulty passing through cellular membranes [101].

AuNPs also display highly localized enhancement of electromagnetic fields upon illumination by ultraviolet (UV) to near infrared (NIR) light. This field enhancement is a direct consequence of the resonant oscillations of free electrons at the interface of a metal conductor and a dielectric (e.g. air, water, etc.). Referred to as surface plasmons, these oscillations are highly localized in the case of AuNPs because their dimensions are much smaller than the wavelength

Chapter 3. Gold nanoparticle functionalization and mitochondria imaging

of the exciting field [104, 105]. Because of this localized field enhancement, molecules situated in the near vicinity of the AuNPs experience intensities much higher than the initial incident illumination. This phenomenon is the basis for techniques like surface enhanced Raman spectroscopy (SERS) and fluorescence (SEF) [106]. At their surface plasmon resonance, AuNPs have a large absorption cross section, which, in addition to their efficiency in converting absorbed light into heat, make AuNPs ideal photothermal contrast agents [107–109]. The peak wavelength of AuNPs surface plasmon resonance typically lies in the green band (≈ 530 nm) of the visible spectrum. However, it has been repeatedly demonstrated that the peak and broadness of this resonance can be adjusted over a wide wavelength range (UV-NIR) depending on the geometry and material compositions of the AuNP core and shell [110–112]. This tunability grants AuNPs the possibility for simultaneous multicolor labeling and imaging.

This collection of physical and chemical characteristics of AuNPs places them in an ideal position for bioimaging and biomedical applications. This has been demonstrated time and again in photothermal therapy [113, 114] as well as by the use of AuNPs as biomarkers and nanoscale biosensors [115, 116]. However, to accomplish these tasks, it is crucial to functionalize the surface of AuNPs with coatings made up of ligands, proteins, peptides etc. [117–119]. These coatings improve the AuNP's biocompatibility, cellular uptake, and stability in physiological media. Moreover, surface functionalization using specific molecules grants AuNPs with the custom characteristics for applications such as targeting or labeling of organelles. In our experiments we are particularly interested in using AuNPs as mitochondria targeting photothermal markers for specific poli-OCM imaging.

3.1 Multifunctional copolymer coated AuNPs for poli-OCM imaging

Parts of this section were published in: Biomaterials Science 5, 966-971 (2017)

In this study, we synthesized photothermally active AuNPs functionalized with a versatile polypeptide copolymer for mitochondria imaging with the poli-OCM. The synthesis of this multifunctional polypeptide was based on the blood plasma protein human serum albumin (HSA) which served as the precursor. The available carboxylic acid groups of HSA were converted to primary amino groups yielding polycationic HSA (cHSA) [120]. The conversion into cHSA enhances surface attachment and improves cellular uptake due to the electrostatic interactions [121]. Furthermore, cHSA has an increased number of reactive sites allowing for more chemical modifications. Denaturing cHSA resulted in dcHSA whose thiol groups were then reacted with polyethylene oxide (PEO) side chains for water-solubility and to reduce nonspecific interactions [120, 122]. N-Hydroxy-succinimide activated maleimide (MI-NHS) was then reacted with the dcHSA-PEO hybrid in pH 7.4 PBS buffer. Next, this newly introduced

3.1. Multifunctional copolymer coated AuNPs for poli-OCM imaging

maleimide group was reacted with the terminal thiol of the cysteine (Cys) residue of TAT (SH-Cys-Gly-Tyr-Gly-Arg-Lys-Lys-Arg-Arg-Gln-Arg-Arg-Arg) yielding dcHSA-PEO-TAT. The addition of several copies of the TAT peptide improved uptake into mammalian cells and enhanced endosomal escape. Mitochondria targeting was provided by the lipophilic cation triphenyl-phosphonium (TPP), widely known for its selective accumulation in mitochondria. [123]. Finally, hydrophobic TPP cations were attached following the EDC-NHS ester coupling reaction to yield the dcHSA-PEO-TAT-TPP bioconjugate.

This multifunctional polypeptide copolymer we synthesized imparts excellent water solubility, biocompatibility, and stability under various physiological conditions. AuNPs coated with this copolymer are well suited for time-lapse photothermal imaging with poli-OCM. Furthermore, this multifunctional copolymer platform offers the possibility of Au-nanotransporters, traceable via imaging, that are capable of delivering cargos such as drugs to specifically targeted organelles or cell compartments. In this particular case, the AuNPs were designed for mitochondria specific imaging.

We investigate the optimum labeling condition of our functionalized AuNPs for poli-OCM imaging. We approach this by incubating HeLa cells with increasing concentrations of AuNPs. For each of the concentration we evaluate the strength of the measured poli-OCM signal. HeLa cells were seeded onto Ibidi μ -slide 8-well (\approx 2000–4000 cells per well) with 250 μ L of cell culture medium (Dulbecco's Modified Eagle Medium (DMEM), 10% fetal bovine serum, and 1% penicillin and streptomycin antibiotics). The cells were given sufficient time (\geq 12 hrs.) to adhere to the substrate before replacing the medium with a fresh batch containing different concentrations of the dcHSA-PEO-TAT-TPP functionalized AuNPs for each well. We investigated five concentrations: 2.77, 6.84, 13.42, 31.7, and 58.2 nM. The cells were incubated overnight to allow sufficient uptake of the AuNPs. Prior to imaging, the cells were washed $3\times$ with PBS, removing the excess AuNPs, then fresh culture medium was added. In addition, we costained the cells with MitoTracker Deep Red at 10nM for simultaneous dfOCM and fluorescence imaging. This was done to control the AuNP labeling of the mitochondria, ensuring that the difference in poli-OCM signal was not due to significant variations in the mitochondria content among cell cultures. Imaging was conducted using a 532 nm laser as the photothermal heating beam with an average power of 3 mW. Sample images from these cell cultures are shown in Fig. 3.1. Each row features a set of dfOCM, poli-OCM and fluorescence images arranged in increasing AuNP labeling concentrations from top to bottom.

The dfOCM images (Fig. 3.1 left column) are single en-face sections (cross-sectional slices) from complete three-dimensional tomograms featuring the complete cell morphology. The dfOCM contrast is based on the backscattering induced by variations of the refractive index and we clearly notice regions inside the cell with weak and strong signals. Although dfOCM imaging does not offer specific information, we associate the weakly scattering regions with

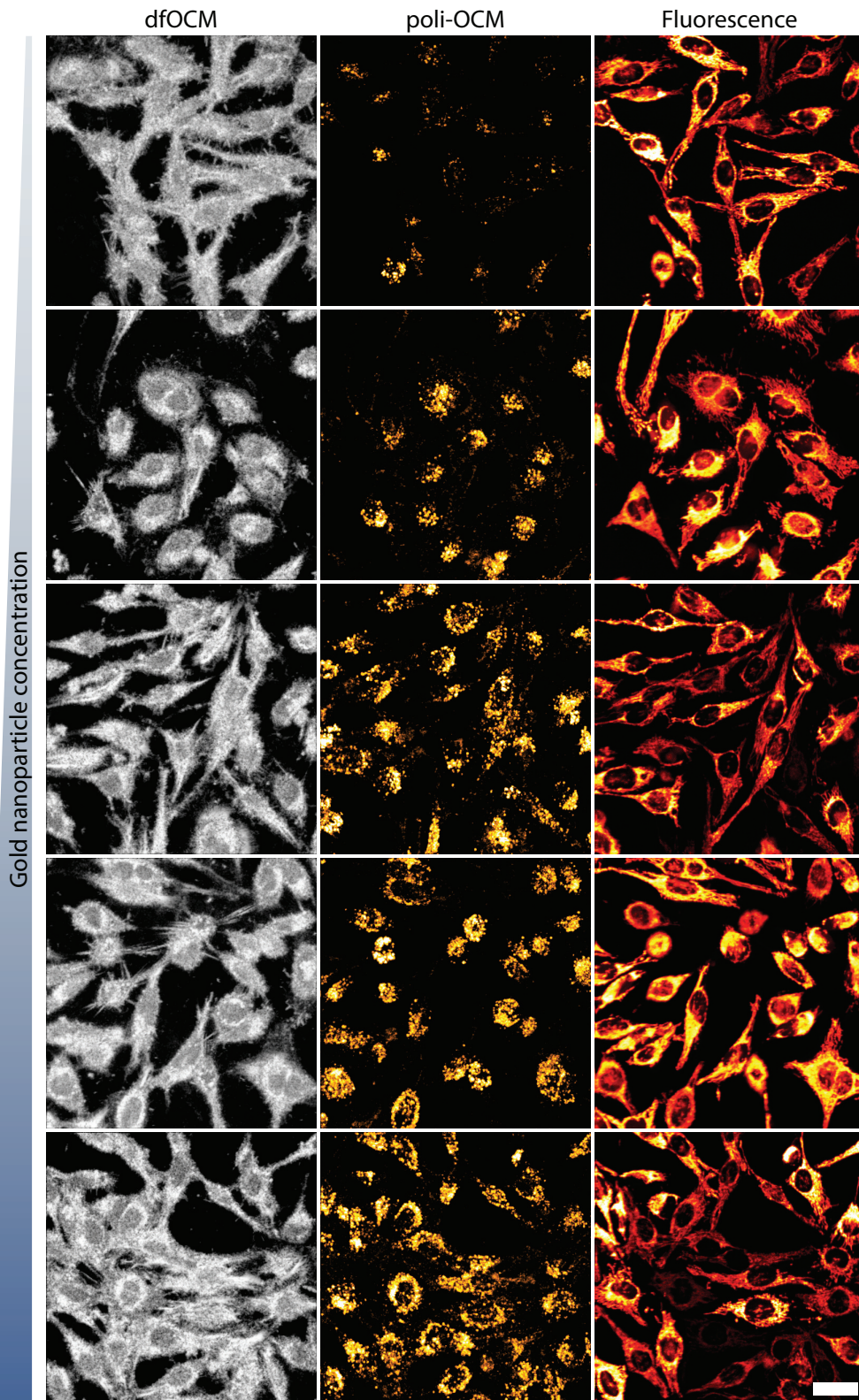


Figure 3.1 – dfOCM, poli-OCM, and fluorescence images of HeLa cells incubated with increasing concentration of mitochondria targeting AuNPs. Going from top do bottom the concentration are 2.77, 6.84, 13.42, 31.7, and 58.2 nM. The HeLa cells were co-stained with MitoTracker Deep Red at 10nM for fluorescence imaging. Scalebar: 25 μ m

3.1. Multifunctional copolymer coated AuNPs for poli-OCM imaging

the cell nucleus. This appears to be a good assumption since this weakly scattering region coincides with parts of the cell not labeled by both the AuNPs and MitoTracker.

The middle column of Fig. 3.1 displays maximum intensity projections along the z-direction of three-dimensional poli-OCM tomograms depicting the presence of AuNPs attached to mitochondria. With regards to the effect of varying the amount of functionalized AuNPs, the series of poli-OCM images clearly illustrates an increase in number of AuNP-labeled mitochondria with higher labeling concentrations. In fact, for the lowest AuNP concentration (2.77 nM) the poli-OCM signal was nearly negligible. On the other hand, from 13.4 nM and above the poli-OCM images show that mitochondria of the entire cell culture were almost completely labeled by the AuNPs.

The corresponding fluorescence images on the right column indicates two things. First, there is clearly a good agreement between the fluorescence imaging with MitoTracker and poli-OCM imaging with the functionalized AuNP demonstrating the specificity of the AuNPs for mitochondria targeting. We further confirm this in [124] where we show a Pearson's colocalization coefficient of 0.89 between MitoTracker and dHSA-PEO-TAT-TPP AuNP labeling. Second, the fluorescence images confirm that there is no noticeable difference with the mitochondria content among the cell cultures and the increase in poli-OCM signal is indeed due to the AuNP concentrations.

We characterized the increase in poli-OCM signal in response to the AuNP labeling concentration by evaluating the distribution of measured signal intensities. For each labeling concentration we acquired a set of three poli-OCM tomograms from different locations in the well. From these tomograms, we subsequently generated histograms showing the distribution of poli-OCM signal intensities (Fig. 3.2). These distributions were normalized to the total number of voxels that had good poli-OCM signal-to-noise for each labeling concentration. This was done to ensure that we are in fact comparing signal strength and quality while avoiding a bias due the number of AuNP labeled mitochondria. The histograms in Fig. 3.2 as well as their mean values show that, as expected, higher AuNP concentrations also gave stronger poli-OCM signals. However, it is interesting to point out that the dependence of poli-OCM signal with labeling concentration is not linear. Inspecting either Eqs. 2.10 or 2.13 we notice that this was evaluated for a single photothermal absorber. Furthermore, the strength of the photothermal signal is, in general, proportional to the absorption cross-section σ_{abs} and not the number of photothermal absorbers within the diffraction limited spot size of the heating beam. Moreover, interaction of plasmonic particles that are too close to each other induce a red-shift with their plasmonic resonance [125, 126] that could, in effect, decrease their absorption efficiency.

Chapter 3. Gold nanoparticle functionalization and mitochondria imaging

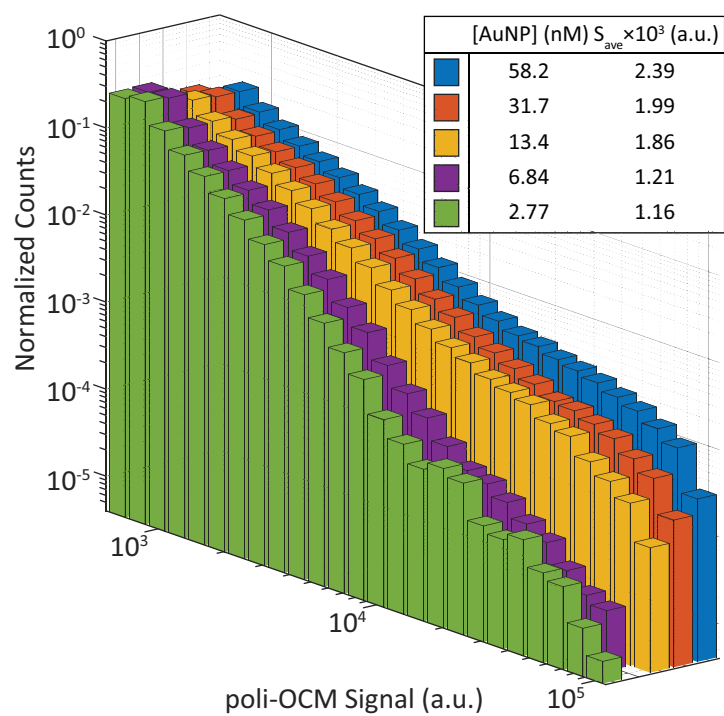


Figure 3.2 – Normalized histogram of poli-OCM signal for increasing the AuNP concentrations in logarithmic scale

3.2 Mitochondria imaging with various Au-nanostructures

Parts of this section were published in: Nano Letters **16**(10), 6236-6244 (2016)

We further demonstrate mitochondria specific poli-OCM imaging with different surface functionalization and other gold nanostructures. In particular we imaged HeLa cells with mitochondria labeled using AuNPs and gold nanorods (AuNRs) functionalized with globular cBSA-TPP. This surface coating is based on polycationic bovine serum albumin (cBSA) with mitochondria targeting provided by the same TPP molecule as with the dcHSA-PEO-TAT-TPP copolymer. Surface functionalization using the globular cBSA-TPP as coating provided the AuNPs with improved cell uptake, stability in biological media, and biocompatibility on top of mitochondria targeting. Despite having fewer functional groups compared to dcHSA-PEO-TAT-TPP coating, we were able to achieve sufficient AuNP mitochondria labeling at a much lower concentration of 0.31 nM. The specifics of synthesizing globular cBSA-TPP are discussed in 4.1.2.

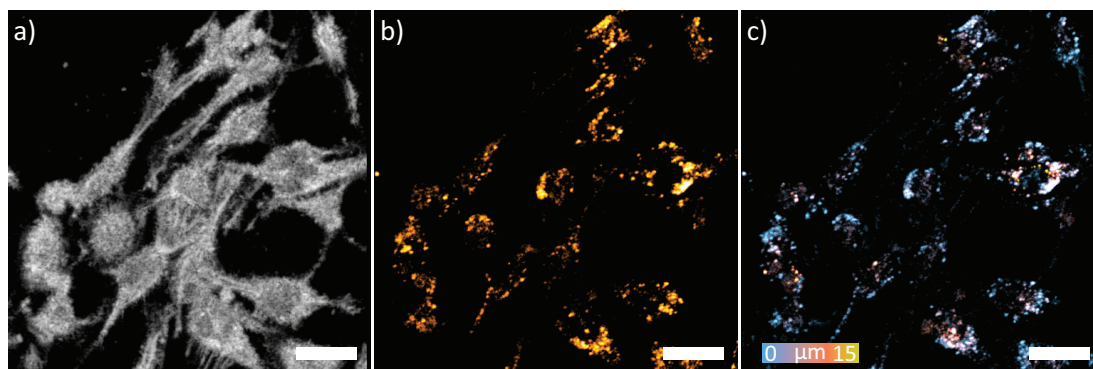


Figure 3.3 – Cross-sectional slices of a) dfOCM and b) poli-OCM tomograms showing the complete cell and the AuNP-labeled mitochondria respectively. c) Maximum intensity projection with the color indicating depth information. Scalebar: 25 μ m

dfOCM and poli-OCM images of HeLa cells with AuNP-labeled mitochondria are shown in Fig. 3.3. The AuNPs were functionalized with globular cBSA-TPP AuNPs and have 3.7 ± 0.9 nm diameter. Similar to 3.1 the dfOCM images is a slice from the full three-dimensional tomogram showing the complete cell and the distinguishable weaker scattering of the nucleus. The two poli-OCM images are a single slice (Fig. 3.3b) and a maximum intensity projection along the z-direction (Fig. 3.3c) with the depth position encoded in the color. Fig. 3.4 features similar images as Fig. 3.3 but with HeLa cell mitochondria labeled with AuNRs instead of AuNPs. The AuNRs had dimensions of 95.2 ± 10.8 nm in length and 51.3 ± 9.5 nm in width resulting in plasmonic resonance peaks at ≈ 530 nm and ≈ 650 nm.

Lastly, we also attempted using fluorescent nanodiamond and AuNP dimers (fND-AuNP) for poli-OCM imaging (3.5). This fND-AuNP dimer is representative of “all-in-one” hybrid

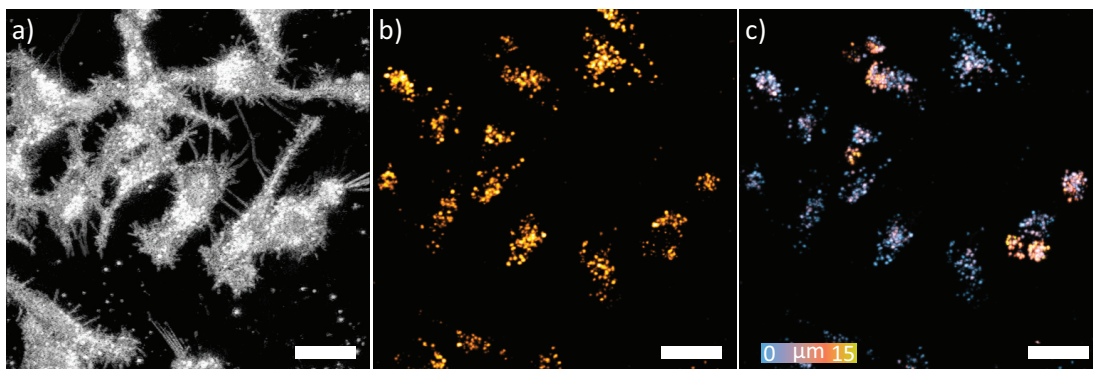


Figure 3.4 – Cross-sectional slices of a) dfOCM and b) poli-OCM tomograms showing the complete cell and the AuNR-labeled mitochondria respectively. c) Maximum intensity projection with the color indicating depth. Scalebar: $25\mu\text{m}$

particles uniquely designed for multimodal cellular imaging. The fluorescence of the ND can be used as a marker for confocal microscopy while the AuNP is useful for photothermal imaging as well as for electron microscopy [127]. This new class of nanoparticles offers the possibility of specificity for both established and emerging techniques across multiple imaging technologies.

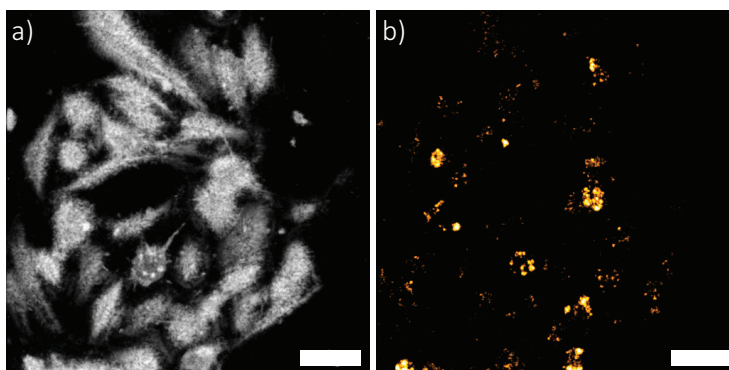


Figure 3.5 – Cross-sectional slices of a) dfOCM and b) poli-OCM tomograms showing the complete cell and mitochondria labeled with the fND-AuNP respectively. Scalebar: $25\mu\text{m}$

3.3 Summary

We have discussed the advantages of using AuNPs as bio-markers for specific intracellular imaging. In particular, AuNPs have a unique combination of properties that make them the ideal labels for photothermal imaging. Compared to other metals, AuNPs are stable in aqueous and biological media, have a low degree of cytotoxicity, and do not photobleach. Furthermore, the plasmonic resonance of the AuNPs can be adjusted by altering their size, geometry, and

composition giving us the ability to design AuNP labels suitable for our imaging system as well as to use multiple labels for multicolor photothermal imaging.

We also discussed the synthesis and characterization of mitochondria specific AuNP labels with a novel multifunctional copolymer coating. This copolymer was based on the blood plasma protein human serum albumin (HSA) with attached TPP molecules for mitochondria targeting. In addition, this multifunctional copolymer platform can be used as traceable nanotransporters since they can be functionalized for delivery and imaged at the same time. For our experiments, these AuNPs were designed to target the mitochondria for specific poli-OCM imaging. We optimized the AuNP labeling condition for these AuNPs by incubating the HeLa cells with different concentrations of AuNP labels and evaluating the poli-OCM signal. Our results show that the strength of the poli-OCM signal is not linearly dependent on AuNP labeling concentration. Increasing the AuNP labeling concentration above 13 nM does not seem to improve the poli-OCM imaging performance.

In the last section of this chapter, we demonstrated the possibility of specific poli-OCM imaging using other kinds of AuNPs and different polymer coatings. We imaged HeLa cells with mitochondria targeting Au-nanospheres and Au-nanorods functionalized with a surface coating based on polycationic bovine serum albumin; mitochondria targeting was again provided by attaching TPP molecules. Finally, we also imaged HeLa cells incubated with fluorescent nanodiamond and AuNP dimers. This unique dimer can be considered an “all-in-one” hybrid particle which can be used for multimodal cellular imaging. The same dimer can be used as a label in fluorescence confocal, electron, and photothermal microscopy [127].

4 Quantification of mitochondrial dynamics

There are a number of techniques that were developed to probe and measure dynamic properties of a system. One particular technique that has been extensively used in both biology and chemistry is fluorescence correlation spectroscopy (FCS) [128]. FCS quantifies the dynamics of a system by measuring the fluctuations of its fluorescence intensity signal [36]. In its first implementation, Magde et al. used FCS to quantify the chemical rate constants and diffusion coefficients of the binding process between ethidium bromide and double stranded DNA [36]. The use of FCS became more prominent upon the development of confocal microscopy and the merging of the two techniques [129]. The use of confocal illumination and detection provided FCS with the necessary sensitivity to probe biological interactions at physiological concentrations. Since then, FCS has emerged as one of the most well-established techniques adapted for cell biology and biophysics. There have been numerous variants of FCS each aimed at improving its effectiveness for specific applications. Dual-focus FCS utilizes a pair of overlapping detection foci which serves as an external length to overcome the limitation introduced by the size of the PSF [130]. Fluorescence cross-correlation spectroscopy is another variant, which is basically a dual color FCS implementation that allows us to observe two different fluorescent species [131]. FCCS is particularly capable for probing molecular reactions between a pair of uniquely labeled reactants. Newer FCS based techniques have also exploited the recent advancement of super resolution imaging techniques [132–134]. One variant of FCS that is of particular interest in this thesis is temporal image correlation spectroscopy (ICS) [135]. As the imaging analogue of FCS [135], temporal ICS averages over space and thereby achieves statistical significance without needing to acquire fluorescence fluctuations on the same focal spot for a long time. This makes temporal ICS well suited to quantify the dynamics of nearly static or slowly diffusing particles.

In the succeeding section of this chapter we demonstrate quantification of mitochondrial dynamics by extending ICS to three-dimensional poli-OCM imaging of AuNP labeled mitochondria. Our method is based combining temporal autocorrelation analysis and a classical

Chapter 4. Quantification of mitochondrial dynamics

diffusion model to extract spatially resolved diffusion parameters, which we can map in three-dimensions. Subsequently, we elaborate on the possible issues introduced by the non-negligible size of mitochondria compared to the focal volume of the poli-OCM. In the last section, we propose single particle tracking as a complementary technique for quantifying mitochondrial dynamics

4.1 3D time-lapse imaging and quantification of mitochondrial dynamics

Journal article

Published in: Scientific Reports 7, Article number: 43275 (2017).

3D Time-lapse Imaging and Quantification of Mitochondrial Dynamics

Miguel Sison^{1*}, Sabyasachi Chakraborty^{2,3*}, Jérôme Extermann^{1,4}, Amir Nahas¹, Paul James Marchand¹, Antonio Lopez¹, Tanja Weil^{2,3}, Theo Lasser¹

* These authors contributed equally to this work.

¹Laboratoire d'Optique Biomédicale, École Polytechnique Fédérale de Lausanne, 1015 Lausanne, Switzerland ²Department of Organic Chemistry III/Macromolecular Chemistry, Ulm University, Albert-Einstein-Allee 11, 89081 Ulm, Germany ³Max-Planck-Institute for Polymer Research, Ackermannweg 10, 55128 Mainz, Germany ⁴Hepia, University of Applied Sciences of Western Switzerland (HES-SO), 4 rue de la Prairie, CH-1202 Genève, Switzerland

We present a 3D time-lapse imaging method for monitoring mitochondrial dynamics in living HeLa cells based on photothermal optical coherence microscopy and using novel surface functionalization of gold nanoparticles. The biocompatible protein-based biopolymer coating contains multiple functional groups which impart better cellular uptake and mitochondria targeting efficiency. The high stability of the gold nanoparticles allows continuous imaging over an extended time up to 3000 seconds without significant cell damage. By combining temporal autocorrelation analysis with a classical diffusion model, we quantify mitochondrial dynamics and cast these results into 3D maps showing the heterogeneity of diffusion parameters across the whole cell volume.

4.1. 3D time-lapse imaging and quantification of mitochondrial dynamics

4.1.1 Introduction

Mitochondria are organelles present in most eukaryotic cells. They are important for sustaining the energy needs of the host cell via the synthesis of ATP [1]. Besides being the cellular powerhouse, mitochondria are also involved in synaptic transmission and cellular signaling [136]. These fundamental functions translate into continuous mitochondria trafficking, which is an essential characteristic of these organelles, best subsumed by the term “mitochondrial dynamics” [11]. Quantifying these dynamics over a large time span promises to deepen our insight on cellular processes tightly related to neurodegenerative diseases such as Alzheimer’s and Parkinson’s disease [1, 137–139].

Confocal fluorescence microscopy remains the most widely used technique for cellular imaging. It provides high spatial resolution and specificity, known from fluorescent markers, making it suitable for intracellular imaging and studying mitochondria morphology. However, available fluorescent markers are prone to photobleaching, such as organic dyes, or are inherently toxic, like quantum dots [25, 26], limiting their viability for long-lasting live cell imaging.

Light-sheet microscopy is a fast, 3D, and high resolution intracellular imaging technique that also addresses photobleaching. In particular, Planchon, T. A. et al. [140] demonstrated imaging live-cell mitochondrial dynamics using a scanned Bessel beam. Live pig kidney epithelial cells (LLC-PK1 cell line) were imaged over 300 volume stacks displaying a decrease in fluorescence intensity of only <20%. Among these techniques, probably the most advanced is lattice light-sheet microscopy by Chen, B.-C. et al. [141] where imaging mitochondrial dynamics for more than 18 minutes was achieved with limited photobleaching. Undoubtedly, light-sheet microscopy has succeeded in pushing the bounds of intracellular imaging. However, it still relies on fluorescence probes and will eventually be confronted with the same limitations.

The use of gold nanoparticles (AuNPs) as biomarkers for photothermal imaging offers a promising alternative because of their high stability and very low toxicity. However, to accomplish photothermal imaging inside living cells, it is crucial to stabilize the surface of the AuNPs with water-soluble, biocompatible ligands that can withstand various physiological conditions. Stability of the AuNPs at varying pH and in the presence of proteases located in vesicles during endosomal uptake processes or in the reductive environment in the cytoplasm are essential to provide suitable intracellular markers for time lapse studies [142]. Protein based polymeric surface coatings offer the additional advantage as multiple functionalities could be incorporated at the level of the polymer. This ensures characterization by standard polymer analytics and guarantees the presence of all required functions at the particle surface after coating [143]. In this way, photothermal imaging AuNPs could be envisaged carrying the desired functionalities for targeting sub-cellular organelles, such as mitochondria, inside living cells.

The photothermal contrast mechanism relies on a temporally modulated refractive index in

Chapter 4. Quantification of mitochondrial dynamics

the near vicinity of the AuNPs resulting from heat dissipated by the AuNPs' plasmon-enhanced absorption. This contrast mechanism is the basis for photothermal optical lock-in optical coherence microscopy (poli-OCM), which provides two distinct imaging modalities: a dark-field mode (dfOCM) for imaging the 3D cell volume, and a poli-mode, utilizing functionalized AuNPs for highly specific 3D mitochondria imaging [100].

In this work, we report the synthesis of a novel and biocompatible protein-based biopolymer for surface functionalization of AuNPs. The biopolymer is comprised of multiple groups imparting enhanced cellular uptake and mitochondria targeting. Using these AuNPs, 3D mitochondria specific poli-OCM imaging during 3000 seconds was demonstrated without any loss of contrast. Finally, we quantified mitochondrial dynamics, per voxel, using temporal autocorrelation analysis based on a classical diffusion model, which allowed us to extract mitochondria diffusion time τ_D and other diffusion parameters. The novelty of our method resulted in cells segmented into sub-volumes providing 3D parameter maps.

4.1.2 Results and Discussion

Synthesis of mitochondria specific AuNPs

We synthesized mitochondria targeting AuNP biomarkers tailor-made for poli-OCM imaging. The synthesis, functionalization, and characterization of these AuNPs are summarized in Fig. 4.1a – d. The blood plasma protein is known to be biocompatible and provides many reactive carboxylic acid and amino groups that can be further modified. First, all accessible carboxylic acid groups were converted into primary amino groups by applying ethylenediamine and the coupling reagent EDC according to a literature-known procedure [144]. After dialysis, globular polycationic bovine serum albumin (cBSA) was obtained having the ability to interact with cellular membranes, facilitate cellular uptake, and cytosolic release by Clathrin-mediated endocytosis [145]. To accomplish mitochondria targeting, lipophilic triphenyl phosphonium groups (TPP) were attached to cBSA [146]. According to the MALDI-ToF mass spectra (Fig. 4.1b), about 19 TPP groups were attached to the cBSA surface yielding cBSA-TPP in good yields. cBSA-TPP was then purified and subjected to AuNP preparation. We used a strong reducing agent, NaBH₄, to reduce Au-salt (HAuCl₄) in the presence of cBSA-TPP and yielded monodispersed spherical AuNPs with diameters centered around 3.7 ± 0.9 nm (Fig. 4.1c). The inset histogram map confirms the relative narrow size distribution and Fig. 4.1d shows the characteristic plasmonic peak of the prepared AuNPs. Since the stability of the cBSA-TPP passivated AuNPs in biological media is crucial for cellular uptake and subsequent observation of their movement without prior aggregation, dynamic light scattering experiments were performed in DMEM medium (see Fig. 4.6). No indication of severe aggregation, as little increase of the particle size, was observed, which is believed to be due to the alteration of ionic strength in biological medium as compared to its aqueous counterpart [147].

4.1. 3D time-lapse imaging and quantification of mitochondrial dynamics

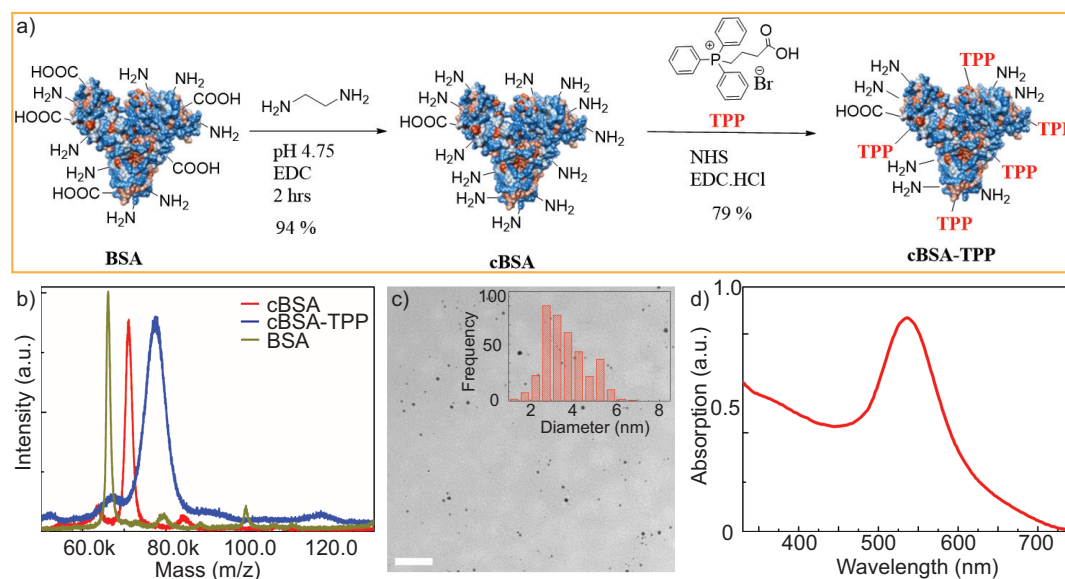


Figure 4.1 – a) Synthesis scheme of globular cationized protein (cBSA-TPP) with multiple mitochondria targeting TPP groups attached. b) MALDI-ToF spectra (matrix: sinapinic acid) indicate successful functionalization from the progressive increase in molecular weight from BSA (calculated 66.00 kDa, measured 66.13 kDa), cBSA (calculated 71.05 kDa, measured 71.04 kDa) and cBSA-TPP (calculated 77.62 kDa, measured 77.51 kDa). Approximately 19 TPP units were attached. c) Low resolution transmission electron microscopy (TEM) image of cBSA-TPP coated AuNPs. Scalebar: 50 nm. Inset: Size distribution histogram indicating average diameters of the AuNPs of 3.7 ± 0.9 nm. d) Characteristic absorption spectra of the as-synthesized AuNPs highlighting the surface plasmon peak centered at 536 nm.

In order to demonstrate the specificity of our AuNP biomarkers, HeLa cells with AuNP labeled mitochondria were co-stained with MitoTracker Red, a standard mitochondria specific dye. These AuNPs were linked with FITC fluorophores which enabled imaging via confocal laser scanning microscopy and colocalization with MitoTracker staining. We conducted this test using two different kinds of AuNP functionalization; the first group of AuNP-cBSA was attached with TPP (AuNP-cBSA-TPP) while the second one was not (AuNP-cBSA). Fig. 4.2a – f shows the fluorescence confocal images of the HeLa cells with MitoTracker (red), AuNP-FITC (green), and their overlays. From these images, we observed good colocalization of AuNP-cBSA-TPP with MitoTracker giving a Pearson's coefficient of 0.69 (Fig. 4.2d – f) as opposed to 0.29 for AuNP-cBSA (Fig. 4.2a – c). These results are indicative of the specificity of our AuNP biomarkers and substantiate their use for mitochondria specific poli-OCM imaging. In addition, we also investigated the biocompatibility of our AuNP labels through a cell viability assay (Fig. 4.2g and Fig. 4.7). We obtain 95% cell viability at 0.31 nM AuNP concentration which is the typical AuNP labeling concentration we use for poli-OCM.

Chapter 4. Quantification of mitochondrial dynamics

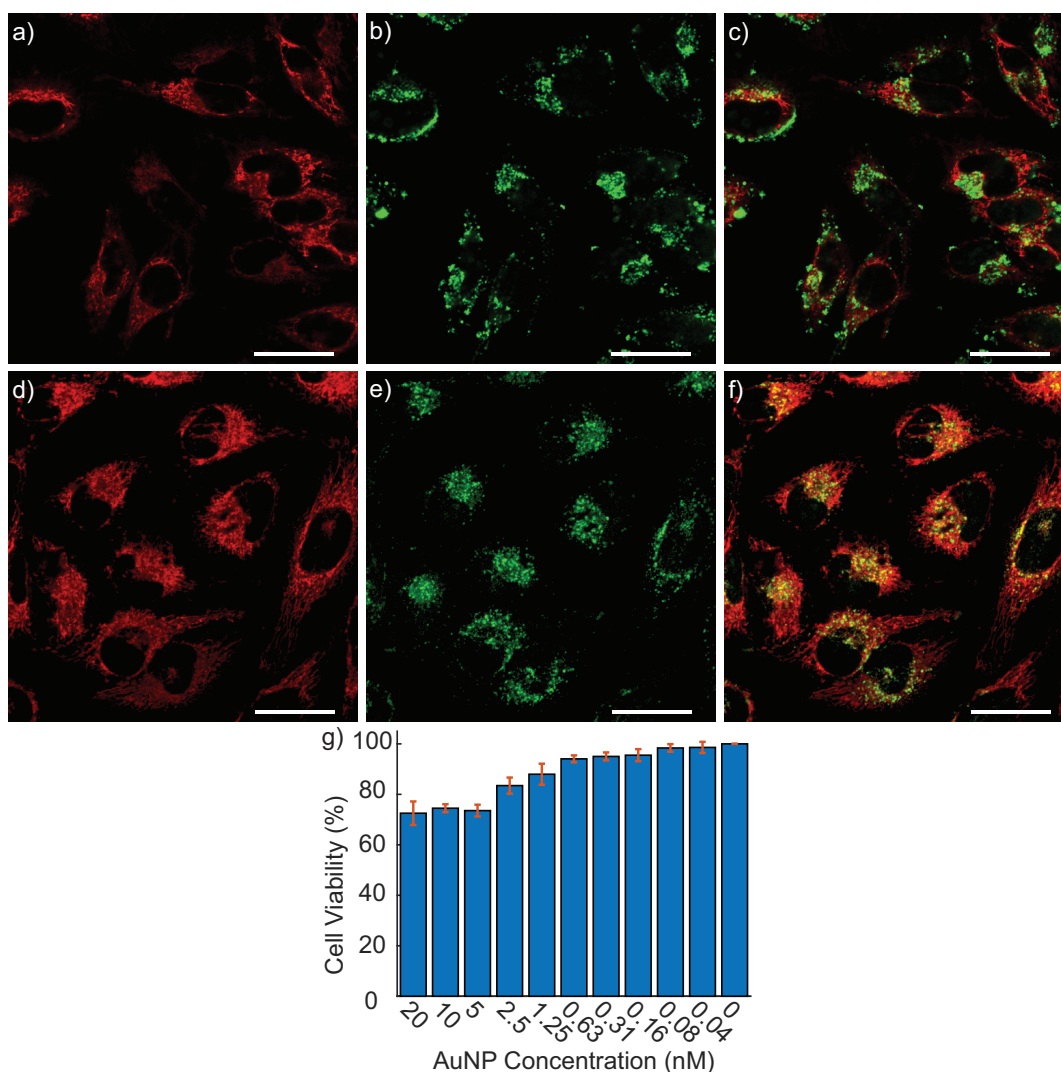


Figure 4.2 – Fluorescence confocal images of HeLa cells incubated with AuNP-noTPP a) – c) and AuNP-TPP d) – f) co-stained with MitoTracker. a) and d) are the MitoTracker images whereas b) and e) are the FITC tagged AuNPs. Their overlays in c) and f) have Pearson's coefficients of 0.29 and 0.69 for AuNP-noTPP and AuNP-TPP respectively. Scalebars: 30 μm . g) Cell viability test showing 95% viability HeLa cells incubated with 0.31 nM of mitochondria targeting AuNPs.

Quantifying mitochondrial dynamics

We quantified mitochondrial dynamics by exploiting fast and specific 3D imaging via poli-OCM and using a diffusion model considering the mitochondria as freely diffusing particles inside the voxel volume. Knowing the high complexity of the intracellular structure, we argue

4.1. 3D time-lapse imaging and quantification of mitochondrial dynamics

that using a voxel sized sampling volume allows the use of a diffusion model supposing a homogeneous environment. This model permits to assess the general mitochondrial dynamic and to cast our results in a parameter space known and used in correlation microscopy.

Our correlation analysis closely follows the principles of image correlation spectroscopy (ICS) developed by Petersen et al. [148] and Wiseman et al. [135, 149] that extended fluorescence correlation spectroscopy (FCS) to full 2D imaging methods. ICS based correlation analysis on pixel-wise intensity fluctuations provide the diffusion time of the particles under investigation. Merging photothermal detection and correlation spectroscopy was previously introduced [150, 151] but not with 3D imaging or extended time scales (up to 1 hour) [152] In a similar manner, phase correlation imaging has also been demonstrated as a robust technique for studying cell dynamics [153] even without the use of specific labels. As we have previously stated, using the poli-OCM we achieved fast 3D mitochondria specific live cell imaging up to 3000 seconds without any loss of contrast (see Fig. 4.10).

Stepping from 2D to 3D imaging, the voxel-wise autocorrelation function can be stated as

$$G_V(\tau) = \frac{\langle \delta i_V(t) \delta i_V(t+\tau) \rangle}{\langle i_V(t) \rangle \langle i_V(t+\tau) \rangle} \quad (4.1)$$

where the indices V point to the individual voxels i.e. the sampling volumes, $\langle \rangle$ denotes time averaging, $i_V(t)$ the time-dependent intensity and τ the temporal lag. The temporal intensity fluctuation is then defined as $\delta i_V(t) = i_V(t) - \langle i_V(t+\tau) \rangle$. Assuming a 3D Gaussian sampling volume, (see Fig. 4.9), the processed intensity data are fitted with the model for classical 3D diffusion behavior

$$G_V(\tau) = \frac{G(0)}{\left(1 + \frac{\tau}{\tau_D}\right) \sqrt{1 + \frac{\tau}{\kappa \tau_D}}} + G_\infty. \quad (4.2)$$

Here $\kappa = \left(\frac{z_0}{r_0}\right)^2$ where r_0 and z_0 represent the lateral and axial extent of the sampling volume, τ_D is the diffusion time, and $G_\infty = \lim_{\tau \rightarrow \infty} G_V(\tau)$ [135, 154]. In FCS, $G(0) \propto \frac{1}{N}$, where N is the mean number of diffusing particles. $G(0)$, in turn, is dependent on the signal to noise ratio and also considers “independent particles” [155], which in the case of poli-OCM can be influenced by AuNP labelling efficiency and interparticle coupling [156]; an in depth analysis of this dependence is beyond the scope of this study. All instrument parameters, r_0 and z_0 , were evaluated by measuring the point spread function (PSF), fitting it with a Gaussian profile, (Fig. 4.9) and by taking into account the coherence length which defines the axial extent of

Chapter 4. Quantification of mitochondrial dynamics

the PSF [157, 158]. For a more in depth discussion of coherent correlation analysis please refer to previous papers in OCCS [157, 158]. Due to the interferometric detection, our signal has extremely high sensitivity to phase and not only intensity in contrast to ICS of Wiseman and Petersen.

The dual imaging modality of the poli-OCM is exhibited in Fig. 4.3a – c. where we show en face and orthogonal slices of the 3D dfOCM (Fig. 4.3a), photothermal OCM (Fig. 4.3b) tomograms, and their overlay (Fig. 4.3c). The orthogonal slices emphasize the 3D specific imaging and localization we achieve using the poli-OCM; we are capable of imaging the entire cell morphology (Fig. 4.3a) as well as only the AuNP labeled mitochondria (Fig. 4.3b). For the purposes of our temporal autocorrelation analysis we image individual cells in a scan range of $25\mu\text{m} \times 25\mu\text{m}$. Alternating between dfOCM and poli-mode, tomograms similar to (Fig. 4.3a and b) were acquired to monitor both the motion of the entire cell (dfOCM) and mitochondrial dynamics (photothermal OCM).

The temporal autocorrelation was calculated for each voxel in the 3D poli-OCM tomogram time series following equation (1). The data was then segmented into sub-volumes of $2 \times 2 \times 2$ voxel ($0.58\mu\text{m} \times 0.58\mu\text{m} \times 2.05\mu\text{m}$) where the autocorrelation was averaged and subsequently fitted with the diffusion model given by equation (2) using a non-linear least squares solver. Our method allowed the extraction of diffusion parameters from each of these segmented sub-volumes resulting in a 3D diffusion time map (Fig. 4.3f). Furthermore, the $2 \times 2 \times 2$ voxels sub-volume we use are related to the measured dimensions of our point spread function (PSF).

The data shown in Fig. 4.3d represent five sub-volumes with different diffusion times (see matched color code of histogram in Fig. 3e) underlining the high variation of the mitochondrial dynamics across the full cell volume. The very small residuals between the autocorrelation and the model indicate a good fit and give confidence to the validity of the model. Additionally, the normalized autocorrelations (Fig. 4.3d, inset) demonstrate even more the large variation of τ_D . The probability distribution (*pdf*) of the τ_D extracted from all sub-volumes in the entire cell (Fig. 4.3e) demonstrates a spread of over two orders of magnitude with a τ_D ranging from 10 to 1.5×10^3 seconds having a mean value of 214 sec. (median value of 101 sec.). We divided the *pdf*(τ_D) into five color-coded intervals, each representing 20 % of the total cell volume (Fig. 4.3e). These intervals were used to render a 3D map of the diffusion time, as shown in Fig. 4.3f and Fig. 4.12 with each sub-volume color-coded according to the *pdf*(τ_D). This 3D map allows us to determine and locate regions within the cell featuring high or low mitochondrial dynamics. These extracted τ_D can be further related, by the Stokes-Einstein relation (see Fig. 4.12), to the viscosity values inside our sampling volumes. Assuming a mitochondria hydrodynamic radius of 500 nm we deduced viscosity values ranging from 0.18 to 26.7 (Pa·s), which are still within the range predicted by the model of Kalwarczyk et al. [159]. In addition, the associated diffusion constants we calculate from these data coincide with published

4.1. 3D time-lapse imaging and quantification of mitochondrial dynamics

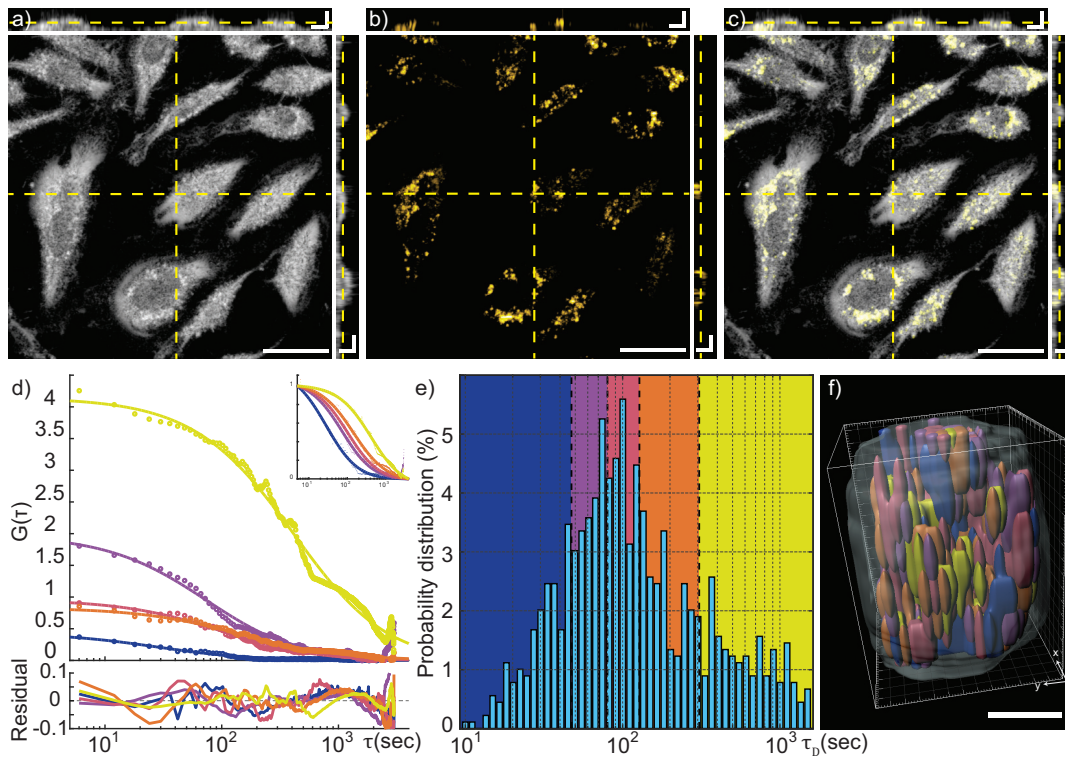


Figure 4.3 – En face and orthogonal slices of a) 3D dark-field OCM and b) poli-OCM tomograms and c) their overlay. In d) we show selected autocorrelation data with corresponding fits and their residuals. Inset: normalized autocorrelation and fits. e) Probability distribution of all extracted diffusion times from each sub-volumes in the entire cell is shown. The color-coded segments of e) each represents approximately 20% of the complete cell volume. f) 3D rendering (diffusion time map) using data from e) illustrating the high heterogeneity of mitochondrial dynamics within the cell. The semi-transparent grey volume outlines the entire cell volume. d)-f) shares the same color-code meaning each curve in d) comes from the same colored segment in e) as well as the same colored sub-volume in f) Scalebars: a) - c) $30 \mu\text{m}$ en face and $7.5 \mu\text{m}$ orthogonal slices, f) $5 \mu\text{m}$.

quantified cellular dynamics using phase correlation imaging [153].

In addition to the high heterogeneity of mitochondrial dynamics, regions within the cell, where it was not possible to extract any diffusion parameters were also observed. As elaborated in S.6. of the supporting information, this region exhibits a high overlap with the locations in the corresponding dfOCM (dark-field OCM) time series showing lower scattering signal. We associate this low scattering regions to the nucleus of the cell where no mitochondria are expected.

Chapter 4. Quantification of mitochondrial dynamics

The high heterogeneity of diffusion parameters over the cell volume is an observed phenomenon resulting from our data and analysis. This is not surprising given the known complexity of the intracellular environment [160–162], especially considering the size of mitochondria and their tendency to form networks. Furthermore, the works of Planchon et al. [140] and Chen, B.-C. et al. [141] also observed this variety in mitochondrial dynamics using a completely different and independent imaging concept. We would like to reiterate that, unlike fluorescence, poli-OCM imaging is not prone to photobleaching at all; as shown in Figures 4.10, there is no decrease in signal contrast even after acquiring 500 poli-OCM tomograms. We, nevertheless, consider lattice light-sheet microscopy as the golden standard for imaging live intracellular dynamics and poli-OCM imaging compares well with these published time-lapse acquisition protocols. These previous works in light sheet microscopy [140, 141] demonstrated similar high heterogeneity of mitochondrial dynamics and can therefore be considered as an independent validation of our observations.

4.1.3 Conclusion

In this paper, we report highly specific fast 3D imaging of mitochondrial dynamics inside living HeLa cells. We prepared narrowly dispersed AuNPs with a protein coating based on the plasma protein BSA, functionalized with positive ammonium and multiple TPP groups. The positive ammonium groups improve cell membrane attachment and endocytosis while the TPP groups provide intracellular mitochondria targeting. All AuNPs used in this study were decorated by the functionalized protein coating approach. The photostability and limited toxicity of these markers enabled true long-lasting time lapse live cell imaging. Finally, we used these functionalized AuNPs for fast 3D poli-OCM imaging to quantify mitochondrial dynamics via temporal autocorrelation analysis resulting to 3D diffusion parameters maps. We believe that this method provides a novel perspective of mitochondrial dynamics and paves an innovative way for investigating its relation to various not yet understood metabolic diseases.

4.1.4 Methods

Preparation of functionalized protein coated AuNPs

Materials used Cationized bovine serum albumin (cBSA) was synthesized following the procedure reported previously by our group [120] N-hydroxy-succinimide (NHS, 99%), (3-Carboxypropyl) triphenylphosphonium bromide (TPP), 98% and N-(3-Dimethylaminopropyl)-N'-ethylcarbodiimide hydrochloride (EDC, 98%) were procured from Sigma-Aldrich. Hydrogen tetrachloro aurate (III) trihydrate, ACS, 99.99% was obtained from Alfa Aesar. Sodium borohydride 98% was bought from Acros Organics. All chemicals were used as received without further purification. Vivaspin ultrafiltration tubes were purchased from GE healthcare. Ultra-pure

4.1. 3D time-lapse imaging and quantification of mitochondrial dynamics

milli-Q water was used for all experiments involving water.

Synthesis of cBSA-TPP TPP (80 mg), NHS (30 mg) and EDC.HCl (40 mg) were dissolved in 0.5 mL of degassed dimethylformamide (DMF) solution. This mixture was stirred at room temperature under argon atmosphere for overnight. Next day, cBSA (20 mg) dissolved in 20 mL milli-Q water was added and reacted overnight at room temperature. The product was washed through vivaspin 20 (MWCO 30K) ultracentrifuge tube to separate the unreacted reactants. Finally, the solution was kept at 4°C for future use. Fig 4.5 shows the zeta potential and XPS data of the conjugate.

Synthesis of cBSA-TPP coated AuNPs AuNPs with desired sizes were synthesized and functionalized for mitochondria labeling. Briefly, aqueous HAuCl₄ solution (60 μL, 10mM) and cBSA-TPP (globular cationic bovine serum albumin with triphenyl phosphonium cations, 50 μL, 10 mg/mL) were mixed and the solution was diluted to 250 μL with milli-Q water. Freshly prepared NaBH₄ solution (6 μL, 3 mg/mL) in chilled milli-Q water was added rapidly to the solution which yielded monodispersed, spherical AuNPs with diameter of approximately 4 nm. Then, the reaction mixture was stirred for 30 minutes and washed with water to remove excess of NaBH₄. By varying the amount of added NaBH₄, various sizes of the AuNPs were obtained. In particular, the AuNPs used in the poli-OCM imaging experiments had diameters of 3.7 ± 0.9 nm. Corresponding XPS peaks of AuNPs are presented in Fig. 4.6a.

AuNP characterization Plasmonic absorption was recorded using TECAN infinite M1000 microplate reader. Zeta-potential and DLS measurements were performed using a Malvern Zetasizer ZEN3600 (Malvern Ltd, Malvern, UK) at 20°C. A JEOL 1400 transmission electron microscope was used to obtain bright field TEM images of the AuNPs. X-ray photoelectron spectroscopy (XPS) data were recorded on a Physical Electronics PHI 5800 ESCA System using mono-chromatized Al K α radiation (13 kV, 250 W).

Cell viability assay

HeLa cells were cultured in Dulbecco's Modified Eagle Medium (DMEM, Gibco) with 10% fetal bovine serum, 1% penicillin/streptomycin with phenol-red and seeded at 6,500 cells/well in a white 96-well (half-area) plate. The cells were left to adhere overnight at 37°C and 5% CO₂ and afterwards different concentrations of AuNPs were added into each well. The treated cells were subsequently incubated with the AuNPs for approximately 30 hours at 37°C, 5% CO₂. After incubation, the cells were washed with phosphate buffer to remove the excess AuNPs present in the medium and re-incubated with DMEM medium. The cells were further incubated for

Chapter 4. Quantification of mitochondrial dynamics

4 hours before the addition of Tox-8 reagent with phenol red free DMEM medium. After 2 hours incubation with Tox-8, the emission intensity was measured by a Tecan Infinite M1000 microplate reader ($\lambda_{ex} = 570$ nm, $\lambda_{em} = 590$ nm). We used wells without cells but with Tox-8 reagent as controls. Each experiment was performed in quadruplicates. The cell viability (V) was calculated according to the following equation

$$V = \left(\frac{X - Z}{Y - X} \right) \times 100\% \quad (4.3)$$

where X is the average emission with the treatment of AuNPs at various concentrations, Y is the average emission of the experimental groups without the treatment of the AuNPs, and Z is the average emission of the culture medium background.

Confocal microscopy

HeLa cells were incubated in Dulbecco's Modified Eagle Medium (DMEM, Gibco) with 10% fetal calf serum (FCS, Gibco) and non-essential amino acids in a humidified incubator at 37°C and 5% CO₂. For confocal laser scanning microscopy (CLSM), cells were seeded onto an Ibidi μ -slide 8-well and incubated with FITC labelled protein coated AuNPs for 24 hours. We used two different kinds of protein coating: one with TPP attached and the other without TPP attached in its backbone. Fluorescence confocal laser scanning microscopy (CLSM) images were acquired with a 63 \times 1.4 NA oil immersion plan apochromatic LSM 710, Axio Observer objective. Fluorescence of FITC was excited by a HeNe laser $\lambda_{ex} = 488$ nm (AOTF transmission set to 10-20%) and was set to emission maximum at 525 nm. We added 1 μ M MitoTracker Red in each well-plate and excited at 560 nm with an emission maximum at 625 nm.

poli-OCM imaging

The 3D time-lapse imaging and analysis we implemented for the quantitative assessment of mitochondrial dynamics is summarized schematically in Fig. 4.4.

Cell culture and AuNP labelling HeLa cells were seeded and incubated overnight onto an Ibidi μ -slide 8-well with 250 μ L of cell culture medium (Dulbecco's Modified Eagle Medium (DMEM, Gibco), 10% fetal bovine serum, and 1% penicillin and streptomycin antibiotics). 2 μ L of 40 nM AuNP solution were then added into the media and again incubated overnight. Finally, the cells were washed with PBS and fresh culture medium was added before imaging. During poli-OCM imaging, the Ibidi μ -slide 8-well was housed in a custom built micro-incubator, where the temperature was regulated at 37°C and humidified premixed (5% CO₂) air was pumped continuously.

4.1. 3D time-lapse imaging and quantification of mitochondrial dynamics

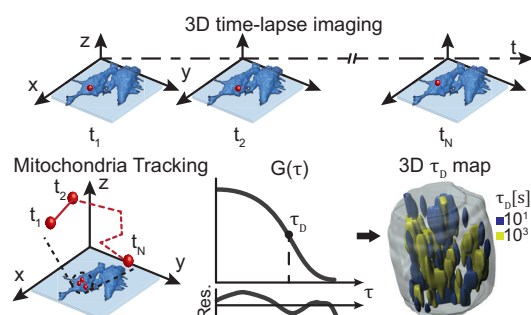


Figure 4.4 – Schematic summarizing step by step imaging and data extraction for mitochondrial dynamics. 3D time lapse imaging of live HeLa cells was performed using the poli-OCM localizing the AuNP labeled mitochondria. Temporal autocorrelation analysis was applied over the whole cell volume resulting in a 3D map of mitochondria diffusion time. In addition, imaging with the poli-OCM also enables mitochondrial dynamics quantification via tracking individual AuNP-labeled mitochondria but is outside the scope of this work

poli-OCM instrumentation The specifics of the OCM instrument as shown in Fig. 4.8 have been previously described and characterized elsewhere (xfOCM [27], dfOCM [163] and poli-OCM [100]). A broadband laser source centered at 800 nm ($\Delta\lambda = 135$ nm) is used as a source for optical coherence imaging. An axicon shapes the illumination beam into a Bessel beam which propagates across the scanning unit and is focused on the sample by a high-NA objective (25 \times , NA = 0.8, Carl Zeiss). The backscattered field is collected by the same objective and superimposed with the reference beam; the resulting interference is finally recorded using a custom-made spectrometer. The Bessel beam configuration of our poli-OCM ensures an extended depth of field or a uniform lateral resolution over the full 3D cellular volume. The poli-OCM, as used in this study, provides a lateral and axial resolution of 0.53 μm and 2.15 μm respectively over an extended depth of focus of 50 μm . The experimental measurement of the resolution is discussed in the supporting information. The photothermal contrast of the poli-OCM [100] is achieved by exciting the plasmonic resonance of the AuNPs using a 532 nm solid-state laser. This photothermal heating beam is intensity modulated at 150 kHz using an AOM before being coupled into the OCM scanning unit by a dichroic mirror (D1; 720DCXR, Chroma Technology). This intensity modulation induces a similarly modulated index of refraction around the AuNP which in turn generates a modulated backscattered signal. This backscattered field is superimposed with a phase modulated reference field (150 kHz) enabling heterodyne detection of the sinusoidally modulated signal. In accordance with C. Pache et al. we operate at an A-scan rate of 3900Hz with an integration time of 250 μs [100]. At this operating parameters the temperature increase in the vicinity of an individual AuNP is approximately 1K [98, 100]. During imaging, we used approximately 6 mW for OCM probe beam and 3 mW average power for the photothermal heating laser.

Chapter 4. Quantification of mitochondrial dynamics

Time lapse imaging Aiming for the extraction of diffusion parameters of the AuNP labeled mitochondria requires fast 3D imaging with short time intervals while extending the experiment over a prolonged acquisition period (100 to 10^3 seconds). A total of 1000 3D tomograms were acquired over a volume of $25 \times 25 \times 50 \mu\text{m}^3$ (approximately $0.29 \times 0.29 \times 1.028 \mu\text{m}^3$ per voxel) while alternating between dfOCM and poli-OCM. This resulted in two time series each having 500 3D tomograms and a time interval of 6 seconds between tomograms. This scan protocol provided us with sufficient sampling necessary for our autocorrelation analysis. Similarly, poli-OCM imaging allows for 3D tracking of AuNP labeled mitochondria but this is not within the scope of this current work.

4.1.5 Supporting Information

S1. Functionalized protein coated AuNP preparation

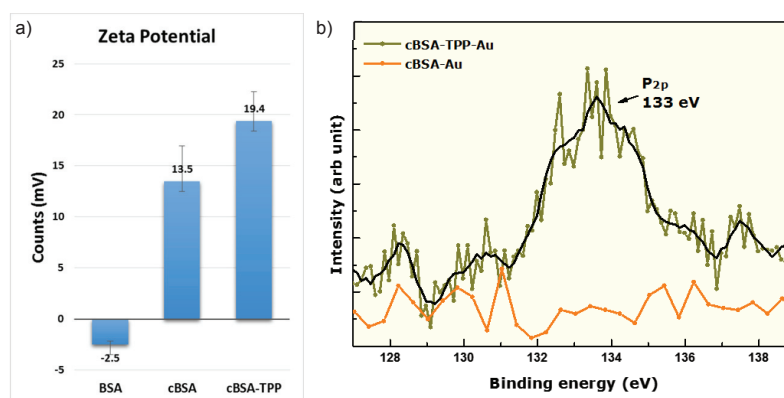


Figure 4.5 – a) Zeta-potential values of BSA, cBSA, and cBSA -TPP conjugates. Increase in zeta-potentials proceeds in line with the expected increase in the number of positive charges after each reaction step. b) XPS spectra of the protein backbone before and after TPP conjugation, where the respective peaks of P_{2p} is clearly observed.

S2. Cell viability test

In addition to the cell viability test included in the main text, we investigated the viability of HeLa cells with AuNP labeled mitochondria exposed to 532nm illumination. A second 96-well plate was prepared following the same procedure as in the experimental section and incubated with the same concentration of AuNPs. This plate was illuminated with light from a 532nm LED array with approximately 5mW of power for 5 minutes continuously. Exposure to the 532nm light was done after washing the excess AuNPs from cell culture. As seen in Fig. 4.7 we still achieved good cell viability at 87% even with this light exposure. The photothermal contrast of our poli-OCM is achieved by scanning a focused intensity modulated 532nm

4.1. 3D time-lapse imaging and quantification of mitochondrial dynamics

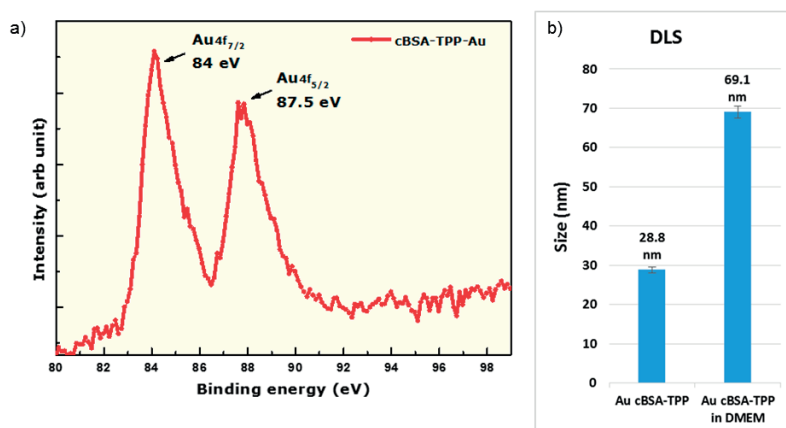


Figure 4.6 – a) XPS spectra of cBSA-TPP passivated Au NPs, where the respective peaks of Au_{4f_{7/2}} and Au_{4f_{5/2}} are readily seen. b) Dynamic Light Scattering (DLS) data of as-synthesized AuNPs in water and DMEM medium. No indication of aggregation is observed.

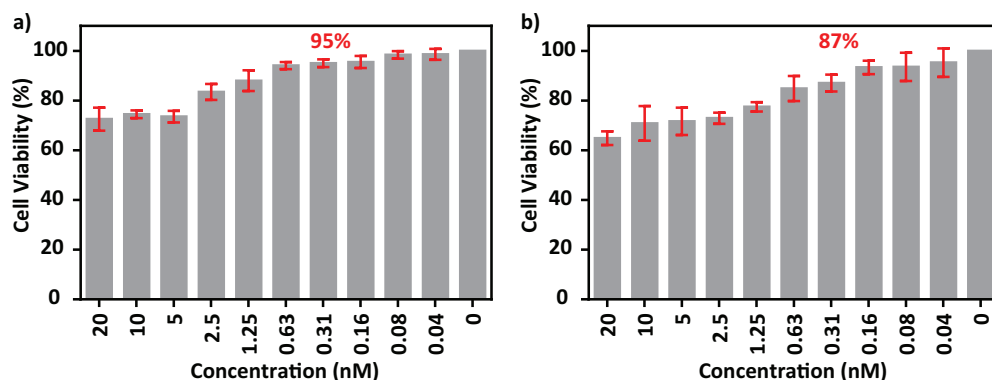


Figure 4.7 – Cell viability data of cBSA-TPP coated AuNPs with (a) 30hrs incubation with no light irradiation, (b) 30hrs total incubation and after 24hrs 532nm LED light irradiation at ≈ 5 mW power with continuous illumination for 5 min. For obtaining poli-OCM image in this work, we used 0.31nM AuNP which clearly stayed in the window where most of the cells were alive (95% and 87% respectively).

beam with an average power of 2mW. Using an integration time of 250 μ s for each A-Scan location (1 pixel along the lateral scan) this translate to 0.5 μ J of light energy distributed over the extended focal depth. Please be aware that for OCM we only need to do 2D scan to achieve 3D tomograms because a single A-Scan records the full axial profile. The induced light stress is therefore negligible compared to fluorescence confocal microscopy. Even with 5mW exposure for 5 minutes (1.5J equivalent to 3×10^6 times more energy) we still achieve 87% cell viability; however, this is through wide-field illumination over the whole cell culture and is not directly comparable to our imaging conditions.

Chapter 4. Quantification of mitochondrial dynamics

S3. poli-OCM schematic and system parameters

A confocal fluorescence channel was also added to the poli-OCM using a dichroic mirror (D2; TL600, Chroma Technology). A 632nm HeNe laser is used as an excitation source spectrally separated from the fluorescence detection path by a dichroic mirror (D3; z647rdc, Chroma technology). This fluorescence signal is filtered by a bandpass filter (HQ680/35, Chroma technology) and detected by an avalanche photodiode (SPCM-AQR-14-FC, PerkinElmer). The addition of the confocal channel enables simultaneous dfOCM and fluorescence imaging.

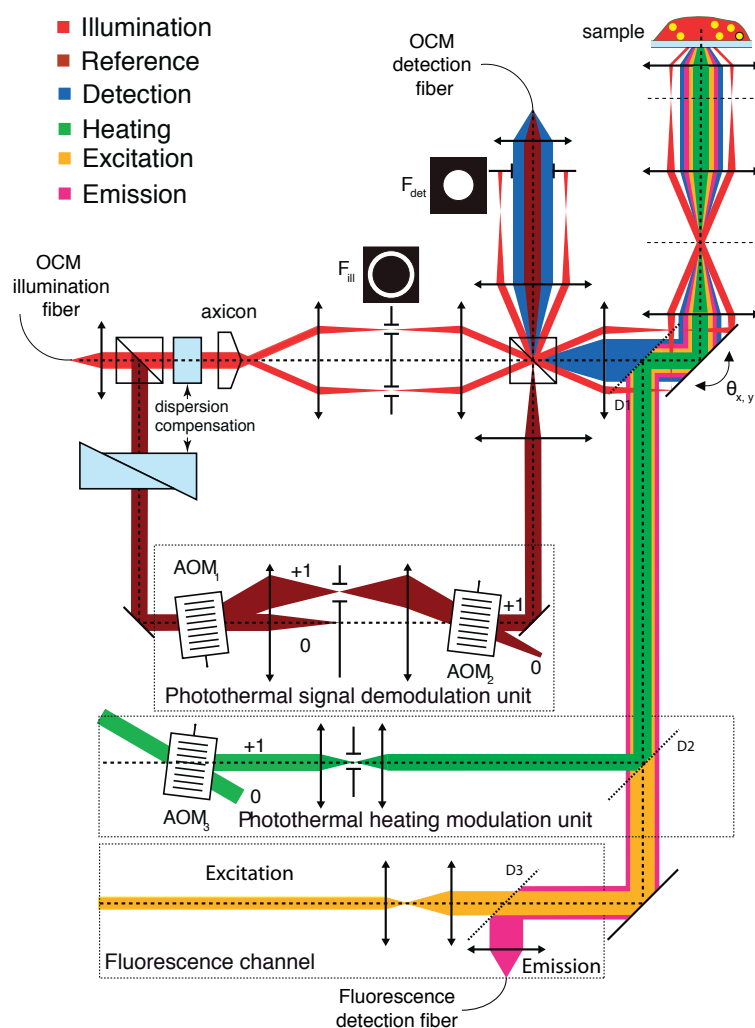


Figure 4.8 – Photothermal optical lock-in optical coherence microscopy setup with an added fluorescence channel.

4.1. 3D time-lapse imaging and quantification of mitochondrial dynamics

	OCM probe	Photothermal heating	Fluorescence excitation
Wavelength	800nm ($\Delta\lambda = 135\text{nm}$)	532nm	632nm
Power	6mW	3mW	80 μW

Table 4.1 – Summary of poli-OCM light source parameters

Imaging parameters The details of poli-OCM light sources are summarized in Table 4.1 and the effective imaging NA is 0.68. 3D time lapse tomograms were acquired by scanning 86×86 pixels covering $25 \times 25 \mu\text{m}^2$ along the x-y plane. The spectrometer of the poli-OCM has an imaging axial extent of $700 \mu\text{m}$ in air ($\approx 526 \mu\text{m}$ in water with 1.33 index of refraction) over 512 pixels. For all our OCM imaging we maintain a voxel sampling of approximately $0.29 \mu\text{m}/\text{voxel}$ laterally $1.028 \mu\text{m}/\text{voxel}$ axially.

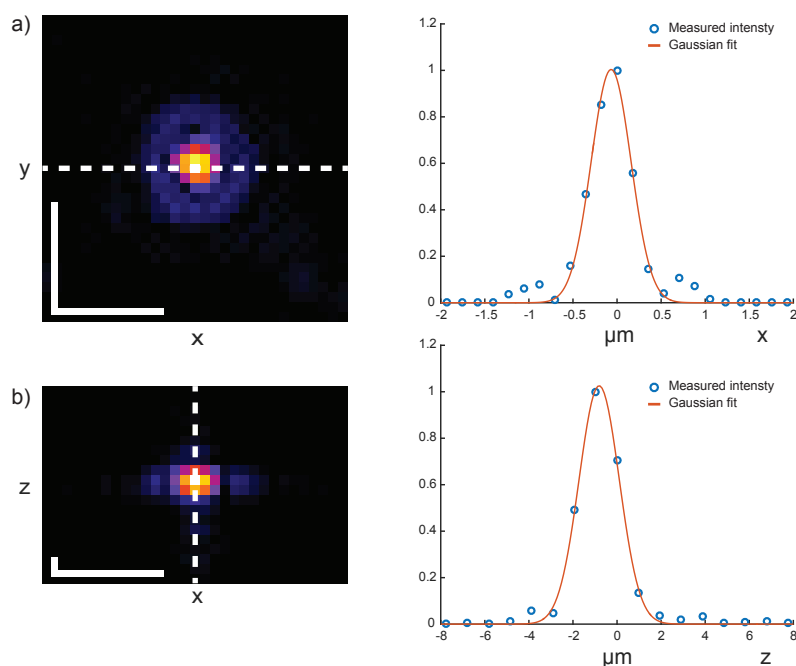


Figure 4.9 – a) En face and b) orthogonal slice of a poli-OCM image of a 50nm AuNP in PDMS and their normalized profile taken along the dashed line with a corresponding Gaussian fit. Scalebar: $2 \mu\text{m}$.

PSF measurement We measure the point spread function (PSF) of the poli-OCM experimentally by imaging 50nm AuNPs suspended in PDMS ($n = 1.4$) as shown in Fig. 4.9. We extract the linear profiles laterally and axially along the dashed lines in Fig 4.9 and fit a Gaussian following

Chapter 4. Quantification of mitochondrial dynamics

$$PSF(s) = A \exp\left(-\frac{(s-\mu)^2}{2\sigma^2}\right) \quad (4.4)$$

where s represents the spatial dimension (x , y or z). Table S1 lists the parameters of the fitted Gaussian laterally (x,y) and axially (z). From this fit we derive the lateral and axial extent, r_0 and z_0 , used in our classical diffusion model which corresponds to the e^{-2} radius of the PSF along both dimensions.

	Lateral	Axial
A	1.004	1.026
μ	-0.067	-0.811 μm
σ	0.226	0.913 μm
FWHM	0.532	2.150 μm
$r_{e^{-2}}$	0.452	1.826 μm

Table 4.2 – Gaussian fit parameters of the poli-OCM PSF

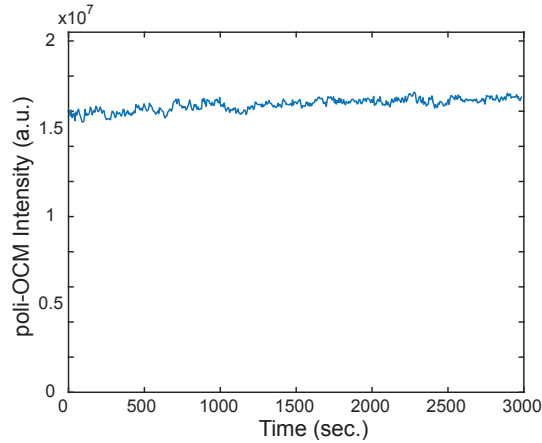


Figure 4.10 – Integrated poli-OCM signal in the whole imaging volume over the imaging period. 500 3D poli-OCM tomograms were acquired continuously at a rate of 1/6Hz.

Contrast stability of live cell poli-OCM imaging We demonstrate the stability of the photothermal contrast of our poli-OCM by monitoring the total signal intensity for each of the 3D tomograms over the entire time series. Unlike most fluorescent dyes, we expect stable poli-OCM signal even with prolonged continuous imaging. Fig. 4.10 shows the behavior of the poli-OCM signal over a span of 3000 seconds, which clearly shows no decrease in signal intensity.

S.4. Image processing & analysis algorithm

The poli-OCM, as we have briefly described in S.3. of the supporting information, is a Spectral Domain OCM system. Its underlying interferometric principle enables 3D volumetric imaging with only x-y scanning. [27, 34, 93, 163] Fig. 4.11 summarizes the algorithm we used to generate 3D tomograms. We subtracted a measured background spectrum from the interference spectrum acquired at every position on the x-y plane. We then applied “*k*-mapping” which converts our spectra that is linear with wavelength λ to spectra linear in wavenumber *k*. We then obtain the 3D tomogram after a Fast Fourier Transform of these spectra. This procedure is repeated for all acquisition in the time series resulting in a 3D time-lapse data set.

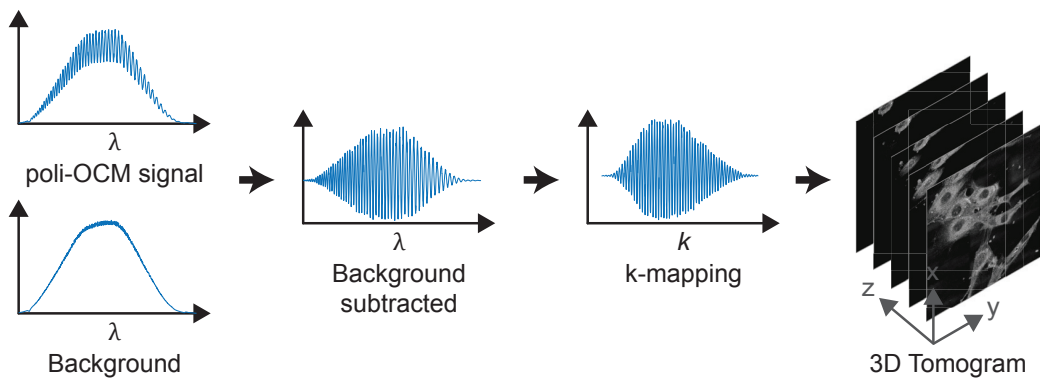


Figure 4.11 – Schematic of 3D tomogram calculation.

We then calculate the temporal autocorrelation of our poli-OCM signal following like in Eq. 2.1 and Eq. 4.1. [150, 151, 157]

$$G_V(\tau) = \frac{\langle \delta i_V(t) \delta i_V(t+\tau) \rangle}{\langle i_V(t) \rangle \langle i_V(t+\tau) \rangle} = (T-\tau) \frac{\sum_{t=0}^{T-\tau} \delta i_V(t) \delta i_V(t+\tau)}{\sum_{t=0}^{T-\tau} i_V(t) \sum_{t=0}^T i_V(t)}. \quad (4.5)$$

We then average the autocorrelation over a volume of $2 \times 2 \times 2$ voxels ($0.58 \mu\text{m} \times 0.58 \mu\text{m} \times 2.05 \mu\text{m}$) then fit the diffusion model using non-linear least squares solver; specifically we use the `lsqcurvefit` function of Matlab R2015b. Averaging over this sub-volume decreases the number of voxels our diffusion parameter maps (i.e. an initial $40 \times 40 \times 20$ voxel space will be reduced to $20 \times 20 \times 10$). To reduce computation time, we generate a mask using the dfOCM image of the cell to exclude voxels outside the cell volume.

For the last part of our analysis, we only consider sub-volumes with autocorrelations fitted with an $R^2 \geq 0.85$. In addition, we also excluded sub-volumes having autocorrelations similar to sub-volumes outside the cell. Diffusion parameters were extracted only from the remaining

Chapter 4. Quantification of mitochondrial dynamics

sub-volumes. Regions inside the cell that were excluded correspond to areas without AuNP labeled mitochondria.

S.5. Diffusion parameter maps

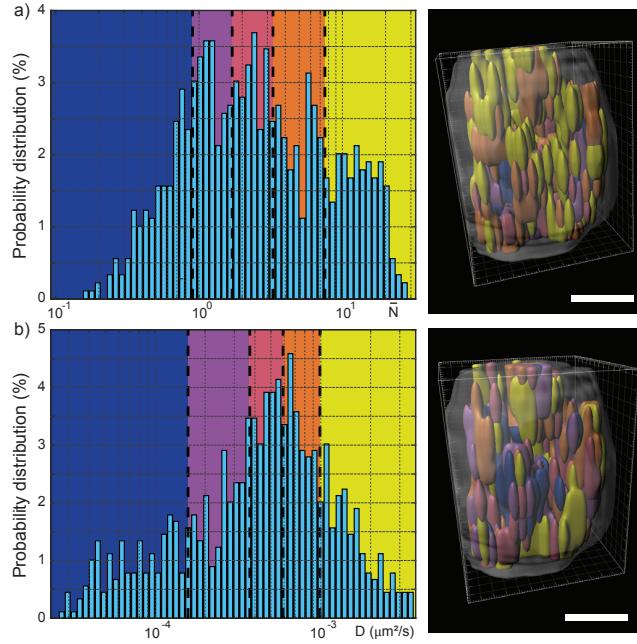


Figure 4.12 – Probability distribution and rendered 3D map of a) mean number of AuNP labeled mitochondria and b) diffusion constant per sub-volume. Scalebar: $5\mu\text{m}$

In addition to quantifying mitochondrial dynamics with the diffusion time, we extract the diffusion constant D and $1/G(0)$. Similar to Fig 4.3, we show the probability distribution and a rendered 3D map of these physical parameters in Fig. 4.12. We calculate the diffusion constant D following

$$D = \frac{r_0^2}{4\tau_D} \quad (4.6)$$

where τ_D is the extracted diffusion time and r_0 is the same as in Table 4.2. We divide both $pdf(D)$ and $pdf(1/G(0))$ into 5 color-coded segments each corresponding to 20% of the cell volume and use these to generate the 3D maps.

The diffusion coefficient can be further related to viscosity by the Stokes-Einstein relation

4.1. 3D time-lapse imaging and quantification of mitochondrial dynamics

given by

$$D = \frac{k_B T}{6\pi\eta r_h} \quad (4.7)$$

k_B is the Boltzmann constant, T the temperature, η is the viscosity, and r_h is the hydrodynamic radius of the diffusing particle.

S.6. Details on diffusion time map

We separate the diffusion time map in 4.3f and Fig. 4.13a into the 5 intervals (Fig. 4.13b-f) of the probability distribution in Fig 4.3e. Furthermore, we include a 6th region, shown in white (Fig 4.13 a-f), which represents the volume within the cell where we extract no diffusion parameters. In this volume, we do not measure any poli-OCM signal and consider it as a region of “infinite” diffusion time. In addition, we observe that this volume has a good correlation with the location in the dfOCM images with lower scattering signal (darker or lower contrast). We expect the nucleus of the cell to be located within this volume.

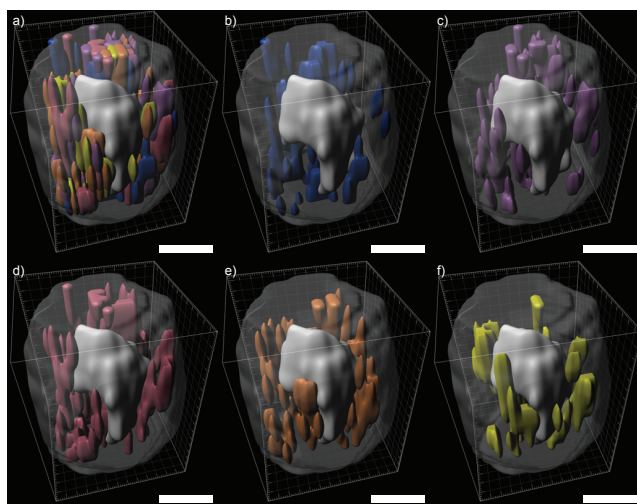


Figure 4.13 – 3D rendering of AuNP labeled mitochondria diffusion time for each of the different cell segments (see main text Fig. 4.3) including a volume with infinite diffusion time supposedly corresponding to the nucleus. Scalebar: $5\mu\text{m}$

4.2 poli-OCM autocorrelation analysis for finite sized particles

In the preceding section, we quantified mitochondrial dynamics using a temporal autocorrelation analysis that is widely used in conventional FCS experiments. This analysis is based on the free diffusion model, which assumes pointlike diffusers. Unfortunately, this assumption only holds true for particles that are much smaller than the observation volume [164–167]. Mitochondria are large organelles known to have diameters of 500nm or bigger while the poli-OCM has a measured PSF with lateral beam waist $\omega_0 \approx 0.42\mu\text{m}$ (4.1.5). For the case of FCS, a number of publications have already investigated the effect of finite sized diffusers to the extracted diffusion parameters. It has been consistently confirmed that maintaining the assumption of pointlike diffusers leads to overestimated values of τ_D [164, 165]. A common approach for correcting the effects of large diffusers is to modify the molecular detection function (MDF).

The MDF is a more complete description of an FCS experiment, which defines the spatial probability distribution of detecting fluorescence signal within the observation volume. Considering spherically symmetric diffusing particles with a finite extent, Mueller et al. [164] proposed modifying the MDF, $U(\mathbf{r})$, as

$$\bar{U}(\mathbf{r}) = \int d\mathbf{r}' v(|\mathbf{r} - \mathbf{r}'|) U(\mathbf{r}') \quad (4.8)$$

where $v(\mathbf{r})$ describes the particle over the three-dimensional space \mathbf{r} . Assuming rotational symmetry of the MDF and orienting the optical axis along the z direction, Equation 4.8 can be rewritten in cylindrical coordinates (ρ, z) as

$$\bar{U}(\rho, z) = \int_0^\infty dk_z \int_0^\infty dk_\rho k_\rho \tilde{v}(k_\rho, k_z) \tilde{U}(k_\rho, k_z) J_0(k_\rho \rho) \exp[-ik_z z]. \quad (4.9)$$

J_0 is the zero order Bessel function of the first kind and $\tilde{v}(k_\rho, k_z)$ and $\tilde{U}(k_\rho, k_z)$ correspond to the coefficients of Fourier-Bessel expansions of $v(\mathbf{r})$ and $U(\mathbf{r}')$ respectively. We determine the effect of mitochondria size by modifying the effective MDF as in Eq. 4.9.

In the previous section, we used a model that approximated the MDF, $U(\mathbf{r})$, of the poli-OCM as a Gaussian in three-dimensions

$$U(\rho, z) \propto \exp\left[-2\left(\frac{\rho^2}{\omega_0^2} + \frac{z^2}{z_0^2}\right)\right], \quad (4.10)$$

4.2. poli-OCM autocorrelation analysis for finite sized particles

with parameters $\omega_0 = 0.452\mu\text{m}$ and $z_0 = 1.83\mu\text{m}$ determined by measuring the PSF (4.1.5). We modeled the mitochondria as spherical particles with radius a and considered three different cases of AuNP labeling distributions defined by $\nu(\mathbf{r})$,

$$\nu_0(\mathbf{r}) = \delta(\mathbf{r}) \quad \text{all AuNPs in a single **point** (center),} \quad (4.11a)$$

$$\nu_1(\mathbf{r}) = \begin{cases} 1 & \mathbf{r} \leq a \\ 0 & \text{otherwise} \end{cases} \quad \text{uniform labeling over the whole **sphere**, and} \quad (4.11b)$$

$$\nu_2(\mathbf{r}) = \begin{cases} 1 & a_1 < \mathbf{r} \leq a_2 \\ 0 & \text{otherwise} \end{cases} \quad \text{labeling on an outer **shell** } a = \frac{a_1 + a_2}{2}. \quad (4.11c)$$

Fig. 4.14a shows the $\overline{U}(\rho, z)$ for each of the cases in 4.11, calculated using a mitochondria with radius $a = 375\text{nm}$ following Equation 4.9. For each AuNP labeling distribution, the auto-correlation function $g(\tau)$ was calculated by simulating 10,000 diffusing mitochondria in 3D and taking the mean. In addition we randomized the radii of the mitochondria following a normal distribution centered at 375nm with a standard deviation of 100nm. This was done to approximate the variability in size of mitochondria inside a cell. The resulting $g(\tau)$ for the three labeling distributions and a diffusion constants of $D = 1 \times 10^{-3} \mu\text{m}^2/\text{s}$ are shown in Fig. 4.14b. As expected, the mitochondria labeled at the center had a $g(\tau)$ that is characteristic of a point particle. Because of their size, not pointlike diffusers take a longer time to pass through the observation volume which is evident from the larger MDF. This translates to shifts in the $g(\tau)$ of both the uniformly labeled and shell labeled mitochondria resulting in the overestimation of their τ_D . Interestingly, this effect is more pronounced with the shell-labeled mitochondria.

So far, we have investigated the effects of the size of AuNP-labeled mitochondria for a Gaussian approximation of the MDF. However, the Bessel-beam illumination of the poli-OCM produces prominent side lobes as seen in Fig 4.9. We account for this different illumination profile by changing $U(\rho, z)$ to

$$U(\rho, z) \propto \exp\left(-2\frac{\rho^2}{\omega_B^2}\right) J_0(k_B \rho) \exp\left(-2\frac{z^2}{z_B^2}\right). \quad (4.12)$$

Physically, the parameters ω_B , k_B , and z_B are determined by the beam waist of the heating beam (ω_B), the angle of the axicon (k_B), and the bandwidth of the broadband light source (z_B). For our simulation we obtained the values of these parameters by fitting the PSF of the poli-OCM.

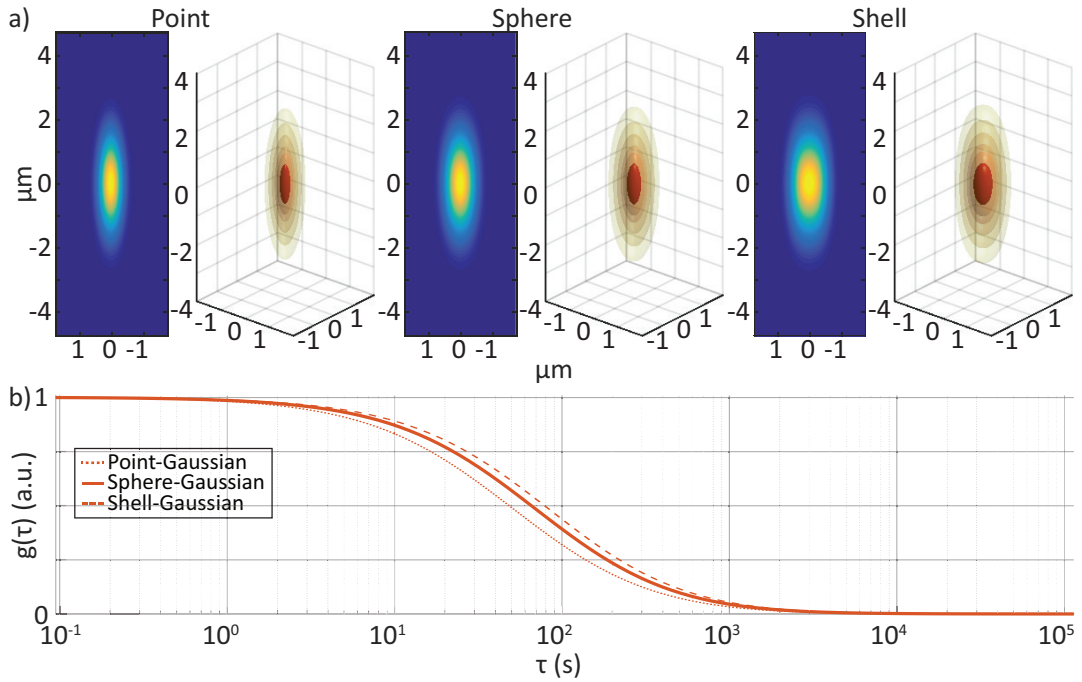


Figure 4.14 – a) Modified molecular detection functions for different labeling distribution of the mitochondria with 375nm radius (point, uniform sphere, and 20nm shell) shown as 2D slices and 3D intensity isosurfaces. b) Mean autocorrelation functions of 10000 diffusing mitochondria for different AuNP labeling distribution. The shift of $g(\tau)$ indicates the overestimation of τ_D for large diffusers.

The modified MDF for the different labeling distributions and their respective autocorrelation functions are shown in Fig. 4.15. As expected, we observe similar results compared to those in 4.14. The size of the mitochondria enlarged the modified MDFs causing the $g(\tau)$ to shift.

We aim to quantify the impact of mitochondria size and AuNP labeling distribution to temporal autocorrelation analysis based on poli-OCM imaging by establishing a “correction factor”. We calculated the $g(\tau)$ using the modified MDFs in Figures 4.14 and 4.15 for a range of diffusion constants from 10^{-4} to $10^{-2} \mu\text{m}^2/\text{s}$. Like in the previous calculations, 10,000 mitochondria with randomized radii were simulated for each diffusion constant. The diffusion parameters were extracted by fitting the resulting $g(\tau)$ with 4.2. We use 4.2 to extract the diffusion parameters so we can quantify the discrepancy between the theoretical diffusion of the mitochondria and the one measured using the free diffusion model for pointlike particles.

We plot the extracted diffusions parameters against the theoretical values and fit a curve to relate the two values. Fig. 4.16 shows the diffusion constants and τ_D along with their corresponding fits for both Gaussian and Bessel-beam PSFs. Based on these results, we observe

4.2. poli-OCM autocorrelation analysis for finite sized particles

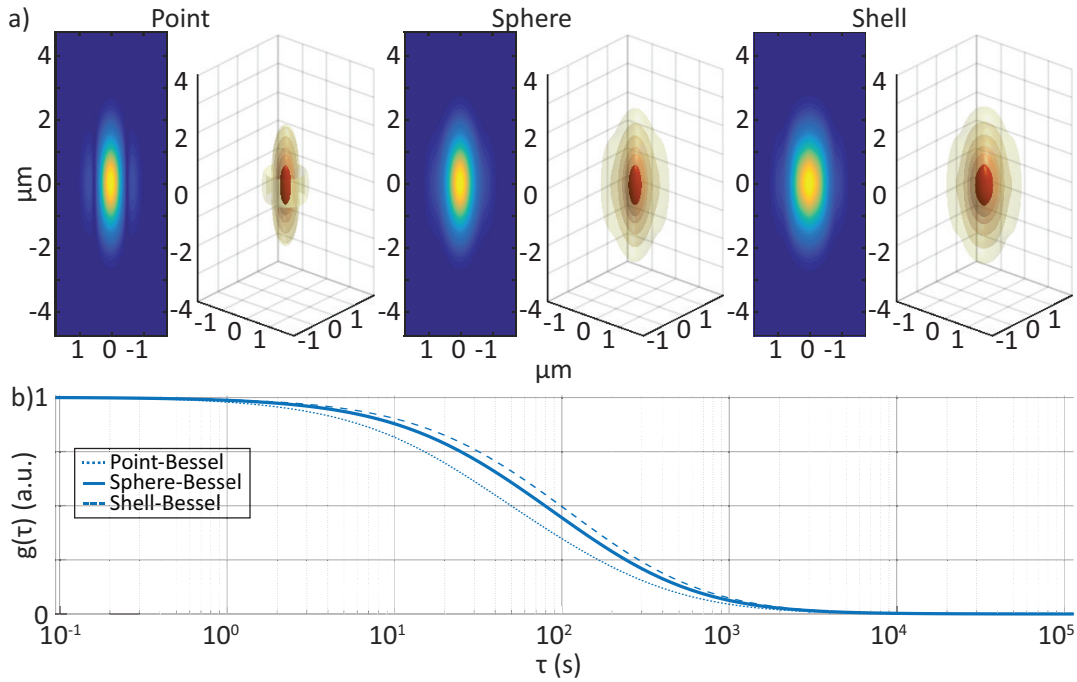


Figure 4.15 – a) Modified molecular detection functions for different labeling distribution of the mitochondria with 375nm radius (point, uniform sphere, and 20nm shell) considering the Bessel-beam illumination of the poli-OCM shown as 2D slices and 3D intensity isosurfaces. b) Mean autocorrelation functions of 10000 diffusing mitochondria for different AuNP labeling distribution. The shift of $g(\tau)$ indicates the overestimation of τ_D for large diffusers.

slower diffusion for Bessel-beam illumination compared to the Gaussian approximation for all cases of AuNP labeling distribution. This is simply attributed to the larger size of the MDFs due to the prominent side lobes of the Bessel-beam. Interestingly, the simulations predicted the same shift in $g(\tau)$ for the shell AuNP labeling distribution with Gaussian PSF and the uniform spherical AuNP labeling with Bessel-beam illumination. This resulted in a measured diffusion constant that is lower by a factor of 0.62 and 0.60 for the two cases respectively (1.63 and 1.62 for τ_D). In other words, the free diffusion model interprets the modification introduced by side lobes of the Bessel-beam like a shell surrounding a finite sized particle.

According to the results of these simulations, the modification of the MDF induced by the mitochondria size and AuNP labeling distribution resulted in a linear shift of the observed τ_D . This means that the “correction factor” is simply the slope of the line relating the calculated and theoretical values. The most pronounced effect was observed for the shell AuNP labeling with Bessel-beam illumination resulting in a calculated τ_D that was overestimated by a factor of 2.

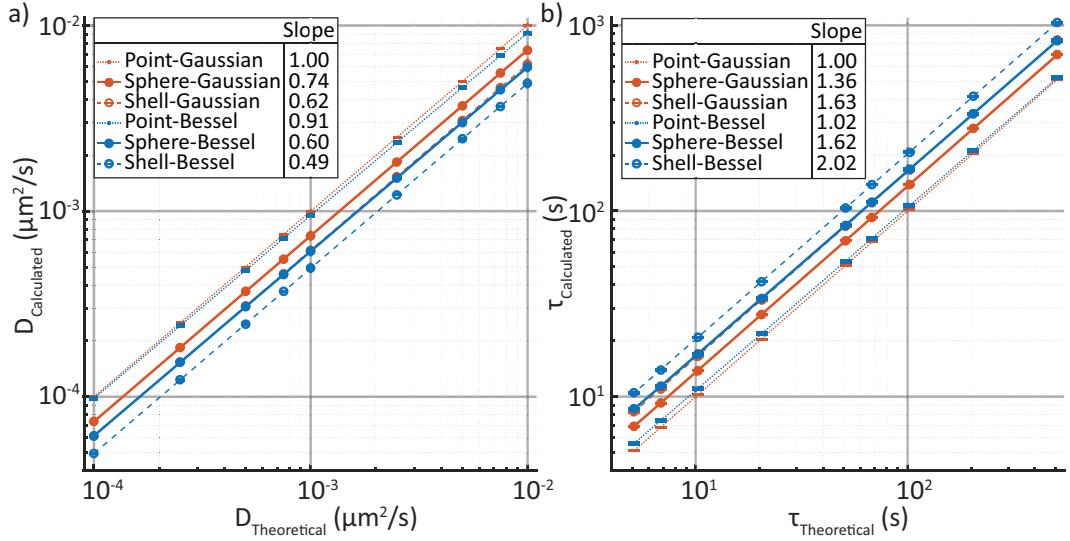


Figure 4.16 – Calculated diffusion constant(a) and time(b) plotted against theoretical values in logarithmic scale. The slope of the fitted line determines the “correction factor” needed to account for mitochondria size, AuNP labeling distribution, and Bessel-beam illumination of the poli-OCM.

Finally, we modify our simulations to investigating the impact of mitochondria size on their diffusion constant in addition to the modification it introduces to the MDFs. According to the Stokes-Einstein relation (Eq. 4.7) the size or hydrodynamic radius of a particle affects its diffusion coefficient. This holds true for mitochondria assuming they are in the same environmental conditions; that is, inside a medium with viscosity η and temperature T . In other words, instead of invoking that the 10000 simulated mitochondria are diffusing at the same constant D , we impose the condition that they are in the same medium. We implement this condition by assigning a theoretical diffusion constant D_{theo} for a mitochondrion with a radius of $r_{\text{mito}} = 375\text{nm}$. We further assume that the hydrodynamic radius of the mitochondria scales linearly with its physical radius such that the effective diffusion constant D_i for each mitochondrion with randomized radius r_i is given by

$$D_i = D_{\text{theo}} \frac{r_{\text{mito}}}{r_i}. \quad (4.13)$$

Fig. 4.17 shows the observed effective diffusion constant and time extracted from the simulations. These results display very similar effects as seen in 4.16. Autocorrelation analysis on imaging results using Bessel-beam illumination still measured slower diffusion. Similarly, the Gaussian PSF with shell labeling and the Bessel-beam PSF with uniform labeling returned nearly equal correction factors; ≈ 0.5 and ≈ 1.9 for diffusion constant and time respectively. The main noticeable difference between Fig. 4.16 and Fig. 4.17 are the “correction factors.”

4.2. poli-OCM autocorrelation analysis for finite sized particles

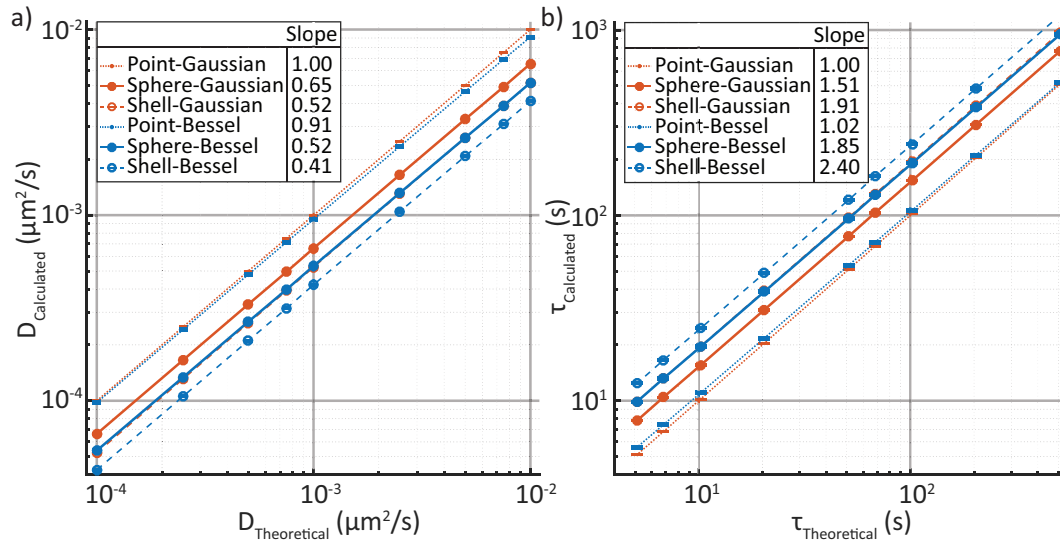


Figure 4.17 – Calculated diffusion constant(a) and time(b) plotted against theoretical values in logarithmic scale. The slope of the fitted line quantifies the “correction factor” considering mitochondria size effects on diffusion constant, AuNP labeling distribution, and Bessel-beam illumination of the poli-OCM.

In particular the “correction factor” for τ_D in the case of Bessel-beam illumination and shell AuNP labeling is now ≈ 2.4 instead of 2. This configuration is definitely the most significant for quantifying mitochondrial dynamics since we expect the AuNP labels to be mostly present on the outer mitochondrial membrane forming a shell. Therefore, a factor of 2.4 must be applied to the previously extracted diffusion parameters (Fig. 4.3) to achieve a more accurate quantification of mitochondrial dynamics. It is important to point out that we did not investigate the impact of different distribution mitochondria size heterogeneity. As previously mentioned our simulations only considered a normal distribution of mitochondria radii with a mean of 375nm and standard deviation of 100nm.

4.3 Quantifying mitochondrial dynamics via 3D single particle tracking

Quantification of mitochondrial dynamics using poli-OCM imaging and temporal autocorrelation analysis encounters issues with its accuracy due to the size of mitochondria. Because of the relative size of the mitochondria compared to the PSF of the poli-OCM, it is not viable to assume pointlike particles as in the conventional free diffusion model applied in FCS. We demonstrated that, in addition to the size of the mitochondria, the distribution of AuNP labels and the side lobes of the Bessel-beam introduces an overestimation of τ_D by as much as a factor of two. One way to circumvent this limitation is to use single particle tracking, which has achieved localization precision well below the size of the imaging PSF.

Journal article

Submitted in: Optics Letters, October 2017.

Quantifying mitochondrial dynamics via 3D single particle tracking

Miguel Sison^{1*}, Jérôme Extermann^{1,2}, Sabyasachi Chakraborty^{3,4}, Tanja Weil^{3,4}, Theo Lasser¹

¹Laboratoire d'Optique Biomédicale, École Polytechnique Fédérale de Lausanne, 1015 Lausanne, Switzerland ²Hepia, University of Applied Sciences of Western Switzerland (HES-SO), 4 rue de la Prairie, CH-1202 Genève, Switzerland ³Department of Organic Chemistry III/Macromolecular Chemistry, Ulm University, Albert-Einstein-Allee 11, 89081 Ulm, Germany ⁴Max-Planck-Institute for Polymer Research, Ackermannweg 10, 55128 Mainz, Germany

Mitochondria are highly dynamic organelles involved in a majority of cellular activities. In this letter we assessed mitochondrial dynamics by combining live cell photothermal optical coherence microscopy with single particle tracking analysis. Functionalized gold nanoparticles were used as mitochondria specific labels for poli-OCM imaging. For each cell sample, mitochondria diffusion and directional motion were measured based on time resolved mean square displacement data. Our results complement published work and demonstrate the usefulness of particle tracking for quantification of the slow mitochondrial mobility. Furthermore, we demonstrate the possibility of using our technique for distinguishing transitions between diffusive and directional mitochondria motion.

4.3. Quantifying mitochondrial dynamics via 3D single particle tracking

4.3.1 Introduction

Recent advances in bioimaging have given researchers powerful tools for investigating dynamic intracellular processes [132–134, 168]. In particular, quantification of disease linked enzyme activity and inhibition [169], spatially resolved protein dynamics inside the nucleus [170], protein-lipid binding [171], and the transport efficiency of membrane-anchored motors [172] were achieved using fluorescence correlation spectroscopy or single particle tracking in combination with these novel methods. However, the majority of these studies have mostly dealt with small particles or even single molecules. Larger organelles ($\approx 1\mu\text{m}$) do not only diffuse at a slower speed but are also often susceptible to crowding and confinement [161, 173], which imposes difficult border conditions to these so far successful correlation methods.

Mitochondria form a continuously reorganizing malleable meshwork [13] and are the primary producers of cellular ATP. Depending on cell activity, mitochondria undergo migration, fusion, and fission to sustain the cell's energy requirements [1, 137]. Since they play a crucial role in many cellular processes, abnormalities and dysfunction of mitochondrial dynamics have been associated with an array of human diseases [1, 13, 174].

M. Sison et al. [175] were able to quantify mitochondrial dynamics by merging photothermal optical coherence microscopy (OCM) [100, 175] with temporal autocorrelation analysis. They functionalized biocompatible gold nanoparticles (AuNPs) with mitochondria targeting groups, enabling three-dimensional mitochondria specific imaging of live cells for up to 3000 seconds. This allowed measurement and mapping of diffusion parameters demonstrating the high heterogeneity of mitochondrial dynamics inside living cells. Their temporal autocorrelation approach is closely related to fluorescence correlation spectroscopy and is therefore inherently limited by the molecular detection function (MDF).

In this letter, we quantified mitochondrial dynamics using three-dimensional particle tracking of AuNP-labeled mitochondria imaged using photothermal optical lock-in OCM (poli-OCM). We demonstrated the accuracy of our approach for slowly diffusing large (not pointlike) mitochondria confirming previously published data. In addition, we revealed the potential of particle tracking to easily distinguish and quantify between directional and diffusive motion of the mitochondria.

4.3.2 Methodology

The functionalized AuNPs used for targeting mitochondria act as localized hot spots while absorbing light from a photothermal heating beam. The heat dissipation into their immediate vicinity induces a local temperature increase causing thermal lensing, which is detected by a separate probe beam. Modulating the heating beam with a known fixed frequency induces a synchronously scattered signal with the same frequency, which is selectively filtered via lock-in

Chapter 4. Quantification of mitochondrial dynamics

detection [100]. Photothermal contrast has been shown as an effective mechanism for adding specificity to optical coherent tomography [176, 177] and microscopy [100, 175].

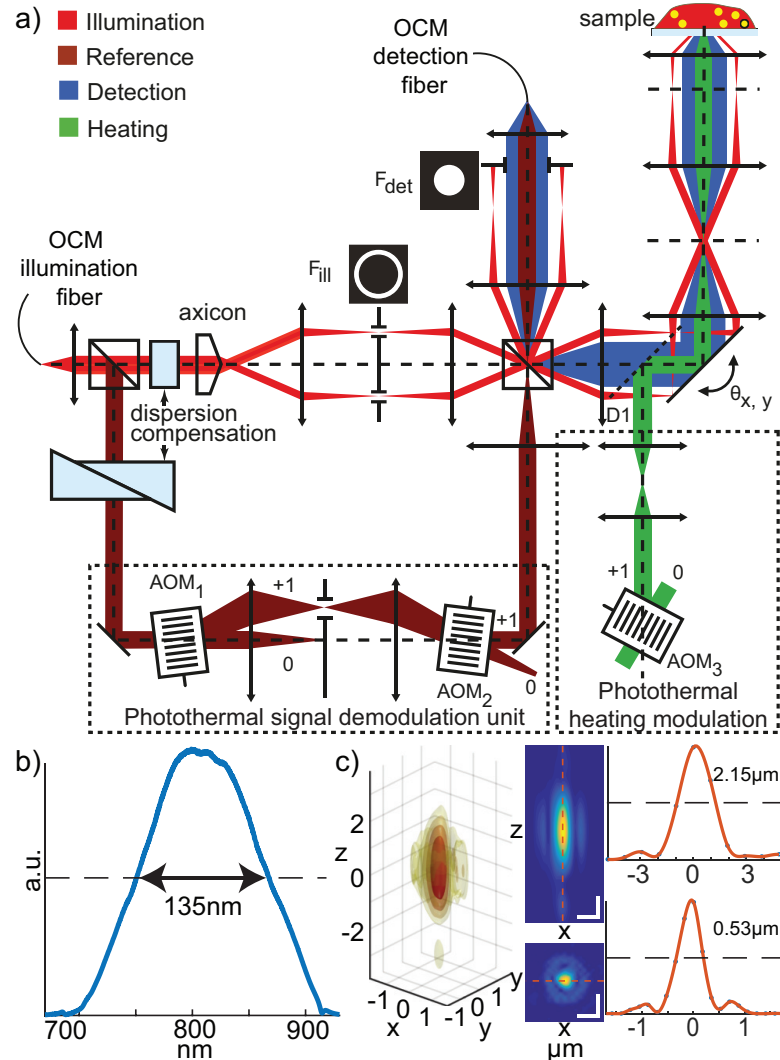


Figure 4.18 – a) Schematic of poli-OCM. An axicon in the illumination beam path ensures an extended focus. AOMs are used for intensity modulation of the photothermal heating beam and phase modulation of the reference beam. b) The spectrum of the broadband light source, centered at 800 nm ($\Delta\lambda = 135$ nm) for OCM imaging. c) The three-dimensional PSF of the poli-OCM shown in intensity iso-surfaces and slices along the $y=0$ (top) and $z=0$ (bottom) planes with line scans. Scale bars = 1 μm

The specifics of the poli-OCM as seen in Figure 4.18a, have been discussed in great detail [100].

4.3. Quantifying mitochondrial dynamics via 3D single particle tracking

Fundamentally, poli-OCM is based on dark-field OCM [30] with additions for photothermal excitation and optical lock-in detection. A broadband laser (Ti-Sa laser, Femtolasers Inc., Austria) centered at 800 nm with a bandwidth of $\Delta\lambda = 135$ nm (Figure 4.18b) is used as the probe for photothermal OCM imaging. Along the illumination path, an axicon (176° apex angle, Del Mar Photonics Inc., USA) shapes the light into a Bessel beam that propagates through a series of relay lenses and the scan unit [27]. The illumination beam is focused on to the sample with a $25\times$ NA = 0.8 water immersion objective (Carl Zeiss). As demonstrated in [27], the Bessel beam illumination provides a uniform lateral resolution over an extended depth of focus spanning far more than the entire thickness of a cell. Photothermal response is induced by exciting the AuNPs at their broad plasmonic resonance using an intensity modulated ($\Omega = 150$ kHz) 532 nm diode pumped solid state laser (Roithner Lasertechnik Inc., Austria). This photothermal heating beam is coupled into the scan unit using a dichroic mirror (D1; 720DCXR, Chroma Technology). On the reference path a pair of AOMs adds a synchronized phase modulation (Ω) on the reference field determined by the difference of their carrier frequencies ($\Omega = \omega_1 - \omega_2$). The backscattered field is superimposed with the phase modulated reference field and the resulting interference signal is detected by a custom built spectrometer. Switching Ω to 0 or 150 kHz allows choosing between the two imaging modalities of poli-OCM: (1) the dark-field mode for imaging the whole cell morphology and (2) the poli-mode for mitochondria specific imaging. The poli-OCM, as currently configured, has a measured (in PDMS) point spread function (PSF) with lateral and axial FWHM of $0.53 \mu\text{m}$ and $2.15 \mu\text{m}$ respectively (Figure 4.18c). During imaging, the cells were illuminated with 5 mW of the probe and 3 mW of the photothermal excitation beams inducing a temperature increase in the order of ≈ 1 K [100].

The mitochondria of living HeLa cells were labeled with functionalized AuNPs following the procedure published in [175]. During imaging the cells were housed inside a custom built temperature stabilized (37°C) micro-incubator with a constant supply of humidified premixed air (5% CO₂). Time-lapse images of both mitochondria motion and full cell morphology were acquired by alternating between the two modalities of the poli-OCM.

An integration time of $250 \mu\text{s}$ with a line scan rate of 3.9 kHz was used for the tomogram acquisition in accordance with [100]. The scan range was adjusted to fit the entire cell within the field of view while maintaining spatial sampling at $\approx 0.41 \mu\text{m}/\text{pixel}$. The effective frame rate is therefore determined by the size of the cell being imaged. The trajectories of the AuNP-labeled mitochondria were acquired using the Trackmate plugin of Fiji [178, 179]. Figure 4.19a shows three-dimensional volume renderings of the time-lapse tomograms illustrating the whole cell in grey and the AuNP-labeled mitochondria as yellow spheres. Two representative trajectories are shown in Figure 4.19b with the corresponding tracked AuNP-labeled mitochondria marked by red spheres (Figure 4.19 a and b).

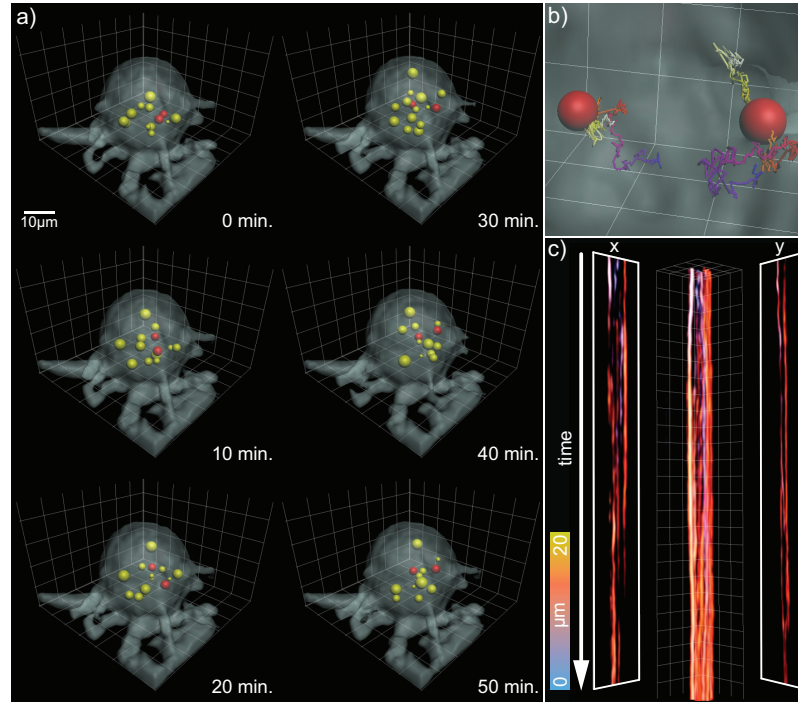


Figure 4.19 – a) Three-dimensional rendering of the full cell morphology (grey) and the AuNP-labeled mitochondria (yellow and red spheres). b) Representative trajectories (time color-coded from purple to white) of 2 tracked AuNP-labeled mitochondria (red spheres). c) Kymographs along the x- and y-planes showing the motion of the AuNP-labeled mitochondria; the color depicts movement along the z-directions as indicated by the colorbar

4.3.3 Results and Discussion

The probability $p(r, t|r_0, \Delta t)$ of finding a particle, undergoing free diffusion in three-dimensions, at position r after a time interval Δt is

$$p(r|r_0, \Delta t) = \left(\frac{1}{4\pi D\Delta t} \right)^{\frac{3}{2}} \exp\left(-\frac{(r-r_0)^2}{4D\Delta t} \right); \quad (4.14)$$

where D is the diffusion constant and r_0 is its initial position [180]. The mean square displacement $msd(\Delta t)$ of the diffusing particle can then be derived from Equation 4.14 as

$$msd(\Delta t) = \langle (r-r_0)^2 \rangle = 6D\Delta t. \quad (4.15)$$

Figure 4.20 shows the mean $msd(\Delta t)$ (black lines) obtained by averaging the $msd(\Delta t)$ traces of all mitochondria trajectories within one cell and the blue shaded regions mark the standard error of the mean. Mitochondria diffusion coefficients were then extracted from the weighted

4.3. Quantifying mitochondrial dynamics via 3D single particle tracking

fits (red line) following Equation 4.15. The weights were based on the statistical degrees of freedom of the mean $msd(\Delta t)$.

The diffusion coefficients of Cell 1 and 2 (Figure 4.20 a and b), obtained via particle tracking, are $1.8 \times 10^{-3} \mu\text{m}^2/\text{s}$ and $5.3 \times 10^{-3} \mu\text{m}^2/\text{s}$ respectively. These values fall within the range published in [175] but both generally imply slightly faster mitochondria diffusion. This offset between the diffusion coefficient measured by the two techniques can be attributed to how the PSF and dimensions of the mitochondria affect particle tracking and correlation analysis. Unlike correlation analysis, the accuracy of particle tracking is more dependent on the precision of localization rather than the resolution of the optical system. An optical microscope has a PSF with FWHM of $\approx 0.5 \mu\text{m}$, whereas particle tracking and localization algorithms have demonstrated localization precision well below $<100 \text{ nm}$ [178, 181, 182]. In our measurements we record a median step size of 117 nm laterally and 144 nm axially (mean 215 nm and 256 nm respectively). This high localization precision enables discriminating changes in position smaller than the resolution limit, which is necessary for accurately describing slowly diffusing particles like mitochondria. In contrast, correlation analysis measures the signal fluctuation as a diffusing particle transitions through an observation volume characterized by the PSF. Typically, correlation analysis assumes point diffusers. However, it has been shown that maintaining this assumption for large diffusing particles like the mitochondria results in underestimated diffusion constants [164, 165].

As opposed to the first two cell samples, Cell 3 features a non-linear $msd(\Delta t)$ that increases at larger Δt . Adding a drift or flow with constant velocity V_f to free diffusion [183, 184] modifies the probability function in Equation 4.14 to

$$\begin{aligned} p_f(r|r_0, \Delta t) &= \left(\frac{1}{4\pi D \Delta t} \right)^{\frac{3}{2}} \exp\left(-\frac{(r - r_0 - V_f \Delta t)^2}{4D \Delta t} \right) \\ &= p(r|r_0, \Delta t) \exp\left(\frac{V_f (2(r - r_0) - V_f \Delta t)}{4D} \right); \end{aligned} \quad (4.16)$$

with $msd(t)$ given by

$$msd(\Delta t) = \langle (r - r_0)^2 \rangle = 6D\Delta t + V_f^2 \Delta t^2. \quad (4.17)$$

From these equations, it is easy to see that the inclusion of directional motion results in a non-zero first moment of the probability distribution. However, even accounting for a constant flow, Equation 4.17 still does not sufficiently characterize the motion of AuNP-labeled mitochondria for Cell 3. Inspecting the raw data, we saw that starting at the ≈ 5000 second mark (dashed line in Figure 4.20c), the AuNP-labeled mitochondria transitions from free diffusion to a more directed flow. We segmented the trajectories and recalculated the $msd(\Delta t)$ only starting from the 5000 second mark. We then fitted Equation 4.17 on the $msd(\Delta t)$ of this segment as

Chapter 4. Quantification of mitochondrial dynamics

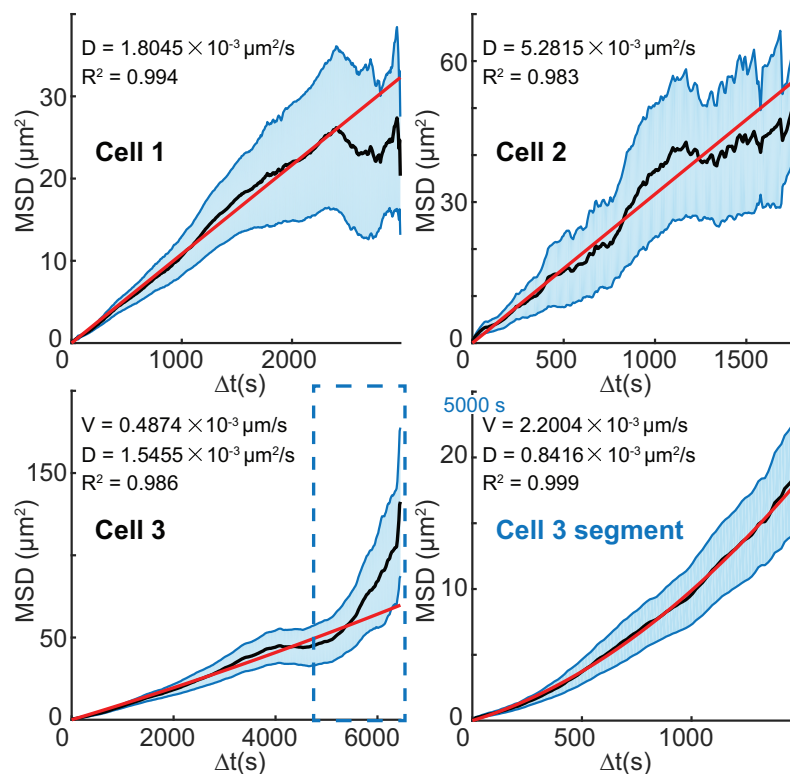


Figure 4.20 – a)-c) $msd(\Delta t)$ of Cells 1 to 3 with the corresponding diffusion constant and velocity obtained from the fits following Equations 4.15 or 4.17. d) Gives the $msd(\Delta t)$ from segmented trajectories of Cell 3 starting from 5000 to 6450 seconds.

seen in 4.20d. This allowed us to quantify two distinct dynamic states of the AuNP-labeled mitochondria. The velocity of the AuNP-labeled mitochondria increased by more than 3 \times , from $0.49 \times 10^{-3} \mu\text{m/s}$ to $2.2 \times 10^{-3} \mu\text{m/s}$ while the diffusion coefficient was reduced by almost half, from $1.5 \times 10^{-3} \mu\text{m}^2/\text{s}$ to $0.8 \times 10^{-3} \mu\text{m}^2/\text{s}$.

4.3.4 Conclusion

The execution of numerous cellular activities involves mitochondrial dynamics. The size of mitochondria makes them prone to intracellular crowding and confinement rendering quantification of mitochondrial diffusion difficult for fluorescence correlation spectroscopy and other similar techniques. Here we have demonstrated the practicability of three-dimensional particle tracking analysis based on time-lapse poli-OCM imaging for quantifying mitochondrial dynamics. Furthermore, we have demonstrated that the high localization of particle tracking translates to improved accuracy ideal for measuring the slow mitochondria diffusion.

4.3. Quantifying mitochondrial dynamics via 3D single particle tracking

Lastly, we establish the capability of our approach for identifying the transition between diffusive and directional mitochondrial motion as well as quantitatively differentiating these states. Transitioning between these states of motion comes with complexity not easy to integrate in a correlation analysis. The simplicity and accuracy of poli-OCM based particle tracking complements the three-dimensional mapping of mitochondrial dynamics achievable with correlation analysis [175].

4.4 Summary

In this chapter we developed two techniques for quantifying mitochondrial dynamics based on time-lapse poli-OCM imaging. The first technique (4.1) employed temporal autocorrelation analysis and fitting with a classical free diffusion model to extract mitochondrial diffusion parameters. With this analysis we demonstrate the high heterogeneity of mitochondrial diffusion inside a living cell. Furthermore, these quantified parameters are spatially resolved and can be linked to each voxel within the cell. This allowed us to generate three-dimensional diffusion parameter maps, which we can use to identify and locate regions inside the cell where mitochondria undergo fast and slow diffusion.

In 4.2 we also investigated the effect of assuming point like diffusers as in the classical diffusion model despite the non-negligible dimensions of the mitochondria compared to the size of the PSF. Furthermore, we determined the effect of using a Bessel-like illumination PSF, like with the poli-OCM, compared to the conventional Gaussian PSF. We also considered the non-uniform size of mitochondria within a cell and different AuNP labeling distributions. We conducted this analyses by numerical simulations while modifying the effective molecular detection function of the system. The simulations revealed that, as expected, maintaining the assumption of point-like diffusers and a Gaussian PSF results in overestimated diffusion times. Our analysis gave as a means to address this over estimation depending on the parameters of our system using a “correction factor” which can be calculated through the simulations.

Finally, the second technique we developed, as presented in 4.3, made use of single particle tracking (SPT). An SPT approach, unlike temporal autocorrelation analysis, is not limited by the PSF of the system. Different localization and tracking algorithms have demonstrated localization precisions that are well below the dimensions of the PSF as long as the signal to noise ratio (SNR) is sufficient. Considering this, mitochondria specific poli-OCM imaging is very well suited for SPT due to the high sensitivity of the poli-OCM signal. Furthermore, the stability of the AuNP labels allowed us to image continuously for more than 6000 seconds without any observable degradation of contrast. The better localization precision of SPT enabled us to extract diffusion constants with more accuracy. We also showed the possibility of using SPT for identifying and differentiating the change in mitochondrial dynamics from diffusive to directional motion. However, SPT as we have implemented it does not allow us to map the diffusion parameters within the cell.

Temporal autocorrelation analysis and SPT, individually, have their advantages. These two techniques can be used to complement each other in quantifying mitochondrial dynamics and provide us with a more complete understanding of this phenomenon.

5 Outlook: Mitochondrial dynamics in the Cockayne Syndrome

The Cockayne syndrome (CS) is a very rare yet severe genetic disorder causing neurodegeneration and developmental deficiency [37]. It is inherited in an autosomal recessive manner, which means both parents need to carry the mutation for it to be transmitted [185]. Mutations in the CSA or CSB gene products are the known causes of CS [186, 187]. Despite its low incidence, CS causes dramatic premature aging leading up to eventual death often within the first or second decade of life [188]. Patients afflicted with this disease suffer through dental caries, visual and hearing impairment, photosensitivity, microcephaly, ataxia, and muscle weakening and atrophy while they live [37, 185, 189, 190]. Including these symptoms, CS shares phenotypic similarities with other neurodegenerative and mitochondrial diseases [191].

CS is also categorized as DNA repair-deficient disease characterized by defective transcription-coupled nucleotide excision repair (TCR) [38, 39]. TCR allows the cell to remedy damaged DNA by removing DNA lesions or adducts [192]. Impaired TCR could explain the photosensitivity of CS patients by preventing the cell from repairing UV-induced damage to the DNA. Mutations with CSA or CSB are also known causes of another TCR-deficient disease called UV-sensitive syndrome (UVSS) [193]. Whereas UVSS exhibits photosensitivity and mild skin abnormalities, it is not known to share the other symptoms of CS relating to neurodegeneration and aging [194]. The impact of CSB and UV stimulated scaffold protein A (UVSSA, a gene associated with UVSS) mutations to ROS were investigated, which revealed CSB-deficient cells exhibited elevated levels of ROS while the UVSSA mutants did not [38]. It was proposed that, on top of its other roles, CSB acts as an electron sink arresting increased ROS levels and protecting against nuclear DNA damage [38]. These seem to indicate the uncoupling of CS impact to UV response and mitochondrial function. In a study by Aamann et al., CSB-deficient cells experienced a decrease in mitochondrial base excision repair (BER) activity [37], which may lead to increased levels of oxidized DNA [195] and mtDNA [38, 196]. Consequently, this reduced BER activity promoted mitochondrial dysfunction that could increase ROS production, which in turn expose mtDNA to ROS-induced damage even more [37]. This cyclic interaction between ROS

Chapter 5. Outlook: Mitochondrial dynamics in the Cockayne Syndrome

and mitochondrial dysfunction is reminiscent of AD and might point to the cause of the rapid aging experienced by CS patients. CSB impairment has also been linked to abnormal mtDNA replication by deregulating the mitochondrial DNA polymerase γ (POLG1) [39]. CSB-deficient cells revealed mitochondrial function impairment and reduced OXPHOS due to the depletion of POLG1, which could be reversed to some degree via treatment with ROS scavengers [39].

There is clearly a need to investigate the role of mitochondrial dysfunction in the pathogenesis of CS. In this pilot study, we exploited the AuNP based mitochondria specific poli-OCM imaging and analysis techniques we developed to investigate the mitochondrial dynamics of CS cell lines. To the best of our knowledge there is no existing method for imaging and quantifying the effect of CS on mitochondrial dynamics. In our experiments we used the CSB-deficient CS1AN-SV and CSB-proficient MRC5-SV, both which are immortalized Simian Virus 40 transformed human fibroblast. For specific poli-OCM imaging, we used the same mitochondria targeting AuNP labels described in 4.1.2.

5.1 CS cell viability with AuNP-mitochondria labeling

Before initiating the time-lapse poli-OCM imaging experiments, we first examined the viability of both MRC5-SV and CS1AN-SV incubated with the mitochondria targeting AuNPs. The test we conducted was qualitative with the aim of establishing cell viability in conditions approximating what they will be exposed to during imaging. Different cultures were prepared each having different concentration of AuNPs. Specifically we used 0.031 nM, 0.155 nM, 0.31 nM, 1.55 nM, and 3.10 nM as well as a control group without AuNPs for a total of 6 cases. For both cell lines each case was replicated 4 times and cell growth was monitored over 5 days or until the cultures reached confluency. The cell cultures were kept in an environment similar to an actual poli-OCM imaging experiment excluding the intermittent exposure to laser light. We observed no appreciable difference in cell growth among the different AuNP concentrations, all of which grew to confluency at the same rate as the control group. The only noticeable discrepancy was the difference in growth rate between the two cell lines. The MRC5-SV cultures reached confluency after 4 day while the CS1AN-SV cultures needed approximately 1 day more. We used the same seeding concentration in all wells which was 2000-4000 cells per 1 cm² of growth area. For a more quantitative analysis on the impact of the AuNP labels to the CS cell lines a test similar to that described in 4.1.4 should be conducted.

5.2 Quantifying CS mitochondrial dynamics

After ensuring the viability of the CS cell lines with AuNP labeling we proceeded with the time-lapse poli-OCM imaging experiment to acquire the necessary data for quantifying CS mitochondrial dynamics. We labeled MRC5-SV and CS1AN-SV cell cultures with mitochondria

5.2. Quantifying CS mitochondrial dynamics

targeting AuNPs following the procedures discussed in 3.1, 4.1.4, and 4.3.2. Briefly, we plated ≈ 2000 – 4000 cells per well onto Ibidi μ -slide 8-well with $250 \mu\text{L}$ of cell culture medium. We incubated the cells with 0.31 nM of AuNP labels for 12 hrs and then washed prior to the experiment. During imaging the cells were housed inside a the micro-incubator at 37°C with $5\% \text{ CO}_2$ humidified air. The tomograms were acquired with 5 mW of photothermal heating and 6 mW of OCM probe beam powers.

Sample images of CS1AN-SV cells with AuNP-labeled mitochondria acquired with the poli-OCM are shown in Fig. 5.1. In particular, Fig. 5.1 a and b feature cross-sectional and orthogonal slices along the dashed yellow line of dfOCM and poli-OCM tomograms respectively. The dfOCM image clearly shows the morphology of these cells including the well discernible lamellipodia. We also observe that these fibroblasts are very thin; except for one or two that seem to be swelling, most are $<10 \mu\text{m}$ thick. From our experience with imaging HeLa cells, round swollen cells that are still well attached are indicative of cells about to go into mitosis. Fig. 5.1c is a depth color coded maximum intensity projection of the poli-OCM image showing the location of the AuNP labeled mitochondria inside the cells. As seen from the color of this image, most of the AuNPs are found within $5 \mu\text{m}$ of depth, which further alludes to the thinness of these cells.

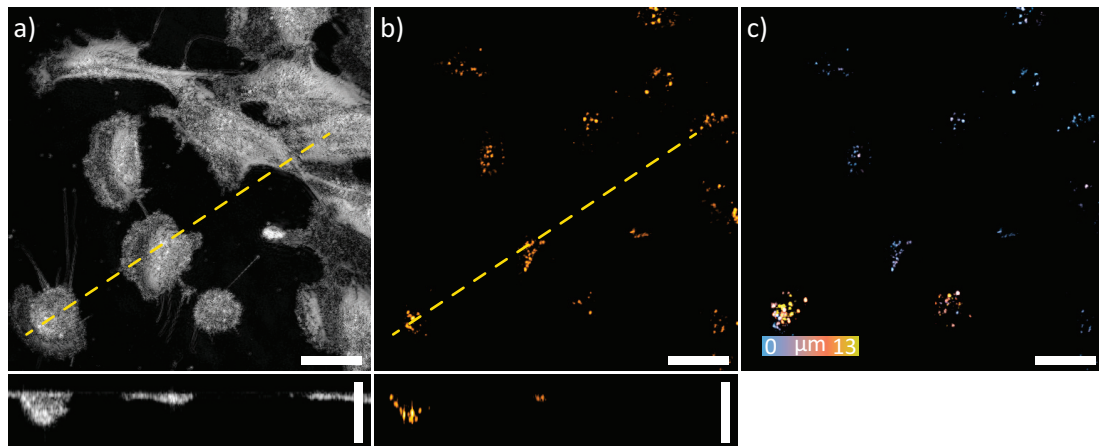


Figure 5.1 – Cross-sectional slices of a) dfOCM and b) poli-OCM tomograms and orthogonal slices taken along the dashed yellow line. c) is a maximum intensity projection of the poli-OCM tomogram with the color code indicating depth information. Scalebar: $35 \mu\text{m}$.

In order to quantify mitochondrial dynamics, we then conducted time-lapse poli-OCM imaging of MRC5-SV and CS1AN-SV cells with AuNP-labeled mitochondria. Similar to 4.1.4 and 4.3.2, we limit ourselves to one cell per time-lapse data set and adjusted the scan range to cover its whole area while maintaining a pixel sampling of $0.41 \mu\text{m}$ along the lateral direction. We acquired alternating dfOCM and poli-OCM tomograms using an integration time of $250 \mu\text{s}$ in accordance with [100]. This means that the acquisition rate or time difference

Chapter 5. Outlook: Mitochondrial dynamics in the Cockayne Syndrome

between two successive three-dimensional tomograms is determined by the size of the cell being imaged. For each cell we imaged continuously for a total of 2 hours (7200 seconds).

In Fig. 5.2 we show histograms of mitochondrial diffusion time, τ_D , from four cells of each cell line. The τ_D and other mitochondrial diffusion parameters were extracted via temporal autocorrelation analysis and fitting with a classical diffusion model. As with the results in 4.1.2, these τ_D values are spatially resolved and can be mapped in three-dimensions to their respective voxels within the cell. These histograms characterize the probability distribution of τ_D and illustrate the heterogeneity of mitochondrial dynamics within one cell and across the cell line. Furthermore, these histograms have a logarithmic time scale to better visualize the broad distribution of τ_D values that goes from ≈ 50 -5000 seconds.

Looking at these histograms, we see that there is a slightly larger variation with the mean τ_D for MRC5-SV (≈ 400 -1500 seconds) compared to CS1AN-SV (≈ 500 -1300 seconds). Interestingly, it also appears that the τ_D distributions of the CS1AN-SV cells are more uniform compared to the MRC5-SV cells. The τ_D distributions of CS1AN-SV Cell 1, 2, and 4 have more or less the same shape with similar peaks at ≈ 200 -250 seconds. Whereas CS1AN-SV Cell 3 was slightly different, having a broader τ_D distribution with a peak that is not as well defined. In contrast, the τ_D distributions of the MRC5-SV cells are more varied. MRC5-SV Cell 1 and 2 have τ_D values that are distributed more evenly over the entire range of the histogram. On the other hand, the τ_D distribution of MRC5-SV Cell 3 has a very well defined peak and the distribution decays soon after 2000 seconds. As for MRC5-SV Cell 4, it also had a narrower distribution with a peak at ≈ 150 -200 seconds similar to MRC5-SV Cell 3. However, unlike MRC5-SV Cell 3, the distribution of MRC5-SV Cell 4 had a second peak after 2000 seconds and is in fact closer to CS1AN-SV Cell 2 and 4. Despite these noticeable differences there is still no clear or defining characteristic that differentiates the τ_D probability distributions of MRC5-SV from CS1AN-SV.

We also analyzed the time-lapse data set using the single particle tracking analysis that was discussed in 4.3. Fig. 5.3 shows the mean $msd(\Delta t)$ plots for each of the 8 cells with their corresponding fits and diffusion constants. The mean $msd(\Delta t)$ is calculated from the trajectories of all tracked AuNP-labeled mitochondria within each cell. The blue shaded region around the mean $msd(\Delta t)$ represents the range covered by the standard error of the mean. As in 4.3.3, the diffusion constants were obtained from the slopes of the weighted fits of the mean $msd(\Delta t)$ with Eq. 4.15. Again, we used the statistical degrees of freedom of the mean $msd(\Delta t)$ as weights since there were much fewer points used to calculate the $msd(\Delta t)$ at larger Δt 's. This is the reason why the fitted lines are more representative of $msd(\Delta t)$ at smaller Δt 's. Based on the acquired diffusion constants, it is again difficult to differentiate MRC5-SV from CS1AN-SV. All 8 cells had diffusion constants ranging from ≈ 0.9 - $4.0 \times 10^{-3} \mu\text{m}^2/\text{s}$ with the MRC5-SV cells having a slightly shorter range of ≈ 1.6 - $3.7 \times 10^{-3} \mu\text{m}^2/\text{s}$. What is more interesting is the shape of the mean $msd(\Delta t)$ plots. Aside from CS1AN-SV Cell 3 and MRC5-SV Cells 3 and 4, most of

5.2. Quantifying CS mitochondrial dynamics

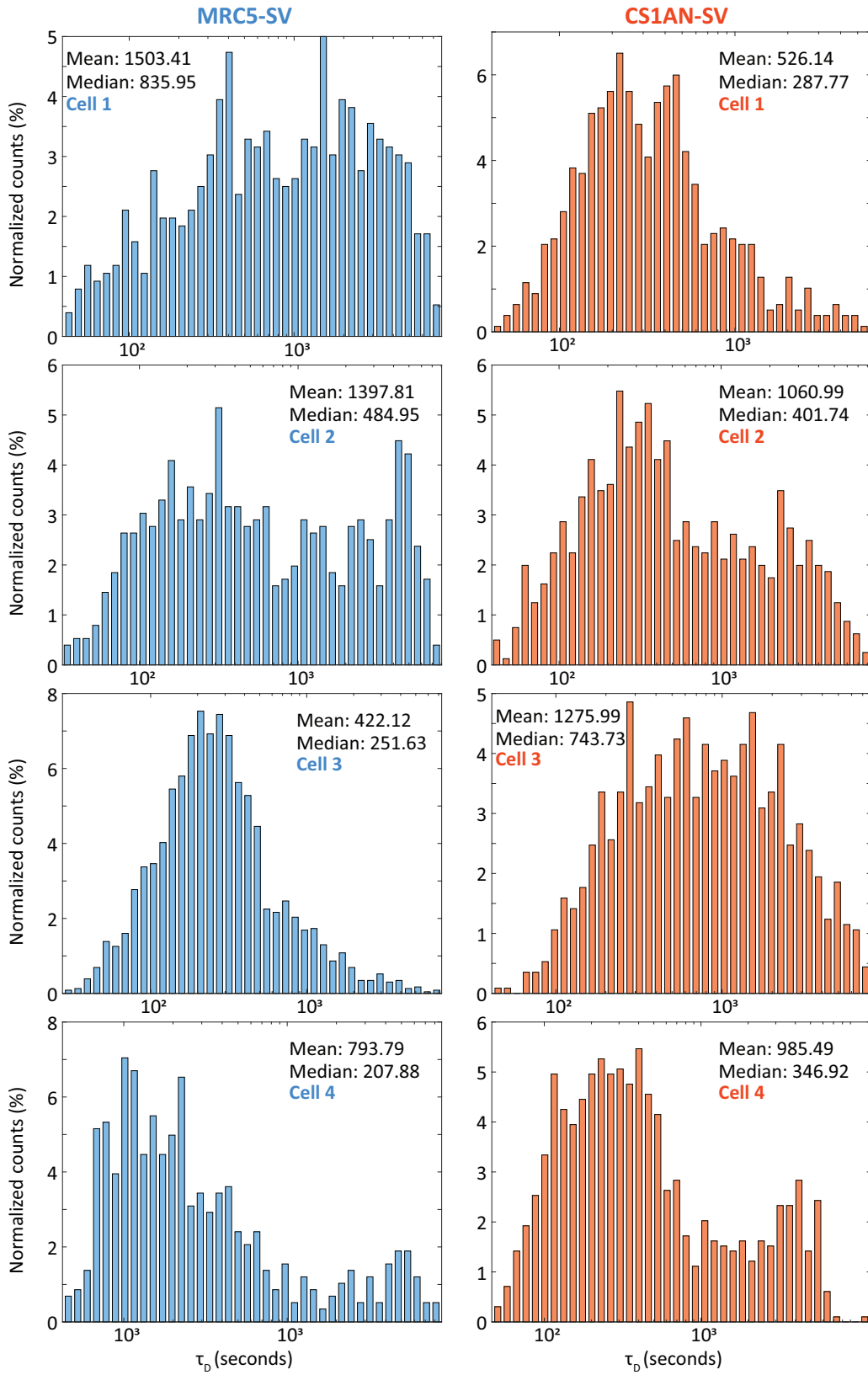


Figure 5.2 – Probability distribution of the extracted mitochondrial diffusion time, τ_D , for each cell from the MRC5-SV and CS1AN-SV cell lines.

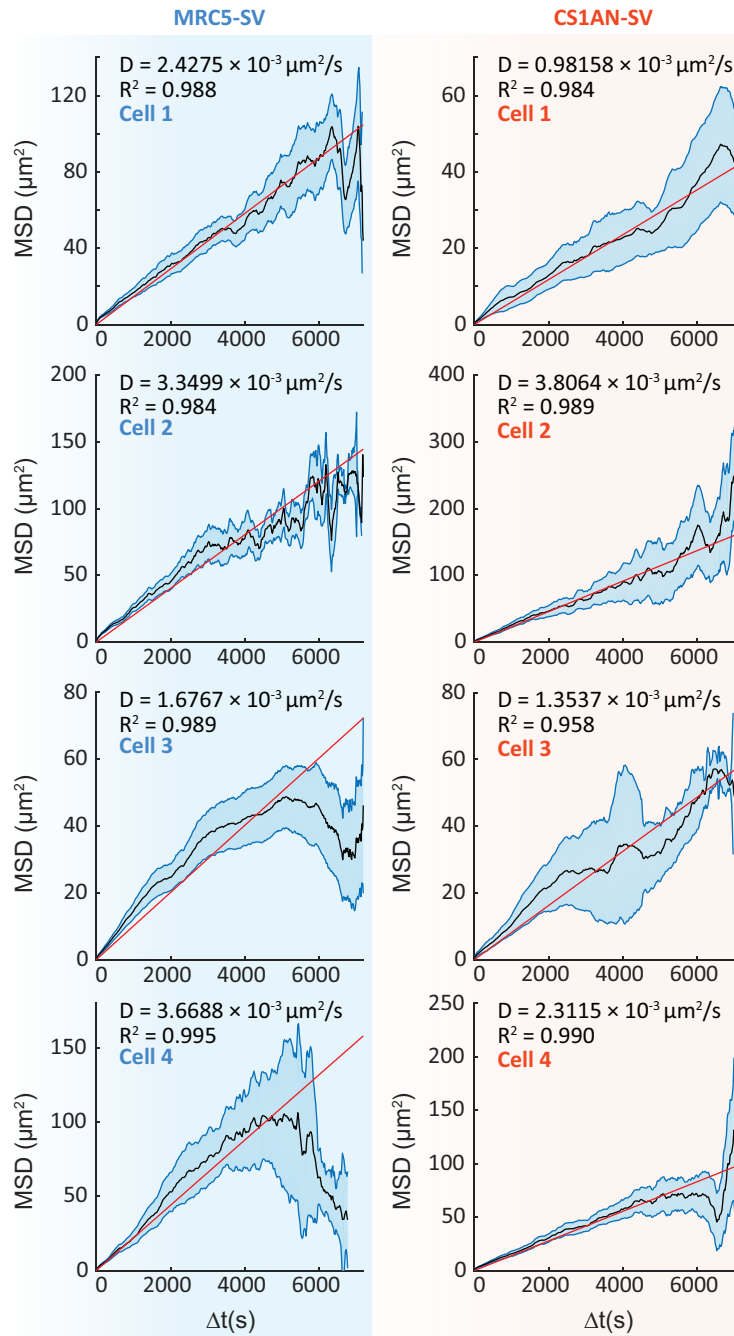


Figure 5.3 – Mean $msd(\Delta t)$ plots calculated from all tracked AuNP-labeled mitochondria within one cell. The fits are weighed with the statistical degrees of freedom of the mean $msd(\Delta t)$ and the diffusion constant is extracted from the slope following Eq. 4.15. The standard error of the mean is indicated by the blue shaded around the mean $msd(\Delta t)$

the cells had linear mean $msd(\Delta t)$ plots. This linear trend indicates free diffusion according to Eqs. 4.14 and 4.15 and as discussed in 4.3.3. The mean $msd(\Delta t)$ plot of CS1AN-SV Cell 3 could still approximate a linear trend in spite of the non-negligible undulation from $\Delta t = 2200$ to 4500 seconds. The standard error of the mean also has its largest values within this range before decreasing starting at $\Delta t=4200$ seconds. This trend of the standard error of the mean is unique to CS1AN-SV Cell 3 and not shared by the other samples. Lastly, both MRC5-SV Cells 3 and 4 mean $msd(\Delta t)$ plot that started with an initially linear slope that progressively decreased with increasing Δt . This kind of mean $msd(\Delta t)$ could indicate a diffusing particle that is restricted by a potential or that the diffusion area is shrinking [197, 198].

5.3 Summary

We conducted time-lapse mitochondria specific poli-OCM imaging of immortalized CS diseased and control cell lines, CS1AN-SV cells and MRC5-SV respectively. From this time-lapse data we quantified the mitochondrial dynamics of both cell lines using temporal autocorrelation and single particle tracking analyses. The characteristics of the resulting τ_D probability distributions were insufficient to definitively distinguish the two cell lines from each other. Similarly, the variation of extracted diffusion constant from the single particle tracking and $msd(\Delta t)$ analysis was not significant to differentiate these cells. It is clear that more data is needed to establish statistically significant information before we can conclude on the difference or similarities of these known CS cell models.

We should take note that this was only a pilot study with the purpose of exploring the possibility of quantifying the mitochondrial dynamics of CS cell lines using mitochondria specific poli-OCM imaging. It was important to establish the viability of these cell lines with AuNP labeling as not to perturb the biological phenomena we aim to investigate. It was equally important to achieve time-lapse poli-OCM over extended time durations without causing cell death or any appreciable adverse cell reaction. We were able to achieve continuous mitochondria specific poli-OCM imaging for up to 2 hours (7200 seconds) using 5 mW and 6 mW of photothermal heating and OCM probe beam powers respectively. Furthermore, the stability and contrast of the poli-OCM was sufficient to perform temporal autocorrelation and single particle tracking analyses on the same datasets. Based on these findings, we are convinced that further investigation of CS mitochondrial dynamics based on poli-OCM imaging is definitely worth pursuing. As previously mentioned, it is important to acquire time-lapse data from a statistically significant number of cells for each cell line being investigated. By doing so, we can establish parameters that will allow us to characterize different cell lines and analyze the relationship between the Cockayne Syndrome and mitochondrial dynamics. Once achieved, future studies can delve into imaging and quantifying the response of CS mitochondrial dynamics to various stimulants, physiological conditions, or proposed treatment at a cellular level.

6 Conclusion

This thesis was aimed at developing imaging based techniques for the quantification of mitochondrial dynamics. This was achieved by exploiting the speed, stability, and specificity provided by poli-OCM. Specifically, we accomplished three-dimensional mitochondria specific imaging using functionalized AuNPs as photothermal bio-markers for poli-OCM imaging. We quantified mitochondrial dynamics by extending methods for analysis, mostly reserved to fluorescence techniques, to three-dimensional time-lapse poli-OCM imaging. Moreover, we presented initial results demonstrating the possibility of using the techniques we developed for investigating the mitochondrial dynamics of diseased cell lines. This is arguably an unprecedented achievement that, to the best of our knowledge, has not been attempted on this time scale.

The functionalization of AuNPs played a crucial role in realizing the goals of this thesis. One distinctive limitation of the OCM is its lack of specificity. Unfortunately, coherence based techniques do not have an established counterpart to the fluorophores that provide molecular specificity to confocal microscopy. For OCM imaging this limitation was surmounted by the invention of poli-OCM. Photothermal imaging using functionalized AuNPs as bio-markers has substantial advantages over confocal fluorescence microscopy. In general, AuNPs are chemically stable, biocompatible, and do not photobleach. In this thesis we presented two biopolymer based surface coatings that were used to functionalize the AuNPs. Surface functionalization of AuNPs with these polymer coatings improved biocompatibility, cellular uptake, and solubility in biological media. Both surface coatings utilized triphenyl-phosphonium (TPP), a molecule known for selective accumulation to the mitochondria, to impart the AuNPs with mitochondria specific labeling. The first surface coating we present is based on the polycationic denatured blood plasma protein human serum albumin (dcHSA-PEO-TAT-TPP). This copolymer coating has an increased number of reactive sites that allows for more chemical modifications, which can further lead to a multifunction nanolabel or nanotransporter [124]. We optimized the labeling concentration of dcHSA-PEO-TAT-TPP functionalized AuNPs for

Chapter 6. Conclusion

poli-OCM imaging and showed that above 13.4 nM the improvement with the poli-OCM signal diminishes. The second surface coating we used is based on globular cationic bovine serum albumin (gcBSA-TPP). We were able to achieve mitochondria specific time-lapse poli-OCM imaging using gcBSA-TPP AuNPs at only 0.31 nM labeling concentration. Despite this low concentration, the poli-OCM signal had sufficient contrast, lasting for at least 2 hours without any observable decrease in signal strength, and allowed us to quantify mitochondrial dynamics using temporal autocorrelation and single particle tracking analysis. As a demonstration of the versatility of our method, we also conducted poli-OCM imaging using gold nanorods and fluorescent nanodiamond gold nanoparticle dimers [127].

These novel biopolymer surface coatings and uniquely structured functionalized nanolabels give us a few possibilities for future studies. First, the use of multifunctional copolymer coatings allows for targeted drug delivery with gold nanotransporters, which we can monitor via poli-OCM imaging. Furthermore, using the techniques we develop, we are well-equipped to investigate and quantify the impact of these nanotransporters and the substances they deliver to cellular activities such as mitochondrial dynamics. Second, the use of uniquely structured AuNPs or AuNRs may lead to “multicolor” poli-OCM imaging and even a three-dimensional photothermal imaging analogue to fluorescence cross-correlation spectroscopy.

The two techniques we developed to quantify mitochondrial dynamics relied heavily on the high sensitivity and stability of poli-OCM imaging, which allowed us to continuously image AuNP-labeled mitochondria without any loss of contrast. The first technique (1) is based on temporal autocorrelation analysis combined with a classical diffusion model. Autocorrelation analysis is the concept behind fluorescence correlation spectroscopy (FCS); arguably one of the most well-established techniques for quantifying dynamic processes in chemistry and biophysics. In our approach, we extended this analysis to three-dimensional poli-OCM imaging allowing us to extract spatially resolved mitochondria diffusion parameters. We showed three dimensional diffusion parameter maps, which we can use to identify and locate regions inside the cell where there is fast or slow mitochondrial diffusion. The diffusion parameters we measured illustrate the high degree of heterogeneity in the cell with diffusion times spanning over three orders of magnitude (10 to 1.5×10^3 seconds). This characterized the variation in mitochondrial activity within the cell and illustrated the intracellular crowding experienced by a relatively massive organelle. However, the classical diffusion model used with our temporal autocorrelation analysis assumes point-like diffusers. Previous studies in FCS have shown that maintaining this assumption for diffusers with comparable dimensions to the point spread function (PSF) of the instrument results in an overestimation of the measured diffusion time. In the case of the poli-OCM, this is complicated even more by the Bessel-like illumination beam, which results in focal volume with prominent side lobes. We investigated the effect of mitochondria size and the unique shape of the poli-OCM PSF by incorporating them as modification to the molecular detection function. Through simulations we showed that compared

to the ideal assumption of the classical diffusion model, temporal autocorrelation analysis of poli-OCM imaging data resulted to diffusion times that were $\approx 2.4\times$ larger. The MDF modification we implemented can be used to calculate a “correction factor” depending on the system parameters. The second technique (2) we developed exploits the higher localization precision of single particle tracking (SPT). SPT algorithms have demonstrated localization precision well below the size of the PSF, which is of particular significance in quantifying the dynamics of nearly static or slowly diffusing particles like the mitochondria. The high sensitivity and signal stability of poli-OCM imaging is perfect for SPT analysis, which typically requires high signal to noise ratio. Moreover, we demonstrated the possibility of poli-OCM based SPT analysis in identifying and differentiating the transition from diffusive to directional mitochondrial motion. This complex dynamic phenomena is not as straightforwardly addressed with temporal autocorrelation analysis.

The ability to extract spatially resolved diffusion parameters with temporal correlation analysis is well complemented by the accuracy and versatility of single particle tracking. The two techniques we developed work well together in quantifying mitochondrial dynamics and provide researchers with a set of tools that aid in obtaining a more complete understanding of this important cellular phenomenon. Due to their involvement in energy production and ensuring cell health and survival, mitochondrial dysfunction has been implicated with numerous human disorders. Despite many studies linking abnormal mitochondria dynamics to the pathogenesis of these diseases, few have investigated them through imaging and quantification of mitochondrial motion. This is arguably due to the absence of an established technique that allows continuous imaging of the same cell over long time durations while still providing the specificity necessary to study the mitochondria.

In this thesis we also attempted to quantify the mitochondrial dynamics of the Cockayne syndrome (CS). CS is a severe genetic disorder that causes neurodegeneration, developmental deficiencies, premature aging, and death. Currently, mutations in either CSA or CSB gene products are the known causes of CS. We conducted mitochondria specific three-dimensional time-lapse imaging using the poli-OCM on two immortalized cell lines: (1) the diseased CSB-deficient CS1AN-SV and (2) the control CSB-proficient MRC5-SV. We extracted mitochondrial diffusion parameters using the two analysis techniques that we developed. The initial results we presented contained mitochondrial diffusion parameters of four cells from each cell line. Interestingly, the extracted diffusion parameters show that the MRC5-SV cells displayed more variation with their mitochondrial dynamics compared to the CS1AN-SV cells. This was observed in both temporal autocorrelation and single particle tracking analysis. Despite quantifying mitochondrial dynamics, the data we have collected at this point was insufficient to differentiate between the CS1AN-SV and MRC5-SV. However, it is worth noting that this was a pilot study. It was important to establish the viability of the CS cell lines upon exposure to the AuNP labels. We demonstrated incubation of both CS1AN-SV and MRC5-SV with AuNP labels

Chapter 6. Conclusion

for over 5 days without any appreciable difference with the unlabeled control. We were also able to achieve continuous time-lapse poli-OCM imaging for two hours without observing cell death, using 5 mW and 6 mW of photothermal heating and OCM probe beam powers. Furthermore, the quality of the three-dimensional poli-OCM images were sufficient to perform temporal autocorrelation and single particle tracking analyses on the same datasets. These findings convinced us that investigating CS mitochondrial dynamics via poli-OCM imaging is worth pursuing. Evidently, future studies would benefit from collecting a larger data set that would reach statistical significance. Such a study would establish a set of parameters characterizing the impact of CS to mitochondrial dynamics and vice versa. Once achieved, this study could serve as a foundation for investigating the response of CS mitochondrial dynamics to various stimulants including experimental treatment methods. Furthermore, this would be a first step in studying other human diseases that have been associated with mitochondrial dysfunction using the techniques developed in this thesis.

Acknowledgements

This thesis would not have succeeded without the help and support of my family and friends. Thank you all!

First, I would like to express my gratitude to my supervisor Prof. Theo Lasser for giving me the opportunity to work on my thesis at the Laboratoire d'Optique Biomedicale (LOB). This last four years were not easy but his continued support and seemingly, endless optimism helped me get through it. I appreciate all of our discussions; I learned a lot not only about science but also about life. The experience of working under his supervision will stay with me forever.

I also want to thank Prof. Hans Peter Herzig, Prof. Dimitri Van de Ville, Dr. Martin Villiger, and Prof. Tanja Weil for accepting to be part of my thesis committee. Their scrutiny and criticism only made my work better.

I am especially grateful to our collaborators Prof. Tanja Weil and Dr. Sabyasachi Chakraborty. I will not embarrass myself by pretending to understand the chemistry of gold nanoparticle synthesis and functionalization as well as they do. I enjoyed our work together and I am happy our efforts bore fruit; this thesis would not have been possible without their contribution.

A special thanks goes to my post-doc Dr. Jérôme Extermann. He was always very patient and supportive even though I was not the most efficient student. Despite splitting his time between LOB and HEPIA, he was always ready to offer help and did whatever he could to make my situation even just a little bit better. I could always count on him for advice and he guided me through trying times. I appreciate all that he has done for me.

I was also very fortunate to have shared a room with my long-time officemates Dr. Corrine Berclaz and Dr. Daniel Szlag. Perhaps due to my presence, our room was never the tidiest nor the most "professional". I am grateful to them for welcoming me and all my peculiarities, I know it was not easy. Let me also take this opportunity to apologize to Corrine (a.k.a. my office mother). I am sorry for worrying her when I faked collapsing, it's just one of those things people experience having me around.

Acknowledgements

At this point, I would like to acknowledge the rest of my LOB family, all the past and present members whom I had the pleasure to work with. First, all my thanks to our secretaries Fabienne Ubezio and Noelia Simone. Fabienne helped me with my move to Lausanne and my initial integration to the Swiss system. As for Noelia, I cannot even count the number of times I have bothered her even for the simplest of things; I thank her for always being helpful and in good spirit. Life in LOB would not be complete without Mr. Antonio "Tonio the old man of LOB" Lopez. Whenever I feel depressed, hopeless, sleepy, or bored, taking a trip to the Tonio corner of the lab never failed to brighten up my mood. He has always been our reservoir of good mood, loud music, and inexplicable craziness. I am grateful that he was there from beginning to end. I also want to thank Dr. Marcel Leutenegger for always having the perfect answer to whatever microscopy question I ever had. A special mention also goes to the original occupants of BM 5141, Dr. Stefan Geissbühler, Dr. Stephane Broillet, and Dr. Azat Sharipov. They were a quiet bunch but we had our share of fun. I also want to give thanks to Dr. Arno Bouwens who was my original mentor for OCM and still one of the best people I know at explaining scientific concept. I am also grateful to Dr. Tristan Bolmont and Dr. Taoufiq Harach, the biologists of LOB who taught me everything I know about cell culturing and more. To Ms. Arielle Planchette, I feel sad that I can not be there for the rest of her PhD; I am sorry that I have to leave now. Arielle and her interesting friends educated me on British civilization and culture, the memory of her party is forever etched in my mind. Finally, to the current LOB, Dr. Kristin Grussmayer, Dr. Jochem Deen, Dr. Tomas Lukes, and Mr. Adrien Descloux, I hope I left the lab in a more or less acceptable state. Good luck and thank you all!

I would also like to convey my deepest appreciation to all my friends. Out of the many aspects of PhD life in Lausanne, they are the ones that I hold most dear. I cannot put into words how the camaraderie I experienced kept me going and made me feel that things would eventually turn out for the better. I hope they can forgive me for failing to mention each one of them.

I would like to thank my friend and roommate Mr. Orly Tarun. Orly and I have been friends for more or less 12 years now. We have traveled halfway across the world with only our friendship as insurance. It was quite an adventure and I am happy to have taken it with you. I don't know where and what the future will bring us but I wish him and Severine all the best. This now brings me to the next person I want to thank, Orly's new roommate and soon to be better half, Dr. Severine Coquoz. Severine started her PhD more or less at the same time as me. We were colleagues who eventually became good friends. Out of our many interesting conversations, I am not sure if I shocked her more or the other way around. For the next chapters of their life together, I wish Severine and Orly all the luck. I hope they will always remember that the world can be a kind and beautiful place if we make it. In the off chance that the world does fail, they will always have each other (or just blame Orly... that also works). Have fun!

Since she requested, I have to particularly mention and acknowledge Ms. Marie Eve Pascale

Acknowledgements

Didier, one of my very best friends here in Lausanne. I will never forget all the crazy, wild, and intoxicated evenings we shared; it was simply pure unmitigated fun. To this date, Marie still holds the distinction of hosting the best party of 2017. In addition to being the party monger, I am also extremely grateful to her for feeding me specially during my thesis writing days. The cakes she made were so unearthly delicious just one bite felt like being flung into space, launching you to an otherworldly adventure. But above all these, I am thankful to Marie for being an amazing friend! Hopefully this is not the end and we can have more fun in the future.

A special thank you also goes to my boys! Mi compadre Dr. Edgar Emilio Morales Delgado, Dr. Gael Nardin, Mr. Sébastien Walpen, Mr. Vincent Khashayar Shamaei, and Mr. Gabriel Bernasconi. I will no longer elaborate on the things we did during our time together. I am not sure it is safe to put them into writing, much more in my thesis. I do have to say, that over the four years of doing my PhD I needed at least one of them at any given time. I could not ask for a more reliable group of respectable gentlemen to call my friends. The same could be said of the men upholding the spirit and memory of *Atlantis*, Mr. David 'Batista' Nguyen and Mr. Dino 'Augustus' Carpentras. As I begin to accept that life has been slowly pushing us to take different paths, I hope that we may encounter each other once again.

I also want to thank Dr. (or soon to be) Paul Marchand and his wife Linda Mhalla. I wish them a happy one year wedding anniversary. I am sorry if I do not write anything more original this time. The truest and most sincere words I have for them, I already gave for their wedding gift. I know this is a lazy cop out but they know me.

Next I would like to mention the honorable Dr. Amir Nahas, the most French post-doc in LOB. Amir and I enjoyed many moments together despite me not understanding why he was always calling for 20 gods, or wine gods, or vain gods, or whatever he was saying. I hope he does well in Strasbourg and I expect that the next time we see each other he will stop using the excuse of "catching a boat" to escape.

I am also very fortunate to have had the pleasure of being friends with Mr. Alejandro Diaz-Tormo and Ms. Coralie Dessauges. They are definitely two of the nicest people I know and I am happy to have met them during my first year in Lausanne. It is always difficult making friends when you are new to a place but their kindness and sincerity made me feel welcome. They have since moved to other cities and I wish them all the best for their respective PhD's.

Completing my EPFL family, I wish to thank all my friends in LBP, especially Dr. Cornelis Lütgebaucks and Ms. Evangelia Zdrali. I am also grateful to everyone in LAPD and LO, namely Mr. Paul Delrot, Dr. Damien Loterie, Ms. Manon Rostykus, Dr. Timothé Laforest, Dr. Nicolino Stasio, and Dr. Francesca Volpetti. And last but not least, thank you to Kim, Adrien, and all my friends from Satellite!

Acknowledgements

To my friends spread around the world, Dr. Cheryl Abundo, Ms. Alva Presbitero, Dr. Mark Jayson Villangca, Ms. Mary Grace Bato, Ms. Irene Crisologo, and to the rest of the gang left in the Philippines, I treasure how they supported me despite the distance. Thank you for keeping me company even during the wee hours of the night. There are times that our discussions would interfere with work but these were needed distractions. I miss you all and I thank you for being my friends all these years.

Finally, I want to express my love and gratitude to my parents. Despite being separated by continents and oceans from either direction, thousands of kilometers, and unreliable 3rd world internet connection I was never left wanting of the unconditional love and care that only parents can provide. Even when I lost confidence and stopped believing in myself, they never did. Everything I have accomplished, I owe it to them. Thank you!

Lausanne, 20th November 2017

Miguel Sison

Bibliography

- [1] E. Burté, V. Carelli, P. F. Chinnery, and P. Yu-Wai-Man, “Disturbed mitochondrial dynamics and neurodegenerative disorders,” *Nature Reviews Neurology*, vol. 11, pp. 11–24, dec 2014.
- [2] C. GM., “The Mechanism of Oxidative Phosphorylation,” in *The Cell: A Molecular Approach. 2nd edition.*, Sinauer Associates, 2000.
- [3] J. K. Brunelle, E. L. Bell, N. M. Quesada, K. Vercauteren, V. Tiranti, M. Zeviani, R. C. Scarpulla, and N. S. Chandel, “Oxygen sensing requires mitochondrial ROS but not oxidative phosphorylation,” *Cell Metabolism*, vol. 1, pp. 409–414, jun 2005.
- [4] E. L. Bell, B. M. Emerling, and N. S. Chandel, “Mitochondrial regulation of oxygen sensing,” *Mitochondrion*, vol. 5, pp. 322–332, oct 2005.
- [5] D. N. Bowser, T. Minamikawa, P. Nagley, and D. A. Williams, “Role of mitochondria in calcium regulation of spontaneously contracting cardiac muscle cells.,” *Biophysical journal*, vol. 75, pp. 2004–14, oct 1998.
- [6] R. Rizzuto, D. De Stefani, A. Raffaello, and C. Mammucari, “Mitochondria as sensors and regulators of calcium signalling,” *Nature Reviews Molecular Cell Biology*, vol. 13, pp. 566–578, aug 2012.
- [7] L. Contreras, I. Drago, E. Zampese, and T. Pozzan, “Mitochondria: The calcium connection,” *Biochimica et Biophysica Acta - Bioenergetics*, vol. 1797, pp. 607–618, jun 2010.
- [8] D. F. D.-F. Suen, K. L. Norris, and R. J. Youle, “Mitochondrial dynamics and apoptosis,” *Genes and Development*, vol. 22, pp. 1577–1590, jun 2008.
- [9] C. Wang and R. J. Youle, “The Role of Mitochondria in Apoptosis,” *Annual Review of Genetics*, vol. 43, pp. 95–118, dec 2009.
- [10] L. A. Pradelli, M. Bénétou, and J.-E. Ricci, “Mitochondrial control of caspase-dependent and -independent cell death,” *Cellular and Molecular Life Sciences*, vol. 67, pp. 1589–1597, may 2010.

Bibliography

- [11] S. A. Detmer and D. C. Chan, "Functions and dysfunctions of mitochondrial dynamics," *Nature Reviews Molecular Cell Biology*, vol. 8, no. 11, pp. 870–879, 2007.
- [12] C. M. Nasrallah and T. L. Horvath, "Mitochondrial dynamics in the central regulation of metabolism," *Nature Reviews Endocrinology*, vol. 10, pp. 650–658, sep 2014.
- [13] S. L. Archer, "Mitochondrial Dynamics — Mitochondrial Fission and Fusion in Human Diseases," *New England Journal of Medicine*, vol. 369, pp. 2236–2251, dec 2013.
- [14] H. Chen and D. C. Chan, "Mitochondrial dynamics-fusion, fission, movement, and mitophagy-in neurodegenerative diseases," *Human Molecular Genetics*, vol. 18, pp. R169–R176, oct 2009.
- [15] X. Wang, D. Winter, G. Ashrafi, J. Schlehe, Y. L. Wong, D. Selkoe, S. Rice, J. Steen, M. J. Lavoie, and T. L. Schwarz, "PINK1 and Parkin target miro for phosphorylation and degradation to arrest mitochondrial motility," *Cell*, vol. 147, pp. 893–906, nov 2011.
- [16] W. Song, J. Chen, A. Petrilli, G. Liot, E. Klinglmayr, Y. Zhou, P. Poquiz, J. Tjong, M. A. Pouladi, M. R. Hayden, E. Masliah, M. Ellisman, I. Rouiller, R. Schwarzenbacher, B. Bossy, G. Perkins, and E. Bossy-Wetzel, "Mutant huntingtin binds the mitochondrial fission GTPase dynamin-related protein-1 and increases its enzymatic activity," *Nature Medicine*, vol. 17, pp. 377–382, mar 2011.
- [17] M. Corrado, L. Scorrano, and S. Campello, "Mitochondrial dynamics in cancer and neurodegenerative and neuroinflammatory diseases," *International Journal of Cell Biology*, vol. 2012, pp. 1–13, 2012.
- [18] S. T. Hess, T. P. Girirajan, and M. D. Mason, "Ultra-High Resolution Imaging by Fluorescence Photoactivation Localization Microscopy," *Biophysical Journal*, vol. 91, pp. 4258–4272, dec 2006.
- [19] E. Betzig, G. H. Patterson, R. Sougrat, O. W. Lindwasser, S. Olenych, J. S. Bonifacino, M. W. Davidson, J. Lippincott-Schwartz, and H. F. Hess, "Imaging Intracellular Fluorescent Proteins at Nanometer Resolution," *Science*, vol. 313, pp. 1642–1645, sep 2006.
- [20] R. Schmidt, C. A. Wurm, S. Jakobs, J. Engelhardt, A. Egner, and S. W. Hell, "Spherical nanosized focal spot unravels the interior of cells," *Nature Methods*, vol. 5, pp. 539–544, jun 2008.
- [21] D. C. Jans, C. a. Wurm, D. Riedel, D. Wenzel, F. Stagge, M. Deckers, P. Rehling, and S. Jakobs, "STED super-resolution microscopy reveals an array of MINOS clusters along human mitochondria.," *Proceedings of the National Academy of Sciences of the United States of America*, vol. 110, pp. 8936–41, may 2013.

- [22] R. Medda, S. Jakobs, S. W. Hell, and J. Bewersdorf, "4Pi microscopy of quantum dot-labeled cellular structures," *Journal of Structural Biology*, vol. 156, pp. 517–523, dec 2006.
- [23] L. M. Hirvonen, K. Wicker, O. Mandula, and R. Heintzmann, "Structured illumination microscopy of a living cell," *European Biophysics Journal*, vol. 38, pp. 807–812, jul 2009.
- [24] L. Plecitá-Hlavatá, M. Lessard, J. Šantorová, J. Bewersdorf, and P. Ježek, "Mitochondrial oxidative phosphorylation and energetic status are reflected by morphology of mitochondrial network in INS-1E and HEP-G2 cells viewed by 4Pi microscopy," *Biochimica et Biophysica Acta - Bioenergetics*, vol. 1777, pp. 834–846, jul 2008.
- [25] A. Chakraborty and N. R. Jana, "Design and synthesis of triphenylphosphonium functionalized nanoparticle probe for mitochondria targeting and imaging," *Journal of Physical Chemistry C*, vol. 119, pp. 2888–2895, jan 2015.
- [26] E. Fanizza, R. M. Iacobazzi, V. Laquintana, G. Valente, G. Caliandro, M. Striccoli, A. Agostiano, A. Cutrignelli, A. Lopodota, M. L. Curri, M. Franco, N. Depalo, and N. Denora, "Highly selective luminescent nanostructures for mitochondrial imaging and targeting," *Nanoscale*, vol. 8, no. 6, pp. 3350–3361, 2016.
- [27] R. A. Leitgeb, M. Villiger, A. H. Bachmann, L. Steinmann, and T. Lasser, "Extended focus depth for Fourier domain optical coherence microscopy," *Optics Letters*, vol. 31, no. 16, p. 2450, 2006.
- [28] J. Goulley, M. Villiger, C. Berclaz, P. Meda, A. Grapin-Botton, and T. Lasser, "Live in vivo imaging of Langerhans islets in normal and diabetic mice by extended focus optical coherence microscopy," *Diabetologia*, vol. 53, pp. S194–S194, sep 2010.
- [29] M. Villiger, J. Goulley, M. Friedrich, A. Grapin-Botton, P. Meda, T. Lasser, and R. A. Leitgeb, "In vivo imaging of murine endocrine islets of Langerhans with extended-focus optical coherence microscopy," *Diabetologia*, vol. 52, pp. 1599–1607, aug 2009.
- [30] M. Villiger, J. Goulley, and T. Lasser, "Towards High Resolution Optical Imaging of Beta Cells In Vivo," *CURRENT PHARMACEUTICAL DESIGN*, vol. 16, pp. 1595–1608, may 2010.
- [31] C. Berclaz, J. Goulley, M. Villiger, C. Pache, A. Bouwens, E. Martin-Williams, D. Van de Ville, A. C. Davison, A. Grapin-Botton, and T. Lasser, "Diabetes imaging—quantitative assessment of islets of Langerhans distribution in murine pancreas using extended-focus optical coherence microscopy," *Biomedical Optics Express*, vol. 3, p. 1365, jun 2012.
- [32] C. Berclaz, C. Pache, A. Bouwens, D. Szlag, A. Lopez, L. Joosten, S. Ekim, M. Brom, M. Gotthardt, A. Grapin-Botton, and T. Lasser, "Combined Optical Coherence and

Bibliography

- Fluorescence Microscopy to assess dynamics and specificity of pancreatic beta-cell tracers,” *Scientific Reports*, vol. 5, p. 10385, sep 2015.
- [33] T. Bolmont, A. Bouwens, C. Pache, M. Dimitrov, C. Berclaz, M. Villiger, B. M. Wegenast-Braun, T. Lasser, and P. C. Fraering, “Label-Free Imaging of Cerebral α -Amyloidosis with Extended-Focus Optical Coherence Microscopy,” *Journal of Neuroscience*, vol. 32, pp. 14548–14556, oct 2012.
- [34] M. Villiger, C. Pache, and T. Lasser, “Dark-field optical coherence microscopy,” *Optics Letters*, vol. 35, p. 3489, oct 2010.
- [35] P. J. Marchand, A. Bouwens, D. Szlag, D. Nguyen, A. Descloux, M. Sison, S. Coquoz, J. Extermann, and T. Lasser, “Visible spectrum extended-focus optical coherence microscopy for label-free sub-cellular tomography,” *Biomedical Optics Express*, vol. 8, p. 3343, jul 2017.
- [36] D. Magde, E. Elson, and W. W. Webb, “Thermodynamic fluctuations in a reacting system measurement by fluorescence correlation spectroscopy,” *Physical Review Letters*, vol. 29, no. 11, pp. 705–708, 1972.
- [37] M. D. Aamann, M. M. Sorensen, C. Hvitby, B. R. Berquist, M. Muftuoglu, J. Tian, N. C. de Souza-Pinto, M. Scheibye-Knudsen, D. M. Wilson, T. Stevnsner, and V. A. Bohr, “Cockayne syndrome group B protein promotes mitochondrial DNA stability by supporting the DNA repair association with the mitochondrial membrane,” *The FASEB Journal*, vol. 24, pp. 2334–2346, jul 2010.
- [38] J. E. Cleaver, A. M. Brennan-Minnella, R. A. Swanson, K.-w. Fong, J. Chen, K.-m. Chou, Y.-w. Chen, I. Revet, and V. Bezrookove, “Mitochondrial reactive oxygen species are scavenged by Cockayne syndrome B protein in human fibroblasts without nuclear DNA damage,” *Proceedings of the National Academy of Sciences of the United States of America*, vol. 111, pp. 13487–92, sep 2014.
- [39] L. Chatre, D. S. F. Biard, A. Sarasin, and M. Ricchetti, “Reversal of mitochondrial defects with CSB-dependent serine protease inhibitors in patient cells of the progeroid Cockayne syndrome,” *Proceedings of the National Academy of Sciences*, vol. 112, pp. E2910–E2919, jun 2015.
- [40] W. M. Saxton and P. J. Hollenbeck, “The axonal transport of mitochondria,” *Journal of Cell Science*, vol. 125, pp. 2095–2104, dec 2012.
- [41] P. Mishra, V. Carelli, G. Manfredi, and D. Chan, “Proteolytic Cleavage of Opa1 Stimulates Mitochondrial Inner Membrane Fusion and Couples Fusion to Oxidative Phosphorylation,” *Cell Metabolism*, vol. 19, pp. 630–641, apr 2014.

- [42] R. J. Youle and A. M. van der Bliek, "Mitochondrial Fission, Fusion, and Stress," *Science*, vol. 337, pp. 1062–1065, aug 2012.
- [43] M. J. Berridge, M. D. Bootman, and H. L. Roderick, "Calcium: Calcium signalling: dynamics, homeostasis and remodelling," *Nature Reviews Molecular Cell Biology*, vol. 4, pp. 517–529, jul 2003.
- [44] P. Pinton, C. Giorgi, R. Siviero, E. Zecchini, and R. Rizzuto, "Calcium and apoptosis: ER-mitochondria Ca²⁺ transfer in the control of apoptosis," *Oncogene*, vol. 27, pp. 6407–18, oct 2008.
- [45] F. M. P. Tonelli, A. K. Santos, D. A. Gomes, S. L. da Silva, K. N. Gomes, L. O. Ladeira, and R. R. Resende, "Stem Cells and Calcium Signaling," pp. 891–916, Springer, Dordrecht, 2012.
- [46] S. Pillai, D. D. Bikle, M.-L. Mancianti, P. Cline, and M. Hincenbergs, "Calcium regulation of growth and differentiation of normal human keratinocytes: Modulation of differentiation competence by stages of growth and extracellular calcium," *Journal of Cellular Physiology*, vol. 143, pp. 294–302, may 1990.
- [47] U. De Marchi, J. Thevenet, A. Hermant, E. Dioum, and A. Wiederkehr, "Calcium co-regulates oxidative metabolism and ATP synthase-dependent respiration in pancreatic beta cells.," *The Journal of biological chemistry*, vol. 289, pp. 9182–94, mar 2014.
- [48] K. Nakayama, "Cellular Signal Transduction of the Hypoxia Response," *Journal of Biochemistry*, vol. 146, pp. 757–765, dec 2009.
- [49] N. S. Chandel, E. Maltepe, E. Goldwasser, C. E. Mathieu, M. C. Simon, and P. T. Schumacker, "Mitochondrial reactive oxygen species trigger hypoxia-induced transcription," *Cell Biology*, vol. 95, pp. 11715–11720, 1998.
- [50] R. B. Hamanaka and N. S. Chandel, "Mitochondrial reactive oxygen species regulate hypoxic signaling.," *Current opinion in cell biology*, vol. 21, pp. 894–9, dec 2009.
- [51] V. Parra, R. Bravo-Sagua, I. Norambuena-Soto, C. P. Hernández-Fuentes, A. G. Gómez-Contreras, H. E. Verdejo, R. Mellado, M. Chiong, S. Lavandero, and P. F. Castro, "Inhibition of mitochondrial fission prevents hypoxia-induced metabolic shift and cellular proliferation of pulmonary arterial smooth muscle cells," *Biochimica et Biophysica Acta (BBA) - Molecular Basis of Disease*, jul 2017.
- [52] A. M. Tolkovsky, "Mitophagy," *Biochimica et Biophysica Acta (BBA) - Molecular Cell Research*, vol. 1793, pp. 1508–1515, sep 2009.
- [53] F. R. Jornayvaz and G. I. Shulman, "Regulation of mitochondrial biogenesis.," *Essays in biochemistry*, vol. 47, pp. 69–84, 2010.

Bibliography

- [54] J. J. Ryan, G. Marsboom, Y.-H. Fang, P. T. Toth, E. Morrow, N. Luo, L. Piao, Z. Hong, K. Ericson, H. J. Zhang, M. Han, C. R. Haney, C.-T. Chen, W. W. Sharp, and S. L. Archer, "PGC1 α -mediated Mitofusin-2 Deficiency in Female Rats and Humans with Pulmonary Arterial Hypertension," *American Journal of Respiratory and Critical Care Medicine*, vol. 187, pp. 865–878, apr 2013.
- [55] D. Hanahan and R. A. Weinberg, "Hallmarks of cancer: The next generation," *Cell*, vol. 144, pp. 646–674, mar 2011.
- [56] J. Lopez and S. W. G. Tait, "Mitochondrial apoptosis: killing cancer using the enemy within," *British Journal of Cancer*, vol. 112, pp. 957–962, mar 2015.
- [57] J. Rehman, H. J. Zhang, P. T. Toth, Y. Zhang, G. Marsboom, Z. Hong, R. Salgia, A. N. Husain, C. Wietholt, and S. L. Archer, "Inhibition of mitochondrial fission prevents cell cycle progression in lung cancer," *The FASEB Journal*, vol. 26, pp. 2175–2186, may 2012.
- [58] A. Ferreira-da Silva, C. Valacca, E. Rios, H. Pópulo, P. Soares, M. Sobrinho-Simões, L. Scorrano, V. Máximo, and S. Campello, "Mitochondrial dynamics protein Drp1 is overexpressed in oncocytic thyroid tumors and regulates cancer cell migration," *PLoS ONE*, vol. 10, no. 3, p. e0122308, 2015.
- [59] O. Warburg, "On the Origin of Cancer Cells," *Science*, vol. 123, pp. 309–314, feb 1956.
- [60] M. V. Liberti and J. W. Locasale, "The Warburg Effect: How Does it Benefit Cancer Cells?," *Trends in Biochemical Sciences*, vol. 41, pp. 211–218, mar 2016.
- [61] T. Pfeiffer, S. Schuster, and S. Bonhoeffer, "Cooperation and Competition in the Evolution of ATP-Producing Pathways," *Science*, vol. 292, pp. 504–507, apr 2001.
- [62] J. Zheng, "Energy metabolism of cancer: Glycolysis versus oxidative phosphorylation (Review).," *Oncology letters*, vol. 4, pp. 1151–1157, dec 2012.
- [63] A. P. Trotta and J. E. Chipuk, "Mitochondrial dynamics as regulators of cancer biology," *Cellular and Molecular Life Sciences*, vol. 74, pp. 1999–2017, jun 2017.
- [64] E. Alirol and J. C. Martinou, "Mitochondria and cancer: is there a morphological connection?," *Oncogene*, vol. 25, pp. 4706–4716, aug 2006.
- [65] S. Y. Wieder, M. N. Serasinghe, J. C. Sung, D. C. Choi, M. B. Birge, J. L. Yao, E. Bernstein, J. T. Celebi, and J. E. Chipuk, "Activation of the Mitochondrial Fragmentation Protein DRP1 Correlates with BRAF(V600E) Melanoma.," *The Journal of investigative dermatology*, vol. 135, pp. 2544–2547, oct 2015.

- [66] A. Ferreira-da Silva, C. Valacca, E. Rios, H. Pópulo, P. Soares, M. Sobrinho-Simões, L. Scorrano, V. Máximo, and S. Campello, "Mitochondrial Dynamics Protein Drp1 Is Overexpressed in Oncocytic Thyroid Tumors and Regulates Cancer Cell Migration," *PLOS ONE*, vol. 10, p. e0122308, mar 2015.
- [67] P. Zou, L. Liu, L. D. Zheng, K. K. Payne, M. H. Manjili, M. O. Idowu, J. Zhang, E. M. Schmelz, and Z. Cheng, "Coordinated Upregulation of Mitochondrial Biogenesis and Autophagy in Breast Cancer Cells: The Role of Dynamin Related Protein-1 and Implication for Breast Cancer Treatment," *Oxidative Medicine and Cellular Longevity*, vol. 2016, pp. 1–10, sep 2016.
- [68] G. E. Zhang, H. L. Jin, X. K. Lin, C. Chen, X. S. Liu, Q. Zhang, and J. R. Yu, "Anti-tumor effects of Mfn2 in gastric cancer," *International journal of molecular sciences*, vol. 14, pp. 13005–13021, jun 2013.
- [69] X. Zhao, C. Tian, W. M. Puszyk, O. O. Ogunwobi, M. Cao, T. Wang, R. Cabrera, D. R. Nelson, and C. Liu, "OPA1 downregulation is involved in sorafenib-induced apoptosis in hepatocellular carcinoma," *Laboratory Investigation*, vol. 93, pp. 8–19, jan 2013.
- [70] C. Jose, N. Bellance, and R. Rossignol, "Choosing between glycolysis and oxidative phosphorylation: A tumor's dilemma?," *Biochimica et Biophysica Acta - Bioenergetics*, vol. 1807, pp. 552–561, jun 2011.
- [71] F. Palau, A. Estela, D. Pla-Martín, and M. Sánchez-Piris, "The role of mitochondrial network dynamics in the pathogenesis of charcot-marie-tooth disease," in *Advances in Experimental Medicine and Biology*, vol. 652, pp. 129–137, Springer, Dordrecht, 2009.
- [72] M. V. Alavi and N. Fuhrmann, "Dominant optic atrophy, OPA1, and mitochondrial quality control: understanding mitochondrial network dynamics," *Molecular Neurodegeneration*, vol. 8, p. 32, sep 2013.
- [73] A. Johri and M. F. Beal, "Mitochondrial Dysfunction in Neurodegenerative Diseases," *Journal of Pharmacology and Experimental Therapeutics*, vol. 342, pp. 619–630, sep 2012.
- [74] R. K. Chaturvedi, P. Adhietty, S. Shukla, T. Hennessy, N. Calingasan, L. Yang, A. Starkov, M. Kiaei, M. Cannella, J. Sassone, A. Ciammola, F. Squitieri, and M. F. Beal, "Impaired PGC-1 α function in muscle in Huntington's disease," *Human Molecular Genetics*, vol. 18, pp. 3048–3065, aug 2009.
- [75] A. Johri, A. Chandra, and M. F. Beal, "PGC-1 α , mitochondrial dysfunction, and Huntington's disease," *Free Radical Biology and Medicine*, vol. 62, pp. 37–46, sep 2013.
- [76] J. Kim, J. P. Moody, C. K. Edgerly, O. L. Bordiuk, K. Cormier, K. Smith, M. Flint Beal, and R. J. Ferrante, "Mitochondrial loss, dysfunction and altered dynamics in Huntington's disease," *Human Molecular Genetics*, vol. 19, no. 20, pp. 3919–3935, 2010.

Bibliography

- [77] E. Bossy-Wetzels, A. Petrilli, and A. B. Knott, "Mutant huntingtin and mitochondrial dysfunction.," *Trends in neurosciences*, vol. 31, pp. 609–16, dec 2008.
- [78] X. Wang, W. Wang, L. Li, G. Perry, H. gon Lee, and X. Zhu, "Oxidative stress and mitochondrial dysfunction in Alzheimer's disease," *Biochimica et Biophysica Acta - Molecular Basis of Disease*, vol. 1842, pp. 1240–1247, aug 2014.
- [79] E. Trushina, E. Nemutlu, S. Zhang, T. Christensen, J. Camp, J. Mesa, A. Siddiqui, Y. Tamura, H. Sesaki, T. M. Wengenack, P. P. Dzeja, and J. F. Poduslo, "Defects in mitochondrial dynamics and metabolomic signatures of evolving energetic stress in mouse models of familial alzheimer's disease," *PLoS ONE*, vol. 7, p. e32737, feb 2012.
- [80] W. Martinet, G. R. Y. De Meyer, A. G. Herman, and M. M. Kockx, "Reactive oxygen species induce RNA damage in human atherosclerosis," *European Journal of Clinical Investigation*, vol. 34, pp. 323–327, may 2004.
- [81] T. Hemnani and M. S. Parihar, "Reactive oxygen species and oxidative DNA damage," *Indian Journal of Physiology and Pharmacology*, vol. 42, pp. 440–452, oct 1998.
- [82] H.-J. Lee, F. Khoshaghideh, S. Lee, and S.-J. Lee, "Impairment of microtubule-dependent trafficking by overexpression of α -synuclein," *European Journal of Neuroscience*, vol. 24, pp. 3153–3162, dec 2006.
- [83] E. M. Valente, "Hereditary Early-Onset Parkinson's Disease Caused by Mutations in PINK1," *Science*, vol. 304, pp. 1158–1160, may 2004.
- [84] S. Liu, T. Sawada, S. Lee, W. Yu, G. Silverio, P. Alapatt, I. Millan, A. Shen, W. Saxton, T. Kanao, R. Takahashi, N. Hattori, Y. Imai, and B. Lu, "Parkinson's disease-associated kinase PINK1 regulates miro protein level and axonal transport of mitochondria," *PLoS Genetics*, vol. 8, p. e1002537, mar 2012.
- [85] Y. Yang, S. Gehrke, Y. Imai, Z. Huang, Y. Ouyang, J.-W. Wang, L. Yang, M. F. Beal, H. Vogel, and B. Lu, "Mitochondrial pathology and muscle and dopaminergic neuron degeneration caused by inactivation of Drosophila Pink1 is rescued by Parkin.," *Proceedings of the National Academy of Sciences of the United States of America*, vol. 103, pp. 10793–8, jul 2006.
- [86] J. Park, S. B. Lee, S. Lee, Y. Kim, S. Song, S. Kim, E. Bae, J. Kim, M. Shong, J.-M. Kim, and J. Chung, "Mitochondrial dysfunction in Drosophila PINK1 mutants is complemented by parkin," *Nature*, vol. 441, pp. 1157–1161, jun 2006.
- [87] A. Rakovic, A. Grünwald, J. Kottwitz, N. Brüggemann, P. P. Pramstaller, K. Lohmann, and C. Klein, "Mutations in PINK1 and Parkin impair ubiquitination of Mitofusins in human fibroblasts," *PLoS ONE*, vol. 6, p. e16746, mar 2011.

- [88] A. K. Lutz, N. Exner, M. E. Fett, J. S. Schlehe, K. Kloos, K. Lämmermann, B. Brunner, A. Kurz-Drexler, F. Vogel, A. S. Reichert, L. Bouman, D. Vogt-Weisenhorn, W. Wurst, J. Tatzelt, C. Haass, and K. F. Winklhofer, "Loss of parkin or PINK1 function increases Drp1-dependent mitochondrial fragmentation.," *The Journal of biological chemistry*, vol. 284, pp. 22938–51, aug 2009.
- [89] R. K. Dagda, S. J. Cherra, S. M. Kulich, A. Tandon, D. Park, and C. T. Chu, "Loss of PINK1 function promotes mitophagy through effects on oxidative stress and mitochondrial fission.," *The Journal of biological chemistry*, vol. 284, pp. 13843–55, may 2009.
- [90] N. Exner, B. Treske, D. Paquet, K. Holmström, C. Schiesling, S. Gispert, I. Carballo-Carbajal, D. Berg, H.-H. Hoepken, T. Gasser, R. Krüger, K. F. Winklhofer, F. Vogel, A. S. Reichert, G. Auburger, P. J. Kahle, B. Schmid, and C. Haass, "Loss-of-function of human PINK1 results in mitochondrial pathology and can be rescued by parkin.," *The Journal of neuroscience : the official journal of the Society for Neuroscience*, vol. 27, pp. 12413–8, nov 2007.
- [91] Y. Yang, Y. Ouyang, L. Yang, M. F. Beal, A. McQuibban, H. Vogel, and B. Lu, "Pink1 regulates mitochondrial dynamics through interaction with the fission/fusion machinery," *Proceedings of the National Academy of Sciences*, vol. 105, pp. 7070–7075, may 2008.
- [92] B. E. A. Saleh and M. C. Teich, *Statistical Optics*, pp. 342–383. John Wiley & Sons, Inc., 2001.
- [93] A. F. F. Lasser, W. Drexler, C. K. Hitzenberger, and T. "Optical coherence tomography - principles and applications," *Reports on Progress in Physics*, vol. 66, p. 239, feb 2003.
- [94] A. F. Fercher, C. K. Hitzenberger, G. Kamp, and S. Y. El-Zaiat, "Measurement of intraocular distances by backscattering spectral interferometry," *Optics Communications*, vol. 117, pp. 43–48, may 1995.
- [95] A. Bouwens, T. Bolmont, D. Szlag, C. Berclaz, and T. Lasser, "Quantitative cerebral blood flow imaging with extended-focus optical coherence microscopy," *Optics Letters*, vol. 39, p. 37, jan 2014.
- [96] A. Bouwens, D. Szlag, M. Szkulmowski, T. Bolmont, M. Wojtkowski, and T. Lasser, "Quantitative lateral and axial flow imaging with optical coherence microscopy and tomography," *Optics Express*, vol. 21, p. 17711, jul 2013.
- [97] P. J. Marchand, A. Bouwens, T. Bolmont, V. K. Shamaei, D. Nguyen, D. Szlag, J. Extermann, and T. Lasser, "Statistical parametric mapping of stimuli evoked changes in total blood flow velocity in the mouse cortex obtained with extended-focus optical coherence microscopy," *Biomed. Opt. Express*, vol. 8, pp. 1–15, jan 2017.

Bibliography

- [98] S. Berciaud, D. Lasne, G. A. Blab, L. Cognet, and B. Lounis, "Photothermal heterodyne imaging of individual metallic nanoparticles: Theory versus experiment," *Physical Review B - Condensed Matter and Materials Physics*, vol. 73, p. 045424, jan 2006.
- [99] A. Gaiduk, P. V. Ruijgrok, M. Yorulmaz, and M. Orrit, "Detection limits in photothermal microscopy," *Chemical Science*, vol. 1, p. 343, aug 2010.
- [100] C. Pache, N. L. Bocchio, A. Bouwens, M. Villiger, C. Berclaz, J. Goulley, M. I. Gibson, C. Santschi, and T. Lasser, "Fast three-dimensional imaging of gold nanoparticles in living cells with photothermal optical lock-in Optical Coherence Microscopy," *Optics Express*, vol. 20, p. 21385, sep 2012.
- [101] T. K. Sau and D. V. Goia, *Biomedical Applications of Gold Nanoparticles*, pp. 101–145. Boston, MA: Springer US, 2012.
- [102] E. E. Connor, J. Mwamuka, A. Gole, C. J. Murphy, and M. D. Wyatt, "Gold nanoparticles are taken up by human cells but do not cause acute cytotoxicity," *Small*, vol. 1, pp. 325–327, mar 2005.
- [103] G. Oberdörster, V. Stone, and K. Donaldson, "Toxicology of nanoparticles: A historical perspective," *Nanotoxicology*, vol. 1, pp. 2–25, jan 2007.
- [104] J. M. Pitarke, V. M. Silkin, E. V. Chulkov, and P. M. Echenique, "Theory of surface plasmons and surface-plasmon polaritons," *Reports on Progress in Physics*, vol. 70, pp. 1–87, jan 2007.
- [105] V. Amendola, R. Pilot, M. Frasconi, O. M. Maragò, and M. A. Iatì, "Surface plasmon resonance in gold nanoparticles: a review," *Journal of Physics: Condensed Matter*, vol. 29, p. 203002, may 2017.
- [106] S. Laing, L. E. Jamieson, K. Faulds, and D. Graham, "Surface-enhanced Raman spectroscopy for in vivo biosensing," *Nature Reviews Chemistry*, vol. 1, p. 0060, aug 2017.
- [107] L. Cognet and B. Lounis, "Ultra-sensitive detection of individual gold nanoparticles : spectroscopy and applications to biology," *Gold Bulletin*, vol. 41, pp. 139–146, jun 2008.
- [108] H. H. Richardson, Z. N. Hickman, A. O. Govorov, A. C. Thomas, W. Zhang, and M. E. Kordesch, "Thermo-optical properties of gold nanoparticles embedded in ice: Characterization of heat generation and melting," *Nano Letters*, vol. 6, no. 4, pp. 783–788, 2006.
- [109] A. O. Govorov and H. H. Richardson, "Generating heat with metal nanoparticles," *Nano Today*, vol. 2, pp. 30–38, feb 2007.

- [110] C. J. Orendorff, T. K. Sau, and C. J. Murphy, "Shape-dependent plasmon-resonant gold nanoparticles," *Small*, vol. 2, pp. 636–639, may 2006.
- [111] H. P. Liang, L. J. Wan, C. L. Bai, and L. Jiang, "Gold hollow nanospheres: Tunable surface plasmon resonance controlled by interior-cavity sizes," *Journal of Physical Chemistry B*, vol. 109, no. 16, pp. 7795–7800, 2005.
- [112] P. K. Jain, K. S. Lee, I. H. El-Sayed, and M. A. El-Sayed, "Calculated absorption and scattering properties of gold nanoparticles of different size, shape, and composition: Applications in biological imaging and biomedicine," *Journal of Physical Chemistry B*, vol. 110, no. 14, pp. 7238–7248, 2006.
- [113] N. S. Abadeer and C. J. Murphy, "Recent Progress in Cancer Thermal Therapy Using Gold Nanoparticles," *The Journal of Physical Chemistry C*, vol. 120, pp. 4691–4716, mar 2016.
- [114] R. S. Riley and E. S. Day, "Gold nanoparticle-mediated photothermal therapy: applications and opportunities for multimodal cancer treatment," *Wiley Interdisciplinary Reviews: Nanomedicine and Nanobiotechnology*, vol. 9, p. e1449, jul 2017.
- [115] S. M. Shawky, A. M. Awad, W. Allam, M. H. Alkordi, and S. F. EL-Khamisy, "Gold aggregating gold: A novel nanoparticle biosensor approach for the direct quantification of hepatitis C virus RNA in clinical samples," *Biosensors and Bioelectronics*, vol. 92, pp. 349–356, jun 2017.
- [116] E. Hutter and D. Maysinger, "Gold-nanoparticle-based biosensors for detection of enzyme activity," *Trends in Pharmacological Sciences*, vol. 34, pp. 497–507, sep 2013.
- [117] C. C. You, M. De, G. Han, and V. M. Rotello, "Tunable inhibition and denaturation of α -chymotrypsin with amino acid-functionalized gold nanoparticles," *Journal of the American Chemical Society*, vol. 127, no. 37, pp. 12873–12881, 2005.
- [118] G. Han, C. T. Martin, and V. M. Rotello, "Stability of gold nanoparticle-bound DNA toward biological, physical, and chemical agents," *Chemical Biology and Drug Design*, vol. 67, pp. 78–82, jan 2006.
- [119] C. X. Zhang, Y. Zhang, X. Wang, Z. M. Tang, and Z. H. Lu, "Hyper-Rayleigh scattering of protein-modified gold nanoparticles," *Analytical Biochemistry*, vol. 320, pp. 136–140, sep 2003.
- [120] Y. Wu, G. Pramanik, K. Eisele, and T. Weil, "Convenient approach to polypeptide copolymers derived from native proteins," *Biomacromolecules*, vol. 13, pp. 1890–1898, jun 2012.

Bibliography

- [121] Y. Wu, K. Eisele, M. Doroshenko, G. Algara-Siller, U. Kaiser, K. Koynov, and T. Weil, "A Quantum Dot Photoswitch for DNA Detection, Gene Transfection, and Live-Cell Imaging," *Small*, vol. 8, pp. 3465–3475, nov 2012.
- [122] S. El-Andaloussi, P. Järver, H. J. Johansson, and U. Langel, "Cargo-dependent cytotoxicity and delivery efficacy of cell-penetrating peptides: a comparative study," *The Biochemical journal*, vol. 407, pp. 285–92, oct 2007.
- [123] S. V. Boddapati, P. Tongcharoensirikul, R. N. Hanson, G. G. M. D'Souza, V. P. Torchilin, and V. Weissig, "Mitochondriotropic Liposomes," *Journal of Liposome Research*, vol. 15, pp. 49–58, jan 2005.
- [124] S. Chakraborty, M. Sison, Y. Wu, A. Ladenburger, G. Pramanik, J. Biskupek, J. Extermann, U. Kaiser, T. Lasser, and T. Weil, "NIR-emitting and photo-thermal active nanogold as mitochondria-specific probes," *Biomater. Sci.*, vol. 5, no. 5, pp. 966–971, 2017.
- [125] K. H. Su, Q. H. Wei, X. Zhang, J. J. Mock, D. R. Smith, and S. Schultz, "Interparticle coupling effects on plasmon resonances of nanogold particles," *Nano Letters*, vol. 3, no. 8, pp. 1087–1090, 2003.
- [126] L. Wang, J. Li, S. Song, D. Li, and C. Fan, "Biomolecular sensing via coupling DNA-based recognition with gold nanoparticles," *Journal of Physics D: Applied Physics*, vol. 42, p. 203001, oct 2009.
- [127] W. Liu, B. Naydenov, S. Chakraborty, B. Wuensch, K. Hübner, S. Ritz, H. Cölfen, H. Barth, K. Koynov, H. Qi, R. Leiter, R. Reuter, J. Wrachtrup, F. Boldt, J. Scheuer, U. Kaiser, M. Sison, T. Lasser, P. Tinnefeld, F. Jelezko, P. Walther, Y. Wu, and T. Weil, "Fluorescent Nanodiamond-Gold Hybrid Particles for Multimodal Optical and Electron Microscopy Cellular Imaging," *Nano Letters*, vol. 16, no. 10, pp. 6236–6244, 2016.
- [128] Y. Tian, M. M. Martinez, and D. Pappas, "Fluorescence correlation spectroscopy: A review of biochemical and microfluidic applications," *Applied Spectroscopy*, vol. 65, pp. 115A–124A, apr 2011.
- [129] R. R. Widengren and J., "Ultrasensitive detection of single molecules by fluorescence correlation spectroscopy," *BioScience*, pp. 180–183, 1990.
- [130] T. Dertinger, V. Pacheco, I. Von Der Hocht, R. Hartmann, I. Gregor, and J. Enderlein, "Two-focus fluorescence correlation spectroscopy: A new tool for accurate and absolute diffusion measurements," *ChemPhysChem*, vol. 8, pp. 433–443, feb 2007.
- [131] P. Schwille, F. Meyer-Almes, and R. Rigler, "Dual-color fluorescence cross-correlation spectroscopy for multicomponent diffusional analysis in solution," *Biophysical Journal*, vol. 72, pp. 1878–1886, apr 1997.

- [132] S. Manley, J. M. Gillette, G. H. Patterson, H. Shroff, H. F. Hess, E. Betzig, and J. Lippincott-Schwartz, "High-density mapping of single-molecule trajectories with photoactivated localization microscopy," *Nature Methods*, vol. 5, pp. 155–157, feb 2008.
- [133] P. N. Hedde, R. M. Dörlich, R. Blomley, D. Gradl, E. Oppong, A. C. Cato, and G. U. Nienhaus, "Stimulated emission depletion-based raster image correlation spectroscopy reveals biomolecular dynamics in live cells," *Nature Communications*, vol. 4, p. 2093, jun 2013.
- [134] F. Göttfert, C. A. Wurm, V. Mueller, S. Berning, V. C. Cordes, A. Honigmann, and S. W. Hell, "Coaligned dual-channel STED nanoscopy and molecular diffusion analysis at 20 nm resolution," *Biophysical Journal*, vol. 105, pp. L01–L03, jul 2013.
- [135] P. W. Wiseman, "Spatial mapping of integrin interactions and dynamics during cell migration by Image Correlation Microscopy," *Journal of Cell Science*, vol. 117, pp. 5521–5534, nov 2004.
- [136] Z.-H. Sheng and Q. Cai, "Mitochondrial transport in neurons: impact on synaptic homeostasis and neurodegeneration," *Nature Reviews Neuroscience*, vol. 13, no. 2, pp. 77–93, 2012.
- [137] D. C. Chan, "Mitochondria: Dynamic Organelles in Disease, Aging, and Development," *Cell*, vol. 125, pp. 1241–1252, jun 2006.
- [138] K. J. Barnham, C. L. Masters, and A. I. Bush, "Neurodegenerative diseases and oxidative stress," *Nature Reviews Drug Discovery*, vol. 3, pp. 205–214, mar 2004.
- [139] M. T. Lin and M. F. Beal, "Mitochondrial dysfunction and oxidative stress in neurodegenerative diseases," *Nature*, vol. 443, pp. 787–795, oct 2006.
- [140] T. A. Planchon, L. Gao, D. E. Milkie, M. W. Davidson, J. A. Galbraith, C. G. Galbraith, and E. Betzig, "Rapid three-dimensional isotropic imaging of living cells using Bessel beam plane illumination," *Nature Methods*, vol. 8, pp. 417–423, may 2011.
- [141] B.-C. Chen, W. R. Legant, K. Wang, L. Shao, D. E. Milkie, M. W. Davidson, C. Janetopoulos, X. S. Wu, J. A. Hammer, Z. Liu, B. P. English, Y. Mimori-Kiyosue, D. P. Romero, A. T. Ritter, J. Lippincott-Schwartz, L. Fritz-Laylin, R. D. Mullins, D. M. Mitchell, J. N. Bembenek, A.-C. Reymann, R. Bohme, S. W. Grill, J. T. Wang, G. Seydoux, U. S. Tulu, D. P. Kiehart, and E. Betzig, "Lattice light-sheet microscopy: Imaging molecules to embryos at high spatiotemporal resolution," *Science*, vol. 346, no. 6208, pp. 1257998–1257998, 2014.
- [142] E. Boisselier and D. Astruc, "Gold nanoparticles in nanomedicine: preparations, imaging, diagnostics, therapies and toxicity," *Chemical Society Reviews*, vol. 38, no. 6, p. 1759, 2009.

Bibliography

- [143] Y. Wu, A. Ermakova, W. Liu, G. Pramanik, T. M. Vu, A. Kurz, L. McGuinness, B. Naydenov, S. Hafner, R. Reuter, J. Wrachtrup, J. Isoya, C. Förtsch, H. Barth, T. Simmet, F. Jelezko, and T. Weil, "Programmable Biopolymers for Advancing Biomedical Applications of Fluorescent Nanodiamonds," *Advanced Functional Materials*, vol. 25, no. 42, pp. 6576–6585, 2015.
- [144] Y. Wu, S. Ihme, M. Feuring-Buske, S. L. Kuan, K. Eisele, M. Lamla, Y. Wang, C. Buske, and T. Weil, "A core-shell albumin copolymer nanotransporter for high capacity loading and two-step release of doxorubicin with enhanced anti-leukemia activity," *Advanced Healthcare Materials*, vol. 2, pp. 884–894, jun 2013.
- [145] K. Eisele, R. A. Gropeanu, C. M. Zehendner, A. Rouhanipour, A. Ramanathan, G. Mihov, K. Koynov, C. R. Kuhlmann, S. G. Vasudevan, H. J. Luhmann, and T. Weil, "Fine-tuning DNA/albumin polyelectrolyte interactions to produce the efficient transfection agent cBSA-147," *Biomaterials*, vol. 31, no. 33, pp. 8789–8801, 2010.
- [146] P. K. Vayalil, J. Y. Oh, F. Zhou, A. R. Diers, M. R. Smith, H. Goltzarian, P. G. Oliver, R. A. Smith, M. P. Murphy, S. E. Velu, and A. Landar, "A novel class of mitochondria-targeted soft electrophiles modifies mitochondrial proteins and inhibits mitochondrial metabolism in breast cancer cells through redox mechanisms," *PLoS ONE*, vol. 10, no. 3, 2015.
- [147] A. C. Sabuncu, J. Grubbs, S. Qian, T. M. Abdel-Fattah, M. W. Stacey, and A. Beskok, "Probing nanoparticle interactions in cell culture media," *Colloids and Surfaces B: Biointerfaces*, vol. 95, pp. 96–102, 2012.
- [148] N. O. Petersen, P. L. Hoddellius, P. W. Wiseman, O. Seger, and K. E. Magnusson, "Quantitation of Membrane-Receptor Distributions by Image Correlation Spectroscopy - Concept and Application," *Biophysical Journal*, vol. 65, no. 3, pp. 1135–1146, 1993.
- [149] P. W. Wiseman, J. A. Squier, M. H. Ellisman, and K. R. Wilson, "Two-photo image correlation spectroscopy and image cross-correlation spectroscopy," *Journal of Microscopy*, vol. 200, pp. 14–25, oct 2000.
- [150] P. M. R. Paulo, A. Gaiduk, F. Kulzer, S. F. G. Krens, H. P. Spaink, T. Schmidt, and M. Orrit, "Photothermal Correlation Spectroscopy of Gold Nanoparticles in Solution †," *Journal of Physical Chemistry C*, vol. 113, no. 27, pp. 11451–11457, 2009.
- [151] V. Octeau, L. Cognet, L. Duchesne, D. Lasne, N. Schaeffer, D. G. Fernig, and B. Lounis, "Photothermal absorption correlation spectroscopy," *ACS Nano*, vol. 3, no. 2, pp. 345–350, 2009.
- [152] D. J. Nieves, Y. Li, D. G. Fernig, and R. Levy, "Photothermal raster image correlation spectroscopy of gold nanoparticles in solution and on live cells," *Royal Society Open Science*, vol. 2, no. 6, 2015.

- [153] L. Ma, G. Rajshekhar, R. Wang, B. Bhaduri, S. Sridharan, M. Mir, A. Chakraborty, R. Iyer, S. Prasanth, L. Millet, M. U. Gillette, and G. Popescu, "Phase correlation imaging of unlabeled cell dynamics," *Scientific Reports*, vol. 6, no. 1, p. 32702, 2016.
- [154] T. Wohland, R. Rigler, and H. Vogel, "The Standard Deviation in Fluorescence Correlation Spectroscopy," *Biophysical Journal*, vol. 80, no. 6, pp. 2987–2999, 2001.
- [155] D. L. Kolin and P. W. Wiseman, "Advances in image correlation spectroscopy: Measuring number densities, aggregation states, and dynamics of fluorescently labeled macromolecules in cells," *Cell Biochemistry and Biophysics*, vol. 49, pp. 141–164, oct 2007.
- [156] K. H. Su, Q. H. Wei, X. Zhang, J. J. Mock, D. R. Smith, and S. Schultz, "Interparticle coupling effects on plasmon resonances of nanogold particles," *Nano Letters*, vol. 3, no. 8, pp. 1087–1090, 2003.
- [157] S. Broillet, D. Szlag, A. Bouwens, L. Maurizi, H. Hofmann, T. Lasser, and M. Leutenegger, "Visible light optical coherence correlation spectroscopy," *Optics Express*, vol. 22, p. 21944, sep 2014.
- [158] S. Broillet, A. Sato, S. Geissbuehler, C. Pache, A. Bouwens, T. Lasser, and M. Leutenegger, "Optical coherence correlation spectroscopy (OCCS)," *Optics Express*, vol. 22, p. 782, jan 2014.
- [159] T. Kalwarczyk, N. Ziebacz, A. Bielejewska, E. Zaboklicka, K. Koynov, J. Szymanski, A. Wilk, A. Patkowski, J. Gapinski, H.-J. Butt, and R. Holyst, "Comparative Analysis of Viscosity of Complex Liquids and Cytoplasm of Mammalian Cells at the Nanoscale," *Nano Letters*, vol. 11, pp. 2157–2163, may 2011.
- [160] K. Luby-Phelps, "Cytoarchitecture and Physical Properties of Cytoplasm: Volume, Viscosity, Diffusion, Intracellular Surface Area," *International review of cytology*, vol. 192, pp. 189–221, 1999.
- [161] R. J. Ellis, "Macromolecular crowding: Obvious but underappreciated," *Trends in Biochemical Sciences*, vol. 26, pp. 597–604, oct 2001.
- [162] R. J. Ellis, "Macromolecular crowding: An important but neglected aspect of the intracellular environment," feb 2001.
- [163] R. Leitgeb, C. Hitzenberger, and A. Fercher, "Performance of fourier domain vs time domain optical coherence tomography," *Optics Express*, vol. 11, p. 889, apr 2003.
- [164] C. B. Müller, A. Loman, W. Richtering, and J. Enderlein, "Dual-focus fluorescence correlation spectroscopy of colloidal solutions: Influence of particle size," *Journal of Physical Chemistry B*, vol. 112, pp. 8236–8240, jul 2008.

Bibliography

- [165] K. Starchev, J. Zhang, and J. Buffle, “Applications of Fluorescence Correlation Spectroscopy— Particle Size Effect,” *Journal of Colloid and Interface Science*, vol. 203, pp. 189–196, jul 1998.
- [166] T. Deptuła, J. Buitenhuis, M. Jarzebski, A. Patkowski, and J. Gapinski, “Size of Submicrometer Particles Measured by FCS: Correction of the Confocal Volume,” *Langmuir*, vol. 31, pp. 6681–6687, jun 2015.
- [167] S. Rüttinger, V. Buschmann, B. Krämer, R. Erdmann, R. MacDonald, and F. Koberling, “Comparison and accuracy of methods to determine the confocal volume for quantitative fluorescence correlation spectroscopy,” *Journal of Microscopy*, vol. 232, pp. 343–352, oct 2008.
- [168] J. W. Krieger, A. P. Singh, N. Bag, C. S. Garbe, T. E. Saunders, J. Langowski, and T. Wohland, “Imaging fluorescence (cross-) correlation spectroscopy in live cells and organisms,” *Nature Protocols*, vol. 10, pp. 1948–1974, nov 2015.
- [169] D. Su, X. Hu, C. Dong, and J. Ren, “Determination of Caspase-3 Activity and Its Inhibition Constant by Combination of Fluorescence Correlation Spectroscopy with a Microwell Chip,” *Analytical Chemistry*, vol. 89, pp. 9788–9796, aug 2017.
- [170] A. P. Singh, R. Galland, M. L. Finch-Edmondson, G. Greci, J. B. Sibarita, V. Studer, V. Viasnoff, and T. E. Saunders, “3D Protein Dynamics in the Cell Nucleus,” *Biophysical Journal*, vol. 112, pp. 133–142, jan 2017.
- [171] D. Krüger, J. Ebenhan, S. Werner, and K. Bacia, “Measuring Protein Binding to Lipid Vesicles by Fluorescence Cross-Correlation Spectroscopy,” *Biophysical Journal*, jul 2017.
- [172] R. Grover, J. Fischer, F. W. Schwarz, W. J. Walter, P. Schwille, and S. Diez, “Transport efficiency of membrane-anchored kinesin-1 motors depends on motor density and diffusivity,” *Proceedings of the National Academy of Sciences*, vol. 113, pp. E7185–E7193, nov 2016.
- [173] F. Höfling and T. Franosch, “Anomalous transport in the crowded world of biological cells,” *Reports on Progress in Physics*, vol. 76, p. 046602, apr 2013.
- [174] P. Mishra and D. C. Chan, “Mitochondrial dynamics and inheritance during cell division, development and disease,” *Nature Reviews Molecular Cell Biology*, vol. 15, pp. 634–646, sep 2014.
- [175] M. Sison, S. Chakraborty, J. Extermann, A. Nahas, P. James Marchand, A. Lopez, T. Weil, and T. Lasser, “3D Time-lapse Imaging and Quantification of Mitochondrial Dynamics,” *Scientific Reports*, vol. 7, p. 43275, feb 2017.

- [176] J. M. Tucker-Schwartz, T. Hong, D. C. Colvin, Y. Xu, and M. C. Skala, "Dual-modality photothermal optical coherence tomography and magnetic-resonance imaging of carbon nanotubes," *Optics Letters*, vol. 37, p. 872, mar 2012.
- [177] C. Zhou, T.-H. Tsai, D. C. Adler, H.-C. Lee, D. W. Cohen, A. Mondelblatt, Y. Wang, J. L. Connolly, and J. G. Fujimoto, "Photothermal optical coherence tomography in ex vivo human breast tissues using gold nanoshells," *Optics Letters*, vol. 35, p. 700, mar 2010.
- [178] J. Y. Tinevez, N. Perry, J. Schindelin, G. M. Hoopes, G. D. Reynolds, E. Laplantine, S. Y. Bednarek, S. L. Shorte, and K. W. Eliceiri, "TrackMate: An open and extensible platform for single-particle tracking," *Methods*, vol. 115, pp. 80–90, feb 2017.
- [179] J. Schindelin, I. Arganda-Carreras, E. Frise, V. Kaynig, M. Longair, T. Pietzsch, S. Preibisch, C. Rueden, S. Saalfeld, B. Schmid, J.-Y. Tinevez, D. J. White, V. Hartenstein, K. Eliceiri, P. Tomancak, and A. Cardona, "Fiji: an open-source platform for biological-image analysis," *Nature Methods*, vol. 9, pp. 676–682, jun 2012.
- [180] A. Einstein, "Über die von der molekularkinetischen Theorie der Wärme geforderte Bewegung von in ruhenden Flüssigkeiten suspendierten Teilchen," *Annalen der Physik*, vol. 322, no. 8, pp. 549–560, 1905.
- [181] N. Chenouard, I. Smal, F. de Chaumont, M. Maška, I. F. Sbalzarini, Y. Gong, J. Cardinale, C. Carthel, S. Coraluppi, M. Winter, A. R. Cohen, W. J. Godinez, K. Rohr, Y. Kalaidzidis, L. Liang, J. Duncan, H. Shen, Y. Xu, K. E. G. Magnusson, J. Jaldén, H. M. Blau, P. Paul-Gilloteaux, P. Roudot, C. Kervrann, F. Waharte, J.-Y. Tinevez, S. L. Shorte, J. Willemsse, K. Celler, G. P. van Wezel, H.-W. Dan, Y.-S. Tsai, C. O. de Solórzano, J.-C. Olivo-Marin, and E. Meijering, "Objective comparison of particle tracking methods," *Nature Methods*, vol. 11, pp. 281–289, jan 2014.
- [182] I. F. Sbalzarini and P. Koumoutsakos, "Feature point tracking and trajectory analysis for video imaging in cell biology," *Journal of Structural Biology*, vol. 151, pp. 182–195, aug 2005.
- [183] H. Qian, M. P. Sheetz, and E. L. Elson, "Single particle tracking. Analysis of diffusion and flow in two-dimensional systems," *Biophysical Journal*, vol. 60, pp. 910–921, oct 1991.
- [184] J. P. Bouchaud, A. Comtet, A. Georges, and P. Le Doussal, "Classical diffusion of a particle in a one-dimensional random force field," *Annals of Physics*, vol. 201, pp. 285–341, aug 1990.
- [185] B. T. Wilson, Z. Stark, R. E. Sutton, S. Danda, A. V. Ekbote, S. M. Elsayed, L. Gibson, J. A. Goodship, A. P. Jackson, W. T. Keng, M. D. King, E. McCann, T. Motojima, J. E. Murray, T. Omata, D. Pilz, K. Pope, K. Sugita, S. M. White, and I. J. Wilson, "The Cockayne

Bibliography

- Syndrome Natural History (CoSyNH) study: clinical findings in 102 individuals and recommendations for care,” *Genetics in Medicine*, vol. 18, pp. 483–493, may 2016.
- [186] A. R. Lehmann, “Three complementation groups in Cockayne syndrome.,” *Mutation research*, vol. 106, pp. 347–56, dec 1982.
- [187] K. Tanaka, K. Kawai, Y. Kumahara, M. Ikenaga, and Y. Okada, “Genetic complementation groups in cockayne syndrome.,” *Somatic cell genetics*, vol. 7, pp. 445–55, jul 1981.
- [188] I. Rapin, K. Weidenheim, Y. Lindenbaum, P. Rosenbaum, S. N. Merchant, S. Krishna, and D. W. Dickson, “Cockayne Syndrome in Adults: Review With Clinical and Pathologic Study of a New Case,” *Journal of Child Neurology*, vol. 21, pp. 991–1006, nov 2006.
- [189] M. Scheibye-Knudsen, M. Ramamoorthy, P. Sykora, S. Maynard, P.-C. Lin, R. K. Minor, D. M. Wilson, M. Cooper, R. Spencer, R. de Cabo, D. L. Croteau, and V. A. Bohr, “Cockayne syndrome group B protein prevents the accumulation of damaged mitochondria by promoting mitochondrial autophagy,” *The Journal of Experimental Medicine*, vol. 209, pp. 855–869, apr 2012.
- [190] V. Laugel, C. Dalloz, A. Sary, V. Cormier-Daire, I. Desguerre, M. Renouil, A. Fourmaintraux, R. Velez-Cruz, J.-M. Egly, A. Sarasin, and H. Dollfus, “Deletion of 5’ sequences of the CSB gene provides insight into the pathophysiology of Cockayne syndrome,” *European Journal of Human Genetics*, vol. 16, pp. 320–327, mar 2008.
- [191] M. Scheibye-Knudsen, D. L. Croteau, and V. A. Bohr, “Mitochondrial deficiency in Cockayne syndrome,” *Mechanisms of Ageing and Development*, vol. 134, pp. 275–283, may 2013.
- [192] M. Fousteri and L. H. Mullenders, “Transcription-coupled nucleotide excision repair in mammalian cells: molecular mechanisms and biological effects,” *Cell Research*, vol. 18, pp. 73–84, jan 2008.
- [193] K. Horibata, Y. Iwamoto, I. Kuraoka, N. G. J. Jaspers, A. Kurimasa, M. Oshimura, M. Ichihashi, and K. Tanaka, “From The Cover: Complete absence of Cockayne syndrome group B gene product gives rise to UV-sensitive syndrome but not Cockayne syndrome,” *Proceedings of the National Academy of Sciences*, vol. 101, pp. 15410–15415, oct 2004.
- [194] T. Nardo, R. Oneda, G. Spivak, B. Vaz, L. Mortier, P. Thomas, D. Orioli, V. Laugel, A. Sary, P. C. Hanawalt, A. Sarasin, and M. Stefanini, “A UV-sensitive syndrome patient with a specific CSA mutation reveals separable roles for CSA in response to UV and oxidative DNA damage.,” *Proceedings of the National Academy of Sciences of the United States of America*, vol. 106, pp. 6209–14, apr 2009.

- [195] J. Tuo, P. Jaruga, H. Rodriguez, V. A. Bohr, and M. Dizdaroglu, "Primary fibroblasts of Cockayne syndrome patients are defective in cellular repair of 8-hydroxyguanine and 8-hydroxyadenine resulting from oxidative stress.," *FASEB journal : official publication of the Federation of American Societies for Experimental Biology*, vol. 17, pp. 668–74, apr 2003.
- [196] T. Stevnsner, S. Nyaga, N. C. de Souza-Pinto, G. T. J. van der Horst, T. G. M. F. Gorgels, B. A. Hogue, T. Thorslund, and V. A. Bohr, "Mitochondrial repair of 8-oxoguanine is deficient in Cockayne syndrome group B," *Oncogene*, vol. 21, pp. 8675–8682, dec 2002.
- [197] A. Kusumi, Y. Sako, and M. Yamamoto, "Confined lateral diffusion of membrane receptors as studied by single particle tracking (nanovid microscopy). Effects of calcium-induced differentiation in cultured epithelial cells," *Biophysical Journal*, vol. 65, pp. 2021–2040, nov 1993.
- [198] M. J. Saxton and K. Jacobson, "SINGLE-PARTICLE TRACKING:Applications to Membrane Dynamics," *Annual Review of Biophysics and Biomolecular Structure*, vol. 26, no. 1, pp. 373–399, 1997.

Miguel Sison

Data of birth: 19.01.1988

Nationality: Philippines

Education

- 2013 – Present** **PhD. in Photonics**
École polytechnique fédérale de Lausanne
Laboratoire d'Optique Biomedicale (LOB), Prof. Theo Lasser
- 2010 – 2013** **Friedrich-Schiller-Universität Jena**
MSc. Photonics, Abbe School of Photonics
Jena, Germany
- 2005 – 2010** **University of the Philippines, Diliman Campus**
BSc. Applied Physics, National Institute of Physics
Quezon City, Philippines

Experience and Projects

- 2011 – 2013** **Institute of Applied Physics**
Abbe School of Photonics, Friedrich-Schiller-Universität Jena
Supervisors: Prof. Dr. Thomas Pertsch and Dr. Norik Janunts
- Master thesis: “Plasmonic black hole”
- Semester project: “Secondary surface plasmon-polaritons generated by nanohole and measurement of probe oscillation amplitude of scanning near-field optical microscope”
- Internship: “Stabilization and testing of phase-resolved fiber based scanning near-field optical microscope”
- 2007 – 2010** **Instrumentation Physics Laboratory**
National Institute of Physics, University of the Philippines, Diliman Campus
Supervisor: Prof. Caesar Saloma
- Bachelor thesis: “Dynamic range of optical-feedback semiconductor laser interferometer”

Teaching and Supervision

- Project supervision: École polytechnique fédérale de Lausanne (EPFL)
Master project, Yohan Lecomte, spring semester 2014
Semester Project, Alexandre Emmanuel Wetzel, fall semester 2015
Semester project, Cédric Kilchoer, spring semester 2014
Semester project, Adrien Descloux, fall semester 2013
Semester project, Timothée Bronner, fall semester 2013
Laboratory immersion, Valentin Oreiller, summer 2014
- Teaching assistance: École polytechnique fédérale de Lausanne (EPFL)
Bi microscopy I, Prof. T. Lasser, fall semester 2013, 2014, and 2015
Bi microscopy II Prof. T. Lasser, spring semester 2014
Imaging Optics Prof. H.P. Herzig, spring semester 2015 and 2016

Peer-reviewed Publications

Published:

M. Sison, S. Chakraborty, J. Extermann, A. Nahas, P.J. Marchand, A. Lopez, T. Weil, T. Lasser “3D Time-lapse Imaging and Quantification of Mitochondrial Dynamics”, *Scientific Reports*, 7, 43275, 2017

S. Chakraborty, **M. Sison**, YZ. Wu, A. Ladenburger, G. Pramanik, J. Biskupek, J. Extermann, K. Kaiser, T. Lasser, T. Weil, NIR-emitting and photo-thermal active nanogold as mitochondria specific probes, *Biomaterials Science*, 5, 966-971, (2017)

S. Coquoz, A. Nahas, **M. Sison**, A. Lopez, and T. Lasser, “High-speed phase-shifting common-path quantitative phase imaging with a piezoelectric actuator,” *J. Biomed. Opt.* 21(12), 126019 (2016)

P. J. Marchand, A. Bouwens, D. Szlag, D. Nguyen, A. Descloux, **M. Sison**, S. Coquoz, J. Extermann, and T. Lasser, “Visible spectrum extended-focus optical coherence microscopy for label-free subcellular tomography,” *Biomed. Opt. Express* 8(7), 3343-3359 (2017)

WN. Liu, B. Naydenov, S. Chakraborty, B. Wuensch, K. Hubner, S. Ritz, H. Colfen, H. Barth, K. Koynov, HY. Qi, R. Leiter, R. Reuter, J. Wrachtrup, F. Boldt, J. Scheuer, U. Kaiser, **M. Sison**, T. Lasser, P. Tinnefeld, F. Jelezko, P. Walther, YZ. Wu, T. Weil, “Fluorescent Nanodiamond-Gold Hybrid Particles for Multimodal Optical and Electron Microscopy Cellular Imaging”, *Nano Letters* 16 (10), 6236-6244, (2016)

B. N. Tugchin, N. Janunts, A. E. Klein, M. Steinert, S. Fasold, S. Diziain, **M. Sison**, E.-B. Kley, A. Tünnermann, T. Pertsch, “Plasmonic Tip Based on Excitation of Radially Polarized Conical Surface Plasmon Polariton for Detecting Longitudinal and Transversal Fields”, *ACS Photonics*, 2(10), 1468–1475, (2015)

Submitted:

M. Sison, J. Extermann S. Chakraborty, T. Weil, T. Lasser, “Quantifying mitochondrial dynamics via 3D single particle tracking”, *Optics Letters*, October (2017)

Conference Contributions

M. Sison, S. Chakraborty, J. Extermann, A. Nahas, C. Pache, T. Weil, T. Lasser “Three dimensional time lapse imaging of live cell mitochondria with photothermal optical lock-in optical coherence microscopy”, *SPIE Photonics West, San Francisco, USA* (2016)

M. Sison, P.J. Marchand, A. Bouwens, S. Coquoz, J. Extermann and T. Lasser, "Live cell imaging with visible wavelength extended-focus optical coherence microscopy," *Focus on Microscopy 2015, Göttingen, Germany* (2015)

S. Coquoz, L. Mouchiroud, **M. Sison**, D. Szlag, P. J. Marchand, A. Bouwens, J. Auwerx, T. Lasser, “Label-free three-dimensional imaging of *C. elegans* with visible wavelength extended-focus optical coherence microscopy”, *SPIE Photonics West, San Francisco, USA* (2016)

Languages

Filipino/Tagalog	mother tongue
English	fluent
German	A1
French	beginner

